



**DEVELOPMENT OF ADAPTIVE TILT TRACKER THAT UTILIZES  
QUADRANT-CELL DETECTOR TO TRACK EXTENDED OBJECTS**

THESIS

Issac J. Thornton, First Lieutenant, USAF

AFIT-ENG-14-M-78

**DEPARTMENT OF THE AIR FORCE  
AIR UNIVERSITY**

**AIR FORCE INSTITUTE OF TECHNOLOGY**

---

---

**Wright-Patterson Air Force Base, Ohio**

**DISTRIBUTION STATEMENT A.**  
APPROVED FOR PUBLIC RELEASE; DISTRIBUTION UNLIMITED.

The views expressed in this thesis are those of the author and do not reflect the official policy or position of the United States Air Force, Department of Defense, or the United States Government. This material is declared a work of the U.S. Government and is not subject to copyright protection in the United States.

AFIT-ENG-14-M-78

**DEVELOPMENT OF ADAPTIVE TILT TRACKER THAT UTILIZES  
QUADRANT-CELL DETECTOR TO TRACK EXTENDED OBJECTS**

**THESIS**

Presented to the Faculty

Department of Electrical and Computer Engineering

Graduate School of Engineering and Management

Air Force Institute of Technology

Air University

Air Education and Training Command

In Partial Fulfillment of the Requirements for the  
Degree of Master of Science in Electrical Engineering

Issac J. Thornton, BS

First Lieutenant, USAF

March 2014

**DISTRIBUTION STATEMENT A.**  
APPROVED FOR PUBLIC RELEASE; DISTRIBUTION UNLIMITED.

**DEVELOPMENT OF ADAPTIVE TILT TRACKER THAT UTILIZES  
QUADRANT-CELL DETECTOR TO TRACK EXTENDED OBJECTS**

Issac J. Thornton, BS

First Lieutenant, USAF

Approved:

//Signed//

27 Feb 2014

\_\_\_\_\_  
James A. Louthain, Lt Col, USAF (Chairman)

\_\_\_\_\_  
Date

//Signed//

27 Feb 2014

\_\_\_\_\_  
Milo W. Hyde IV, Major, USAF (Member)

\_\_\_\_\_  
Date

//Signed//

27 Feb 2014

\_\_\_\_\_  
Richard G. Cobb, PhD (Member)

\_\_\_\_\_  
Date

### Abstract

Atmospheric turbulence causes tilt distortion that requires telescopes to track and remove image jitter effects. This research develops an adaptive tilt tracking system to measure and compensate for centroid gain volatility while tracking extended objects. The adaptive tracker counteracts deviations in tilt measurement and correction, due to unintended centroid gain changes. Non-adaptive trackers experience sub-optimal bandwidths and possible instabilities. The adaptive tracker utilizes a quadrant (QUAD) cell detector to measure tilt distortion and its centroid gain relates measured intensity imbalances amongst the four cells to tilt distortion. Additionally, this gain becomes a random variable as it is determined by random image spot characteristics. A tracked low Earth orbit (LEO) object and atmospheric seeing govern spot characteristics. Unlike static natural or laser guide stars, a LEO object's intensity, size, and shape are highly dynamic, resulting in a volatile centroid gain.

This research conducts a rigorous characterization of the QUAD-cell. Results show the QUAD-cell is inherently unreliable while measuring tilt distortion of LEO objects that have resolvable asymmetrical characteristics. This research develops an innovative methodology that rotates the LEO object's image to create a more favorable intensity distribution for the QUAD-cell. Along with image rotation, an adaptive gain term yields significant improvements in QUAD-cell measurement performance, up to 91% for the simulated tilt processes. Applying the methodology, this research realizes an adaptive tilt tracker model that dithers the fast steering mirror to detect non-optimal centroid gains. For a signal to noise ratio of five, results show the adaptive tracker counteracts centroid-gain deviations to attenuate the aperture's one-axis, one-sigma *G-tilt* angle deviation up to 97.76%. The corresponding average maximum long exposure Strehl ratio is about 0.67, a 116% improvement over the non-adaptive tracker.

## **Acknowledgments**

I am grateful to the Air Force and AFIT in providing an opportunity for me to earn an advanced degree. Additionally, I appreciate my advisor's role throughout this effort.

Issac J. Thornton

## Table of Contents

	Page
Abstract .....	iv
Table of Contents .....	vi
List of Figures .....	ix
List of Tables .....	xv
 I. Introduction .....	 1
1.1 Overture .....	1
1.2 Problem Statement.....	3
1.3 Research Objectives .....	4
1.4 Research Contributions .....	4
1.5 Thesis Overview .....	7
 II. Background and Theory .....	 9
Chapter Overview.....	9
Description .....	9
2.1 Tracking Low Earth Orbit Objects .....	9
2.2 Tilt Distortion .....	10
2.2.1 Atmospheric Turbulence .....	10
2.2.2 Characteristics of Tilt Distortion .....	11
2.2.2.1 Tilt Distortion Process .....	12
2.2.2.2 Tilt Distortion Spatial Variance.....	12
2.2.2.3 Tilt Distortion Temporal Dynamics .....	14
2.3 Tilt Measurement With QUAD-cells .....	17
2.4 QUAD-cell Characteristics.....	20
2.4.1 Justification for QUAD-cells.....	20
2.4.2 Shannon-Nyquist Sampling Violation.....	22
2.4.3 Performance With Asymmetrical Intensity Distributions .....	23
2.4.4 Centroid Gain Dependence on Spot Characteristics .....	25
2.5 Adaptive Optics .....	29
2.5.1 Definition.....	29
2.5.2 Tilt Tracker .....	29
2.5.3 Tilt Tracker Performance .....	31
2.5.3.1 Temporal Error .....	32
2.5.3.2 Measurement Error .....	33
2.6 Centroid Gain Variance and Tracker Performance .....	35
2.7 Adaptive Tilt Tracker .....	37
2.8 Methods for Estimating an Arbitrary <b><i>Kg</i></b> .....	40
2.8.1 Utilize Focal Plane Array (FPA) .....	40
2.8.2 Monitor Deformable Mirror (DM) Shape .....	41
2.8.3 Measure Slope Discrepancy .....	42
2.8.4 Dither Tilt Mirror (TM).....	43

III. Optical Modeling and Methodology .....	45
Chapter Overview.....	45
3.1 Model Tilt Process.....	45
3.1.1 Tilt Filter Realization .....	48
3.1.2 Filter Verification .....	49
3.2 Model Optical Setup.....	50
3.2.1 Pyramid Track Sensor (PTS).....	52
3.2.2 Focal Plane Array (FPA) .....	56
3.3 Model LEO Objects.....	57
3.4 Model Signal Flux .....	58
3.5 PTS Frame Rate Characterization .....	59
3.5.1 Determine Threshold <b><i>SNR<sub>v</sub></i></b> Value .....	59
3.5.2 Determine Threshold Frame Rate .....	63
3.6 PTS Centroid Gain Characterization .....	67
3.6.1 Centroid Gain and Spot Spread Relationship .....	68
3.6.2 Tilt Phase Measurement .....	69
3.6.2.1 Tilt Measurement Using Gaussian Source .....	72
3.6.2.2 Tilt Measurement Using Satellite and Missile Objects .....	74
3.6.3 Psuedo-tilt Phase .....	76
3.6.4 Create Symmetrical Intensity Distribution .....	79
IV. Analysis and Results for the Adaptive Tilt Tracker .....	85
4.1 System Description.....	85
4.1.1 Fast Steering Mirror .....	85
4.1.2 Determine <b><i>K<sub>g_opt</sub></i></b> .....	87
4.1.3 Determine Dither Throw and Frequency.....	87
4.1.4 Determine Dither Filter .....	88
4.1.5 Determine Dither Period.....	90
4.1.6 Determine Adaptive Gain, <b><i>K<sub>c</sub></i></b> .....	91
4.1.7 Determine Frame Rate, <b><i>f<sub>s</sub></i></b> .....	91
4.2 Non-Adaptive Tilt Tracker Behavior .....	93
4.3 Demonstration of the Adaptive Tilt Tracker .....	98
4.3.1 Scenario 1 ( <b><i>α</i></b> less than unity for <b><i>f<sub>max</sub></i></b> ) .....	103
4.3.2 Scenario 2 ( <b><i>α</i></b> less than unity for <b><i>f<sub>0</sub></i></b> ) .....	107
4.3.3 Scenario 3 ( <b><i>α</i></b> greater than unity).....	110
4.3.4 Scenario 4 (Desired Tracker Features) .....	116
4.3.4.1 Recalibration.....	116
4.3.4.2 Averaging PTS output signals .....	119
4.3.5 Summary of Scenario Results .....	123
V. Conclusions and Future Considerations.....	128
Chapter Overview.....	128
5.1 Notable Conclusions and Contributions of Research.....	129
5.1.1 Defining QUAD-cell Behavior.....	129
5.1.2 Creating Symmetrical Intensity Distribution/Spot Shape .....	130



5.1.3 Considering Methods to Estimate Spot Size .....	131
5.1.4 Defining the Tracker/QUAD-cell Control Problem .....	132
5.1.5 Recommending Adaptive Tracker Capabilities.....	133
5.2 Future Considerations.....	134
Bibliography .....	138

## List of Figures

	Page
1. Left figure shows a LEO satellite image with no tilt distortion; the right figure shows how tilt distortion blurs the long exposure image of the LEO satellite.....	2
2. The temporal and spatial aspects of atmospheric turbulence [6].....	10
3. The red and blue wavefronts represent two different instances of tilt distortion over the lens diameter, $d$ , [8].....	11
4. The dashed and dotted lines are <i>Z-tilt</i> , <i>G-tilt</i> , and <i>P-tilt</i> measures for tilt phase distortion where the black curve is the 1-D representation of tilt phase distortion over an aperture [8] .....	13
5. G-tilt PSD where it shows $\text{fBW} = 44.2 \text{ Hz}$ .....	16
6. Random process of tilt distortion that is defined by the <i>G-tilt</i> spatial variance and PSD parameters for a vertical slewing telescope .....	17
7. QUAD-cell configuration measuring spot intensity shifts amongst the four cells (QA, QB, QC, and QD) .....	18
8. Normalized magnitude of $\text{SNR}_v$ derivative for different signal levels.....	21
9. Detector A indicates proper sampling; the spot illuminates two pixels for QUAD-cell B, the spot illuminates one pixel for QUAD-cell C, the spot illuminates four pixels for QUAD-cell D .....	23
10. Asymmetrical intensity distribution of a LEO satellite object .....	24
11. QUAD-cell partitions intensity distribution from a Gaussian laser source into four cells to measure tilt distortion .....	26
12. PTS response curve revealed by plotting $I_x$ versus $W_x$ .....	28
13. One-axis closed-loop tilt tracker schematic.....	30
14. One-axis tilt tracker CL transfer function diagram .....	35
15. AOTools® atmospheric statistics menu .....	45

16. CL FSM magnitude frequency response depicted by the solid curve with dashed lines to indicate 3 dB bandwidth point about 200 Hz .....	47
17. G-Tilt PSD depicted by solid curve with dashed lines to indicate a Tyler frequency about 44 Hz.....	47
18. Yule-Walker filter time correlates the inputted ‘white’ tilt process according to G-tilt PSD .....	48
19. Verification of G-tilt filter frequency response .....	49
20. Simulated 3.5 meter annular aperture where optical signals are passed within the white region .....	51
21. Optical pyramid creating four intensity spots to be measured by the detector [19].....	52
22. PTS QUAD-cell detecting tilt disturbance by measuring cell intensity imbalances .....	53
23. Phase mask to simulate PTS pyramidal face effects .....	56
24. Simulated Satellite and ICBM LEO objects .....	58
25. Normalized tracker error where the dashed line shows the minimum tracker error being limited by temporal tracker error .....	62
26. Tilt tracker system represented as a sampled-data system in the $s$ -domain to show phase delay effects due to detector operation.....	63
27. Normalized Kg plotted versus spot spread to show inverse relationship .....	68
28. Torpid sensor response using a spot spread of 40.5% .....	70
29. Hyper-sensitive PTS response using a spot spread of 6.0% .....	71
30. Overlay of normalized RMSE curves for CL (blue) and OL (red) y-tilt phase processes identify the same optimal spot region; maximum CL RMSE = 0.6589 and maximum OL RMSE = 15.656 .....	72
31. Overlay of normalized RMSE curves for CL (blue) and OL (red) y-tilt phase processes identify the same optimal spot region; maximum CL RMSE = 0.4418 and maximum OL RMSE = 14.694 .....	73
32. CL y-tilt phase measurement using satellite object as source .....	74

33. CL $x$ -tilt phase measurement using missile object as source.....	75
34. Tilt measurement using a CW rotating satellite .....	77
35. Green curve represents zero reference tilt being applied at the aperture; red curve shows a non-zero measured tilt for the CW rotating satellite .....	78
36. Satellite and missile intensity distribution over QUAD-cell region.....	79
37. Rotated satellite (left) and missile (right) intensity distribution over the FPA.....	80
38. Rotated satellite (left) and missile (right) intensity distribution over the QUAD-cell.....	80
39. Tracking performance for rotating satellite image and adaptive gain to improve PTS $y$ -tilt phase measurement .....	81
40. Adaptive gain term (blue path) being applied to recover original tilt disturbance, $W$ .....	82
41. Tracking performance for rotating missile image and adaptive gain to improve PTS $x$ -tilt phase measurement .....	83
42. Step response for a critically damped FSM.....	86
43. Comparison of dither signals that correspond to optimal and suboptimal centroid gains .....	87
44. Dither signal shown in tilt phase units being disturbed by atmospheric tilt and band-limited white noise.....	89
45. Dither band-pass filter response with a center-band frequency of 90 Hz.....	89
46. Dither filter passing dither signal at 90 Hz while suppressing signal oscillating at tilt bandwidth frequency of 44 Hz.....	90
47. Detector frame rate being adjusted according to $SNR_v$ ; the horizontal arrow represents $f_{max}$ and the downward arrow represents $f_s$ to sustain $SNR_{v\_0}$ .....	92
48. Curve shows detector frame rate relationship to $V\text{-mag}$ , where $V\text{-mag}$ value at $f_0$ corresponds to the limiting $V\text{-mag}$ for the tracker.....	93
49. Non-adaptive tracker response curves for a unit step input and total delay	

time of 150 $\mu$ s where the curves are evaluated over varying normalized detector response, $\alpha$ .	94
50. Non-adaptive tracker response curves for a unit step input and total delay time of 298.75 $\mu$ s where the curves are evaluated over varying normalized detector response, $\alpha$ .	95
51. Non-adaptive tracker response curves for a unit step input and total delay time of 150 $\mu$ s where the curves are evaluated over varying normalized detector response, $\alpha$ .	96
52. Non-adaptive tracker response curves for a unit step input and total delay time of 298.75 $\mu$ s where the curves are evaluated over varying normalized detector response, $\alpha$ .	97
53. Left-half of adaptive tilt tracker model where the significant features are highlighted and discussed in table 9.	98
54. Right-half of adaptive tilt tracker model where the significant features are highlighted and discussed in table 9.	99
55. SIMULINK® model for PTS having independent Kgx and Kgy responses that are determined by image spot characteristics	101
56. Response for non-adaptive tilt tracker with $\alpha$ equal to 0.10 is shown by the dotted blue curve lagging the OL aperture tilt phase reference, shown by the solid green curve.	103
57. Adaptive tilt tracker calibrating for non-optimal $\alpha$ of 0.10 is shown by the dashed blue curve; after calibration, tracker response tracks OL aperture tilt phase reference, shown by the solid green curve.	104
58. Absolute averages for residual tracker error, in nano-radians, recorded for each randomly drawn, $\alpha$ . Each dot intersecting a radial for $\alpha$ indicates a measurement. The solid-red plot represents the adaptive tracker performance; the dashed-blue plot represents the non-adaptive tracker. Both trackers operate at fmax.	105
59. Standard deviations for residual tracker error, in nano-radians, recorded for each randomly drawn, $\alpha$ . Each dot intersecting a radial for $\alpha$ indicates a measurement. The solid-red plot represents the adaptive tracker performance; the dashed-blue plot represents the non-adaptive tracker. Both trackers operate at fmax.	106

60. Absolute averages for residual tracker error, in nano-radians, recorded for each randomly drawn $\alpha$ . Each dot intersecting a radial for $\alpha$ indicates a measurement. The solid-red plot represents the adaptive tracker performance; the dashed-blue plot represent the non-adaptive tracker. Both trackers operate at $f_0$ .....	108
61. Standard deviations for residual tracker error, in nano-radians, recorded for each randomly drawn, $\alpha$ . Each dot intersecting a radial for $\alpha$ indicates a measurement. The solid-red plot represents the adaptive tracker performance; the dashed-blue plot represents the non-adaptive tracker. Both trackers operate at $f_0$ .....	109
62. Non-adaptive tilt tracker operating with $\alpha$ equal to 1.61 shows a response that has steadily increasing oscillations about the OL aperture tilt phase reference.....	110
63. Adaptive tilt tracker calibrating for non-optimal $\alpha$ of 1.61 is shown by the dashed blue curve; after calibration, tracker response tracks OL aperture tilt phase reference, shown by the solid green curve.....	111
64. Non-adaptive tilt tracker operating with $\alpha$ equal to 1.53 in the presence of band limited white noise; response shows an amplification for the noise envelope about the OL aperture tilt phase reference. ....	112
65. Adaptive tilt tracker calibrating for non-optimal $\alpha$ of 1.53 in the presence of band limited white noise; after calibration, the dashed blue curve tracks OL aperture tilt phase reference with a reduced noise envelope. ....	113
66. Standard deviations for residual tracker error, in nano-radians (log10 scale), recorded for each randomly drawn, $\alpha$ . Each dot intersecting a radial for $\alpha$ indicates a measurement. The solid-red plot represents the adaptive tracker performance; the dashed-blue plot represents the non-adaptive tracker. Both trackers operate at $f_{max}$ .....	114
67. Standard deviations for residual tracker error, in nano-radians (log10 scale), recorded for each randomly drawn, $\alpha$ . Each dot intersecting a radial for $\alpha$ indicates a measurement. The solid-red plot represents the adaptive tracker performance; the dashed-blue plot represents the non-adaptive tracker. Both trackers operate at $f_0$ .....	115

68. Adaptive tilt tracker response shown by the dashed blue curve performs an initial calibration, then detects non-optimal $\alpha$ of 2.45 at 1.26 seconds, recalibrates at 1.33 seconds to track OL aperture tilt phase reference, shown by solid green curve. ....	117
69. Adaptive tilt tracker response for y-axis shown by the dashed blue curve; after initial calibration and recalibration using the $x$ -axis only, the tracker accurately tracks the OL aperture y-tilt phase reference, shown by solid green curve. ....	117
70. Standard deviations for residual tracker error, in nano-radians (log10 scale), recorded for each randomly drawn, $\alpha$ . Each dot intersecting a radial for $\alpha$ indicates a measurement. The solid-red plot represents the adaptive/averaging tracker performance; the dashed-dotted green plot represents the non-adaptive/averaging tracker; the dashed-blue plot represents the non-adaptive/non-averaging tracker. All trackers operate at $f_0$ . ....	121
71. Standard deviations for residual tracker error, in nano-radians (log10 scale), recorded for each randomly drawn, $\alpha$ . Each dot intersecting a radial for $\alpha$ indicates a measurement. The solid-red plot represents the adaptive/averaging tracker performance; the dashed-dotted green plot represents the non-adaptive/averaging tracker; the dashed-blue plot represents the non-adaptive/non-averaging tracker. All trackers operate at $f_{\max}$ . ....	122

## List of Tables

	Page
1. Telescope Parameters.....	50
2. QAUD-cell Specifications .....	54
3. Focal Plane Array Specifications [20] .....	57
4. PTS Frame Rate Characterization [ $Q_e = 0.50$ ; $\chi = 0.30$ ; $N_p = 4$ ] .....	60
5. Minimum allowable frame rate versus loop delay .....	67
6. Satellite Tilt Phase Measurements .....	82
7. Missile Tilt Phase Measurements .....	83
8. FSM Specifications .....	86
9. Adaptive Tracker Component Description .....	100
10. Summary of Results for Simulated Trackers .....	124



# **DEVELOPMENT OF ADAPTIVE TILT TRACKER THAT UTILIZES QUADRANT-CELL DETECTOR TO TRACK EXTENDED OBJECTS**

## **I. Introduction**

### **1.1 Overture**

Space is the ultimate high ground and is of critical interest to the United States Air Force. To maintain space situational awareness, the Air Force Research Laboratory's (AFRL) Directed Energy Directorate conducts research in laser guide star adaptive optics (AO) and space object identification. As satellites get smaller and the number of space objects increases dramatically, research in imaging and identification of space objects is paramount to meeting the Air Force's mission [1].

The Earth's atmosphere creates the greatest obstacle to effectively image and identify space objects using ground-based telescopes. When incident light encounters the atmosphere, it experiences a turbulent medium that distorts optical wavefronts. Without the AO technology, wavefront distortions due to atmospheric turbulence would be a stifling limitation for modern astronomical imaging systems. On the forefront of AO technology is the Starfire Optical Range's (SOR) AO telescopic system, where innovative research continually evolves the system's capabilities and the field of AO.

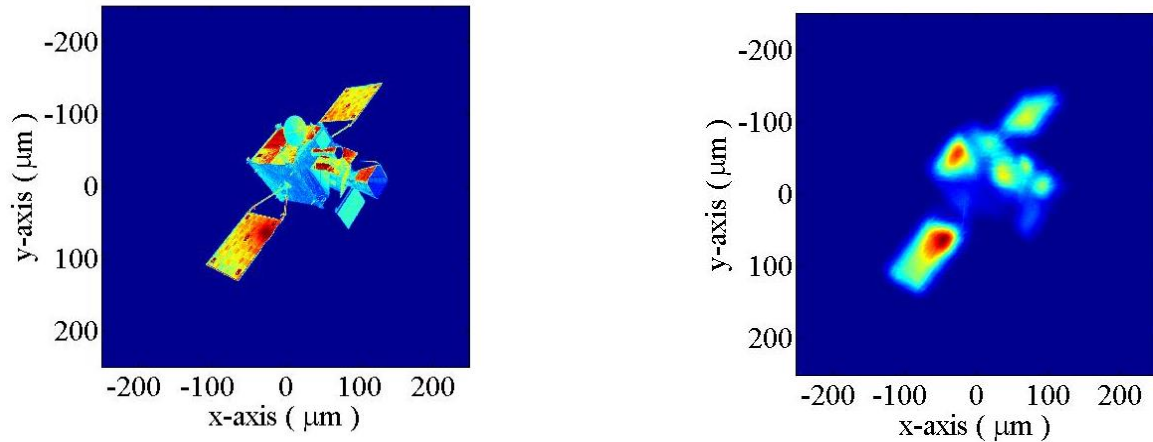


**Figure 1 - Left figure shows a LEO satellite image with no tilt distortion; the right figure shows how tilt distortion blurs the long exposure image of the LEO satellite**

This work addresses the SOR's tilt tracker system, a critical subsystem for the 3.5 meter AO telescope. The tilt tracker abates tilt wavefront distortions that rapidly jitter images. Consider figure 1 where the detrimental effects of tilt distortion are clearly evident; the left figure is a perfect LEO satellite image having no wavefront aberrations. The right figure shows the same satellite image being jittered by a moderate amount of tilt distortion, where the jittering effect reduces image resolution and intensity. It is important to note that LEO objects are typically dim such that tilt distortion degrades image quality to an even greater extent than what is demonstrated by figure 1.

In 1994, Robert Fugate reported preliminary SOR findings for the use of laser beams to compensate the images of faint objects using adaptive optics. He demonstrated a viable tilt tracker system for the 1.5 meter telescope with primary applications toward natural and laser guide stars. The system was innovative and is a relevant forerunner to the tracker proposed in this research. The tracker employed a QUAD-cell avalanche photodiode (APD) detector array to measure tilt distortion; the tracker enabled users to adjust

the detector's frame rate and the control loop gain to reduce tracker error in real-time [2]. In 2010, the SOR upgraded its tilt tracker system along with the sodium beacon AO upgrade to its 3.5 meter telescope [3]. The upgraded tracker indirectly measures global tilt over the aperture using a Shack-Hartman wavefront sensor. The sensor provides both tilt and focus measurements via four sub-apertures, where each sub-aperture has a 4x4 charge-coupled device (CCD) pixel array. As with Fugate's tilt tracker, the updated tracker has primary applications toward laser and natural guide stars; it also enables adjustments for frame rate and gain parameters to reduce tracker error in real-time.

## **1.2 Problem Statement**

The SOR desires to upgrade the tracker system developed in 2010 to an adaptive tracker system that is more suited to the demands of tracking LEO objects, like satellites. Since the laser beacon cannot provide a reliable tilt measurement and a natural guide star is not available for every sky location of a fast moving LEO object, the object itself must be used to measure tilt. This is problematic because LEO object characteristics may deviate substantially from those of guide stars; thereby, introducing unpredictable complications to the tracker system. Accordingly, the adaptive tracker must calibrate "on-the-fly" to adapt to the dynamic characteristics of the LEO object. Additionally, the SOR specifies that the adaptive tracker should utilize a QUAD-cell detector to measure tilt distortion of LEO objects; this adds an additional layer of complexity to the development of the adaptive tracker. The QUAD-cell's behavior is well documented for guide stars; however, documented QUAD-cell applications for LEO objects, e.g. satellites, are relatively non-existent. Since the QUAD-cell's measurement response depends on object characteristics,

it is anticipated the LEO object will cause the QUAD-cell and tracker system to deviate substantially from optimal performance.

### **1.3 Research Objectives**

This research will ultimately determine the viability of an adaptive tracker system that utilizes a QUAD-cell detector to measure tilt distortion of LEO objects. The problem statement above highlights unknowns this research seeks to investigate. First, this research must consider LEO object characteristics that are general enough as to apply to a wide set of scenarios; this will allow a rigorous treatment of the adaptive tilt tracking problem. Second, this research will fully characterize the QUAD-cell's measurement response with an LEO object; results seek to define a possibly unexplored application for the QUAD-cell. Third, this research aims to model a realistic adaptive tilt tracker control loop that clearly defines the control problem when utilizing the QUAD-cell. Finally, this research will consider various alternatives to implement the adaptive tracker, then recommend and simulate a particular methodology that provides relevant results to stakeholders.

### **1.4 Research Contributions**

The research contributions for this work are at the heart of improving methods to image and identify space objects. As stated above, space objects are becoming smaller and their population is ever increasing. Therefore, research to enhance space surveillance telescopes, such as the SOR's 3.5 meter telescope, is critical for the Air Force's mission to sustain space situational awareness. Consider the following notable research contributions made to the fields of adaptive optics and control engineering:

- **QUAD-cell Characterization:** The research findings for the QUAD-cell characterization contribute knowledge towards the field of adaptive optics for a previously undocumented or unexplored use for the QUAD-cell. Typically, AO systems employ QUAD-cell detectors to sense wavefront aberrations of natural and laser guide stars. However, their application towards an arbitrary LEO object was largely uncharacterized and/or undocumented. This research showed that the QUAD-cell detector's behavior deviates substantially from optimal for LEO objects that have asymmetrical characteristics, leading the author to conclude that the QUAD-cell is inherently unreliable for resolvable asymmetrical LEO objects. This research found a significant complication that does not typically occur for guide stars. If an asymmetrical LEO object appears to rotate, it will induce a false or pseudo tilt phase that can cause large and unexpected measurement errors for the QUAD-cell.
- **Image Rotation/Adaptive Gain Methodology:** The benefits of using the QUAD-cell detector to detect tilt distortion of dim LEO objects are so attractive that the author proposes a methodology to overcome the challenges discovered by the QUAD-cell characterization. The methodology to rotate the image of an asymmetrical and possibly rotating LEO object greatly simplifies the problem of tracking the object. Essentially all of the complicating variables that contribute to a non-optimal spot intensity distribution get transformed to make a more favorable distribution for the QUAD-cell. Additionally, the symmetry created by the rotation reduces estimation, processing, and calibration times by 50% for adaptive trackers.
- **Effectively Estimating Spot Size:** This research introduces the reader to four methods for estimating intensity spot sizes and considers the pros and cons for each method.

The dither method is determined to be most appropriate for this research. Since the dither method utilizes a single QUAD-cell detector to estimate spot size, it is more likely than the other methods to maintain fidelity even for dim LEO objects. This research develops an innovative procedure that determines a reference spot size (centroid gain) such that the dithering process can detect non-optimal spot sizes. The reference or optimal spot size is found using a calibrating laser source, where its spot size is systematically varied to measure open loop (OL) and closed loop (CL) tilt processes. Intuitively, the optimal spot corresponds to the spot that allows the QUAD-cell to measure both OL and CL processes with the least measurement error. Additionally, the implemented dither method utilizes a filter to suppress disturbances of spot estimates. Therefore, this research provides an effective application of the dither method that rapidly and robustly estimates spot sizes for arbitrary LEO objects.

- **Control Problem Definition:** This research also contributed to the field of control engineering, with respect to adaptive optics, by defining the control problem of the tilt tracker operating with a QUAD-cell detector. The core of the problem is that the QUAD-cell's response is an uncharacterized random variable for an arbitrary LEO object. When the detector's response, referred to as centroid gain, deviates from optimal, the tilt tracker correspondingly operates with non-optimal bandwidths and/or experiences possible instability. This research provided useful expressions that show how the QUAD-cell detector's operation affects the tilt tracker's phase and gain stability margins. The expressions allow a tilt tracker designer to determine the maximum allowable loop delay in order to sustain desired stability margins. This further allows the designer to determine the minimum or threshold frame rate for the

detector. Also, the expressions are useful in determining or approximating the critical response for the detector that makes the tracker unstable in the presence of a loop delay.

- **Recommended Tracker Capabilities:** The author presents two recommendations to enhance the adaptive tracker's robustness while tracking a LEO object. The first recommendation envisions the tracker having a capability to automatically recalibrate once a non-optimal spot size is detected. This is vital because a LEO object's characteristics can change unexpectedly after the initial calibration such that the initial calibration is made irrelevant to present conditions. This research successfully demonstrates a recalibration procedure. The second recommendation envisions averaging the pyramid track sensor's (PTS) output signals to reduce noise effects from band-limited white noise. Operating the PTS with the highest frame rate possible for adequate signal levels, may allow the sensor to take multiple samples of a given tilt instance. This research has demonstrated that averaging the samples had a measureable benefit in reducing the noise variance for the PTS's output.

## 1.5 Thesis Overview

Chapter II aims to provide the reader with necessary background and theory used to develop the adaptive tilt tracker. The chapter introduces the challenges associated with tracking LEO objects to abate tilt distortion. Furthermore, the chapter describes the mechanisms for tilt distortion. The remaining chapter involves a thorough characterization of the QUAD-cell detector; an analysis of the AO tilt tracker subsystem and subsequent motivation for the adaptive tilt tracker; and a comparison of adaptive tracker

methodologies. Therefore, Chapter II facilitates evaluation of the author's methodology, analysis/results, and conclusions/future considerations for this research.

This research requires extensive simulation that models the concepts introduced in Chapter II; therefore, Chapter III discusses the optical modeling and methodology used to simulate tilt distortion, the SOR 3.5 meter telescope, and associated optical sensors, particularly the pyramid track sensor (a type of QUAD-cell). This chapter further details notable limitations, assumptions, and design decisions for implemented models. Chapter III culminates with a viable methodology to measure tilt distortion of LEO objects with the QUAD-cell detector. Chapter IV implements the methodology born out of Chapter III to realize an effective adaptive tracker model that utilizes the QUAD-cell detector. Therefore, Chapter IV provides analysis and results for the adaptive tilt tracker model where a comparison for the non-adaptive and adaptive tilt trackers, in reference to simulation scenarios, clearly differentiate the trackers. Chapter V concludes this research with notable conclusions and considerations for future work.



## II. Background and Theory

### Chapter Overview

This chapter provides necessary background and theory to facilitate evaluation of the methodology, analysis/results, and conclusion/recommendations chapters of this work. The chapter starts by introducing the challenges associated with tracking a low earth orbiting object to abate tilt distortion. Then, the chapter presents the spatial and temporal mechanisms for tilt distortion. Finally, the remaining chapter involves measuring and compensating for tilt distortion: a thorough analysis of QUAD-cell detector characteristics; an analysis of the adaptive optics tilt tracker subsystem; a motivation for an adaptive tilt tracker; and a high level comparison of four adaptive tilt tracker methodologies.

### Description

#### 2.1 Tracking Low Earth Orbit Objects

Depending on atmospheric seeing, target range, optical parameters, and object characteristics, an object may appear to an optical system as having extent beyond a point source, thereby being termed an extended object. An object orbiting Earth at altitudes ranging about 160 to 2000 km with an average speed of 7.8 km/s, classify as being a LEO object. LEO objects encompass sizes from a basketball to that of the International Space Station [4]. Their motion may be controlled or completely unregulated. Furthermore, a LEO object's detectable intensity corresponds to a typical range of visual band apparent magnitudes (*V-mag*) about a dim +18 *V-mag* to a bright -6 *V-mag*; for reference, a *V-mag* of +6.50 is the mean limit for the naked eye and the Earth's moon has a *V-mag* of -12.92 [5]. The listed characteristics culminate to a dynamic object whose shape, motion, intensity

distribution, and *V-mag* present considerable challenges to a tracking system responsible for abating tilt distortion.

## 2.2 Tilt Distortion

### 2.2.1 Atmospheric Turbulence

The atmosphere is a dynamic fluid whose density varies both spatially and temporally. Density variances translate to refractive index fluctuations which randomize optical path lengths.

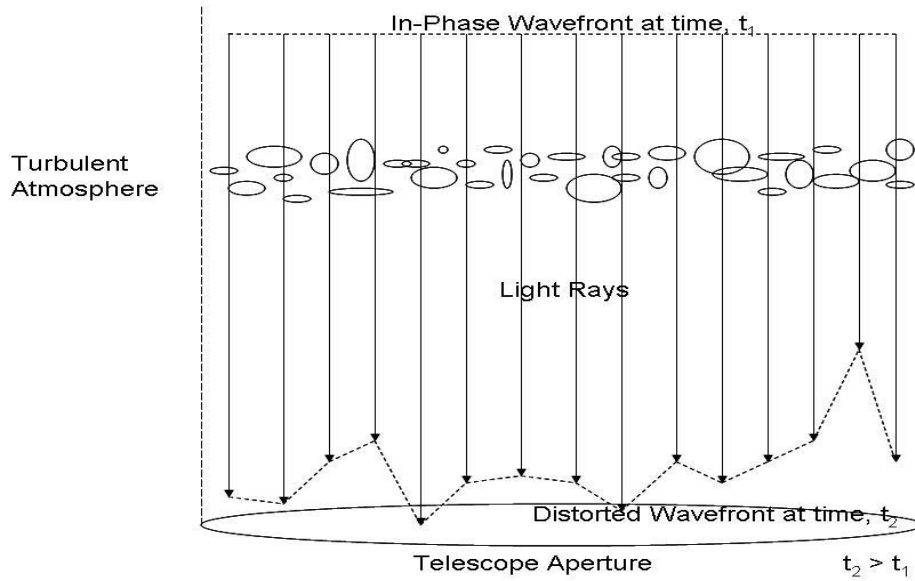


**Figure 2 - The temporal and spatial aspects of atmospheric turbulence [6]**

Consider figure 2; at time,  $t_1$ , a flat wavefront encounters atmospheric turbulence represented above by different sizes and orientations of circles. The circles represent turbulence eddies and the inhomogeneity of atmospheric turbulence. A light ray spatially separated from another may experience different turbulence and therefore travel a different path over the same time interval. Taking the contributions from each light ray at time,  $t_2$ ,

reveals a distorted wavefront that is no longer flat. The resulting wavefront is due to a random process; the distribution of turbulence eddies (circles) depends on random atmospheric temperature, pressure, and wind effects that vary with time and space.

### 2.2.2 Characteristics of Tilt Distortion

Wavefront distortions comprise three primary observed effects in reference to distant starlight: twinkling, spreading, and jittering [7]. The focus of this research involves the jittering effect which is the rapid and random movement of a light source in response to wavefront tilt distortion.

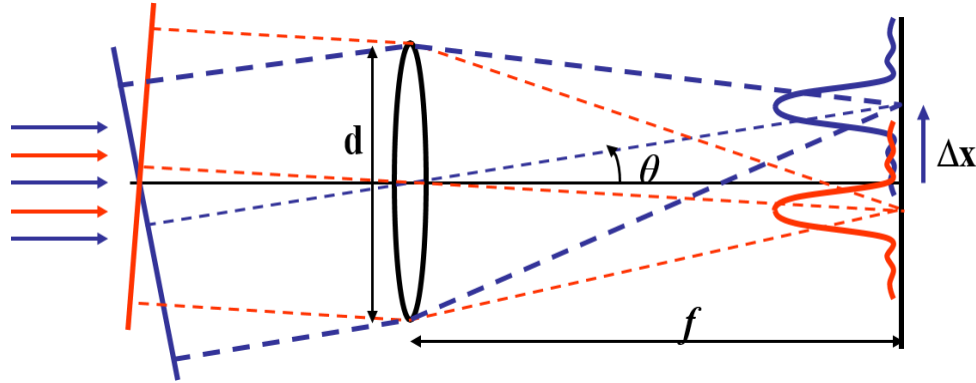


**Figure 3 - The red and blue wavefronts represent two different instances of tilt distortion over the lens diameter,  $d$ , [8].**

Notice the distinguishable effect of tilt distortion in figure 3; since the red and blue light rays intercept the optical axis at different angles, the lens focuses the rays to different locations in the focal plane. Effectively, the distortions randomly tilt incident wavefronts to an optical system. The observed result, tilt distortion, displaces the focused intensity spot by a displacement,  $\Delta x$  or  $\Delta y$ , from the optical axis. Since the small angle approximation is applicable, tilt angle,  $\theta$ , is accurately determined by taking the ratio of image displacement and focal length,  $f$ .

### 2.2.2.1 Tilt Distortion Process

Analogous to the turbulence process, tilt is also a random process described by spatial and temporal statistics. A normal distribution accurately captures the stochastic nature of wavefront distortions because there are so many independent realizations to make the Central Limit Theory applicable. The size of a telescope's aperture diameter controls how much tilt distortion enters an optical system, thus governing the tilt process's variance envelope. Atmospheric turbulence strength in addition to a telescope's operating bandwidth, slew rate, observation range, and zenith angle determine how fast the process cycles from one tilt instance to another.

### 2.2.2.2 Tilt Distortion Spatial Variance

Tilt distortion variance over an aperture diameter,  $D$ , typically takes on values according to

$$\sigma_{G\_tilt}^2 = 0.839 \left( \frac{D}{r_o} \right)^{5/3}, \quad (2.1)$$

where  $G\_tilt$  refers to measuring the average (global) phase gradient or average tilt distortion over an aperture [9].

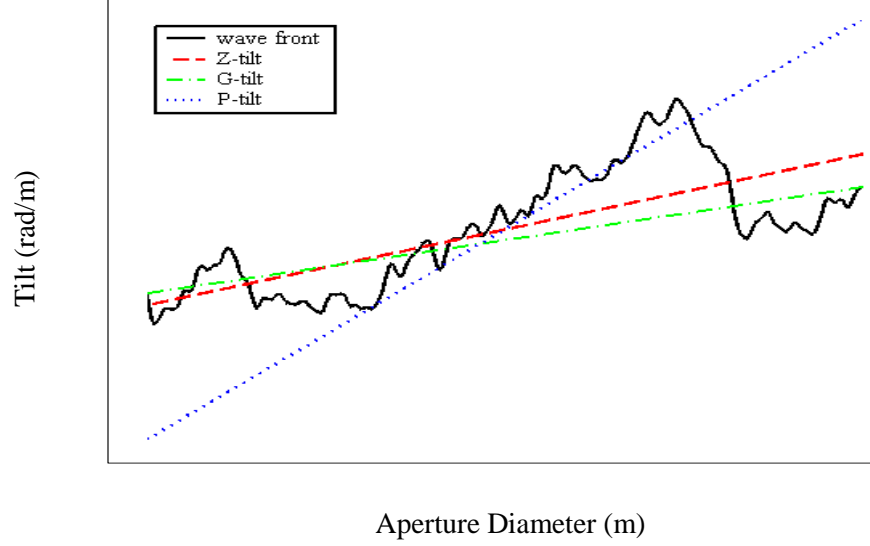


**Figure 4 - The dashed and dotted lines are *Z-tilt*, *G-tilt*, and *P-tilt* measures for tilt phase distortion where the black curve is the 1-D representation of tilt phase distortion over an aperture [8]**

Figure 4 presents typical measures of aperture tilt where *G-tilt* is shown as the dashed-dotted line for the average aperture phase slope. *Z-tilt* (dashed-line) measures tilt by best fitting a plane thru the aperture phase where orthogonal Zernike polynomials represent  $x$  and  $y$  plane components. *P-tilt* (dotted-line) corresponds to measuring the maximum or peak tilt of the aperture phase.

Fried's coherence parameter,  $r_0$ , of equation (2.1) defines a baseline for aperture diameters. Diameters much smaller than  $r_0$  allow optical systems to approach diffraction limited performance [9]. Consequently, a diameter exceeding  $r_0$  offers no resolution improvement; this condition couples more phase distortions into the system at one time, thereby increasing the spatial tilt variance. For astronomical telescopes having aperture diameters up to several meters and  $r_0$  values of 5 to 20 centimeters, the tilt distortion variance is considerable. Equation (2.1) expresses equal contributions from both  $x$  and  $y$  tilt distortions; the additive nature infers that the tilts are independent.

### 2.2.2.3 Tilt Distortion Temporal Dynamics

Tilt dynamics correlate to atmospheric dynamics that are modeled by a turbulence profile,  $C_n^2$ . A profile models turbulence strength and serves as a parameter for the refractive index structure function. Therefore, the profile appropriately adjusts the spatial statistics due to turbulence based on effective wind speed (atmospheric wind speed + telescope slew speed),  $v$  (m/s), and altitude,  $h$  (km), observation path from source to destination. An optical system's location, time of day for viewing, and type of viewing determine which profile to use. Typically, turbulence is greatest during the daytime period and near the ground and jet stream regions but dissipates rapidly for heights greater than the jet stream region.

This research uses a particular  $C_n^2$  profile, the Hufnagel-Valley (5/7) or H-V 5/7, given by

$$C_n^2(h) = 0.00594 \left( \frac{v}{27} \right)^2 (10^{-5}h)^{10} e^{-h/1000} + 2.7 \times 10^{-16} e^{-h/1500} + C_n^2(0) e^{-h/100}, \quad (2.2)$$

where the H-V 5/7 profile assumes night-time vertical viewing (zenith angle,  $\beta = 0$ ) and a center-band operating wavelength,  $\lambda$  (0.5 microns), which is appropriate for some astronomical telescopes [9],[10]. Additionally, coherence parameters corresponding to the 5/7 are

$$r_0(\lambda) = 5 \text{ cm}; \theta_0(\lambda) = 7 \mu\text{m} \quad \text{for} \quad \begin{cases} \beta = 0 & (\text{degrees}) \\ v_{avg} = 21 & (\text{m/s}) \\ \lambda = 0.5 & (\text{microns}) \\ C_n^2(0) = 1.7 \times 10^{-14} & (\text{m}^{-2/3}) \end{cases} \quad (2.3)$$

These values are a baseline and valid at the specified parameters; however, they vary inversely with turbulence strength. The isoplanatic angle,  $\theta_0$  ( $\mu\text{rad}$ ), is the angular analogue to  $r_0$ . It represents the maximum angle two sources can be separated and still be viewed

thru the same turbulence “window”. Equivalently and particularly relevant to this research,  $\theta_0$  as seen from the telescope, is the maximum angle the LEO object can traverse thru for its light rays to experience similar phase distortion.

The tilt distortion power spectral density (PSD) utilizes the  $C_n^2$  profile to capture temporal dynamics of tilt as follows [9],

$$\begin{aligned} P_G(f) &= 0.804D^{-1/3} \sec \beta f^{-2/3} \int_0^L C_n^2(h) v^{-1/3} dh \quad (f < f_{BW}) \\ P_G(f) &= 0.0110D^{-1/3} \sec \beta f^{-11/3} \int_0^L C_n^2(h) v^{8/3} dh \quad (f > f_{BW}) \end{aligned} \quad (2.4)$$

Equation (2.4) integrates over the vertical path, taking into account each turbulence layer contribution. Previously defined telescope parameters, ( $D$  and  $\beta$ ), further refine the one-axis PSD of equation (2.4). The piece-wise nature of the PSD reflect a change in slope about  $f_{BW}$ , the effective bandwidth for tilt distortion over the defined frequency region. Frequencies higher than  $f_{BW}$  correspond to a steeper attenuation of tilt distortion. Once telescope and atmospheric parameters are set, the PSD portrays the power of tilt distortion dynamics versus frequency,  $f$ .

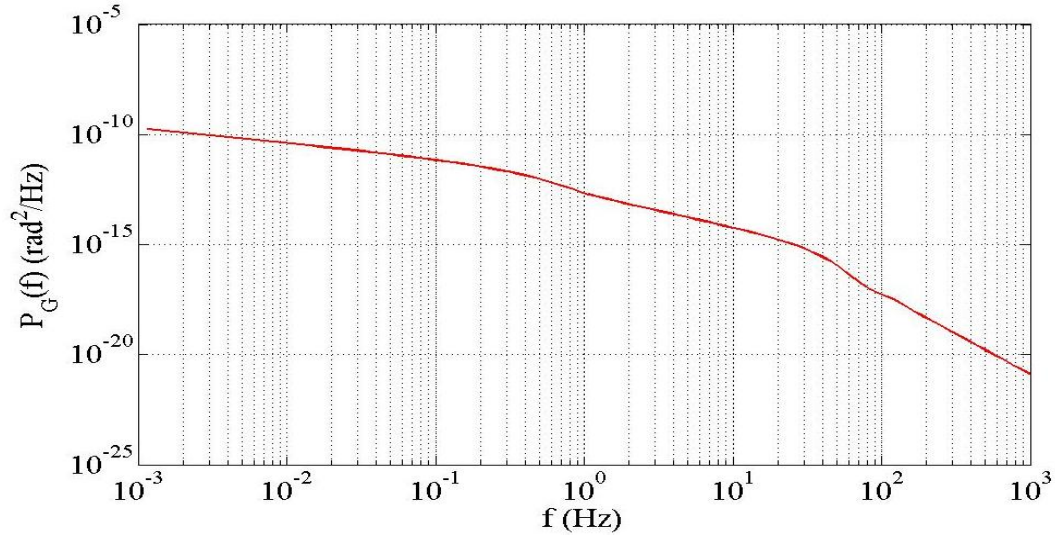


**Figure 5 - G-tilt PSD where it shows  $f_{BW} = 44.2$  Hz**

The tilt PSD of figure 5 indicates that tilt distortion is a low frequency phenomenon. The PSD has a signature low pass filter characteristic; it indicates that tilt distortion cycling faster than 44 Hz contribute negligibly to the overall jittering effect experienced by the optical system. This realization guides requirements on tilt measurement and compensation, specifically bandwidth or how fast the tilt tracker needs to operate in order to adequately abate tilt distortion.



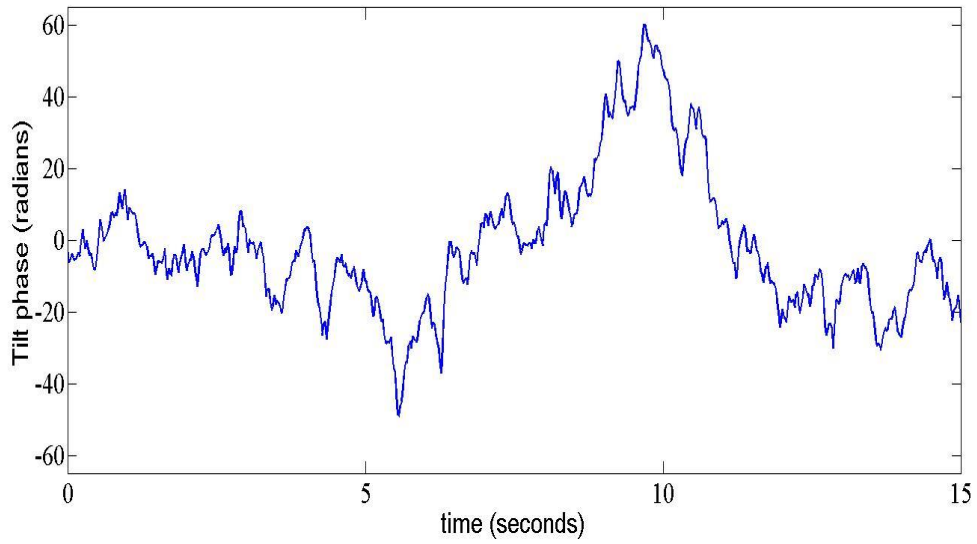


**Figure 6 - Random process of tilt distortion that is defined by the  $G$ -tilt spatial variance and PSD parameters for a vertical slewing telescope**

Figure 6 shows a random tilt process where the tilt instances take on values according to a specified  $G$ -tilt spatial variance. Over the 15 second measurement period, the process cycles from one tilt instance to another according to the  $G$ -tilt PSD. The accuracy of tilt measurements ultimately depends on sensor characteristics; this research considers the QUAD-cell detector.

### 2.3 Tilt Measurement With QUAD-cells

As previously stated, tilt distortion shifts intensity spots from the optical axis as indicated by figure 3. Figure 7 presents the same effect but from the perspective of the QUAD-cell detector located at the focal plane.

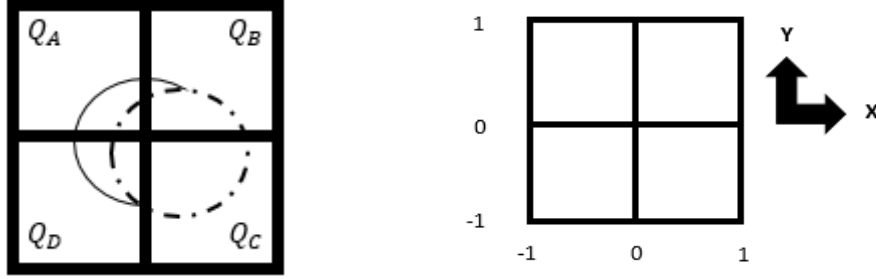


**Figure 7 - QUAD-cell configuration measuring spot intensity shifts amongst the four cells ( $Q_A$ ,  $Q_B$ ,  $Q_C$ , and  $Q_D$ )**

The QUAD-cell creates a Cartesian coordinate system as in figure 7 with an ordered pair,  $(\hat{I}_x, \hat{I}_y)$ , to track spot intensity shifts. Each coordinate ranges from negative to positive one and represents the intensity center of mass in the  $x$  and  $y$  directions as follows [7],

$$I_i = \iint I_{total} dS_i \quad (2.5)$$

$$\begin{aligned} \hat{I}_x &= \frac{\Sigma(I_B + I_C) - \Sigma(I_A + I_D)}{I_{total}} \\ \hat{I}_y &= \frac{\Sigma(I_A + I_B) - \Sigma(I_D + I_C)}{I_{total}}, \end{aligned} \quad (2.6)$$

where  $\hat{I}_x$  simply considers the normalized intensity difference between the right and left half planes in reference to the total QUAD-cell intensity,  $I_{total}$ ; similarly,  $\hat{I}_y$  determines the difference between the top and bottom half planes.

First, consider the diffraction limited amplitude spread function (ASF), the Fourier transform of the pupil function having no aberrations [11],

$$h(u, v) = \frac{1}{\lambda z_i} \iint_{-\infty}^{\infty} P(x, y) e^{-j2\pi(xf_x + yf_y)} dx dy \stackrel{\text{def}}{=} \frac{1}{\lambda z_i} \mathcal{F}\{P(x, y)\}, \quad (2.7)$$

where  $P(x, y)$  is the pupil of an optical system;  $z_i$  is the image plane distance from the pupil plane;  $\lambda$  is wavelength;  $f_x$  and  $f_y$  are pupil plane spatial frequencies. The ASF is a system's

coherent impulse response, taking into account geometric, diffraction, and aberration optical effects.

Now, consider the ASF when the image plane experiences displacements,  $\Delta u$  and  $\Delta v$ , due to tilt distortion,

$$h(u - \Delta u, v - \Delta v) = \frac{1}{\lambda z_i} \mathcal{F}\{P(x, y) e^{j2\pi(\Delta u f_x + \Delta v f_y)}\} = \frac{1}{\lambda z_i} \mathcal{F}\{\mathcal{P}(x, y)\} \quad (2.8)$$

In accordance with Fourier transform principles, a spatial shift in the image plane corresponds to a phase shift in the pupil plane as follows,

$$e^{j2\pi(\Delta u f_x + \Delta v f_y)} = e^{j(\phi_{\text{tilt}_x} + \phi_{\text{tilt}_y})} \quad (2.9)$$

The phase shifts correspond to tilt phase distortions,  $\phi_{\text{tilt}_x}$  and  $\phi_{\text{tilt}_y}$ , that cause image plane displacements,  $\Delta u$  and  $\Delta v$ . The general pupil function,  $\mathcal{P}(x, y)$ , accounts for these phase distortions. However, QUAD-cell's do not measure optical fields and therefore cannot determine tilt phase directly; instead, they estimate wavefront slope by sensing normalized differential intensity signals,  $\hat{I}_x$  and  $\hat{I}_y$ .

This research involves measuring average wavefront tilt,  $G_{\text{tilt}}$ , over the telescope's aperture diameter,  $D$ , given by

$$W_{\text{avg}_x} = \frac{1}{D} \int_{-D/2}^{D/2} \frac{\partial \phi(x, y)}{\partial x} dr \hat{i} \quad (2.10)$$

$$W_{\text{avg}_y} = \frac{1}{D} \int_{-D/2}^{D/2} \frac{\partial \phi(x, y)}{\partial y} dr \hat{j} \quad (2.11)$$

Since  $x$  and  $y$  tilt distortions are orthogonal to one another, the total average tilt represents a randomly tilted rectilinear plane,

$$W_{\text{avg}}(x, y) = W_{\text{avg}_x} + W_{\text{avg}_y} \quad (2.12)$$

The QUAD-cell's differential intensity measurements,  $\hat{I}_x$  and  $\hat{I}_y$ , relate to average wavefront tilt as follows,

$$\widehat{W}_x = \frac{\hat{I}_x}{Kg_x f} \quad (2.13)$$

$$\widehat{W}_y = \frac{\hat{I}_y}{Kg_y f}, \quad (2.14)$$

where centroid gains,  $K_{g_x}$  and  $K_{g_y}$ , determine how responsive the QUAD-cell is to tilt disturbances. Focal length,  $f$ , is the distance from the aperture to the detector plane; it also determines the extent of tilt disturbance experienced at the detector.

## 2.4 QUAD-cell Characteristics

### 2.4.1 Justification for QUAD-cells

Optical systems employ QUAD-cells, a detector with a four cell or pixel array configuration, to maximize signal to noise ratio (SNR) and frame rates during low photon flux conditions. For a charge-coupled device (CCD) array, the SNR is as follows [7],

$$SNR_v = \frac{N_s}{\sqrt{N_s + N_p(n_B + n_D + n_e^2)}} \quad (2.15)$$

$$N_s = \varphi_{photon} T Q_e \quad (2.16)$$

The signal level,  $N_s$  (photo-electron counts), and corresponding shot noise,  $\sqrt{N_s}$ , are functions of photon flux,  $\varphi_{photon}$ ; detector sampling interval,  $T$ ; and quantum efficiency,  $Q_e$ . The number of CCD pixels,  $N_p$ , determine how much inherent system noise factors into the  $SNR_v$  metric, where  $n_B$  is background noise,  $n_D$  is dark current noise, and  $n_e$  is read noise.

Taking the derivative of  $SNR_v$  with respect to  $N_p$  shows the dynamic of its inverse relationship to increasing numbers of detector pixels. Figure 8 displays the normalized magnitude of the derivative for three different values of  $N_s$  and fixed values for system noise parameters.

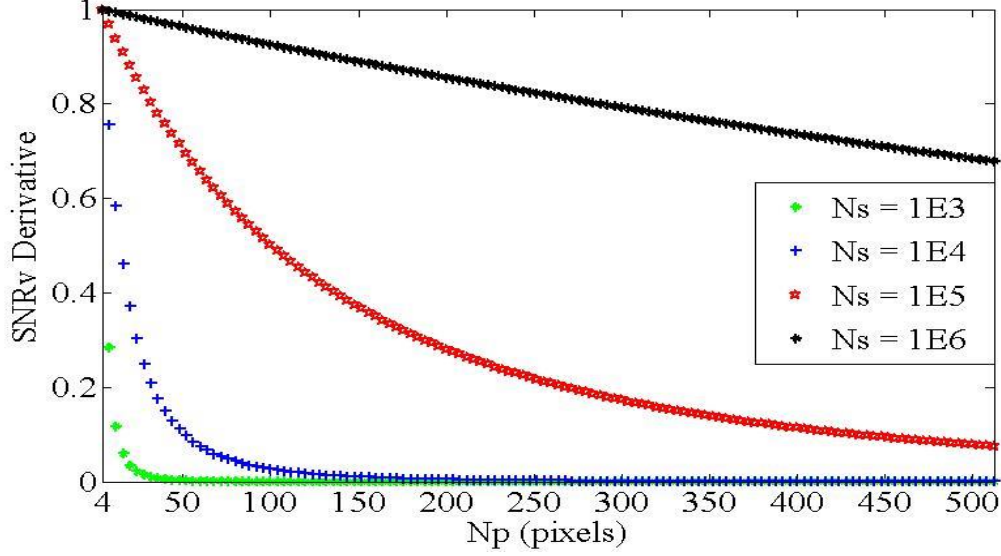


**Figure 8 - Normalized magnitude of  $SNR_v$  derivative for different signal levels**

Notice the derivative decays more precipitously to zero and is intolerant to even a modest increase in pixel numbers above ( $N_p = 4$ ) for lower signal levels. The zero level represents when noise completely overcomes the signal due to excessive pixel numbers, thereby driving  $SNR_v$  to zero. Additionally, figure 8 indicates a QUAD-cell is the minimum usage of pixels for an array. Correspondingly, this maximizes detector  $SNR_v$  and frame rates. As discussed later, the advantage of maximizing  $SNR_v$  is to minimize QUAD-cell measurement error thereby optimizing tilt tracker performance. Additionally, frame rate is a metric for how fast a detector samples an input, processes, then “reads-out” the output to a system [12]. The frame rate inherently induces control loop delays that are detrimental

to a tilt tracker's stability and robustness. A QUAD-cell is able to operate with high frame rates while maintaining an adequate  $SNR_v$ ; the advantage is that the control loop delay is minimized. The listed advantages do come at the expense of a severely degraded detector resolution, however.

### 2.4.2 Shannon-Nyquist Sampling Violation

To demonstrate the QUAD-cell's sampling behavior, consider the intensity distribution of a Gaussian laser source given by [13],

$$I(x, y, z) = I_0 \left( \frac{W_0}{W(z)} \right)^2 \exp \left( \frac{-2(x^2 + y^2)}{W^2(z)} \right), \quad (2.17)$$

where  $I_0$  and  $W_0$  correspond to initial intensity and beam radius parameters at a location ( $z=0$ ) that corresponds to a plane where the beam's wavefront is flat. The focused spot has a radius [13]

$$r(z_L) = \frac{f\lambda}{\pi W(z_L)}, \quad (2.18)$$

with parameters focal length,  $f$ , wavelength,  $\lambda$ , and beam radius,  $W(z_L)$ , at the location of the lens,  $z_L$ . The beam radius is the  $1/e^2$  point of  $I(x, y, z)$  and therefore band limited. Accordingly, the spatial frequency,  $f_{source}$  ( $m^{-1}$ ), of the signal is  $1/r(z_L)$ . The Shannon-Nyquist sampling theorem implies that in order to unambiguously determine the spot radius,  $r(z_L)$ , a detector must sample the spot with frequency,  $f_{detector}$ , that is at least twice  $f_{source}$ .

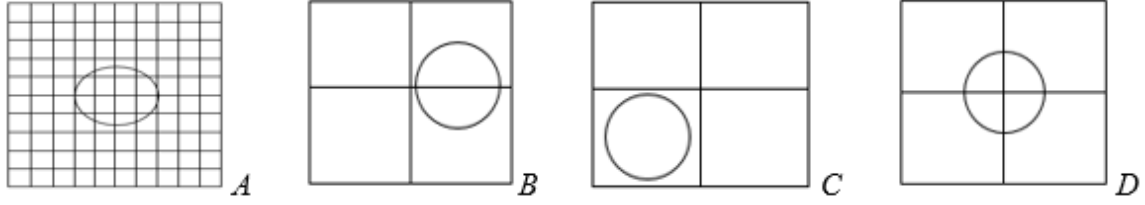


**Figure 9 - Detector A indicates proper sampling; the spot illuminates two pixels for QUAD-cell B, the spot illuminates one pixel for QUAD-cell C, the spot illuminates four pixels for QUAD-cell D**

In figure 9, detector A indicates proper pixel sampling with at least two pixels across the spot's radius in every direction; the detector maintains this sampling relationship regardless of spot displacement. The pixel configurations for detectors B, C, and D show the QUAD-cell's coarse sampling behavior and its inability to determine spot size. Notice the QUAD-cell provides three different results for the same spot; this indicates that QUAD-cell sampling depends on spot location. In general, the intensity distribution from a LEO object is not Gaussian and this adds an additional layer of complexity when utilizing the QUAD-cell.

### 2.4.3 Performance With Asymmetrical Intensity Distributions

The intensity distributions from a LEO object may be asymmetrical as shown by a satellite's y-dimension distribution in figure 10,

$$I(y) = \sum_i^n A_i \exp\left(\frac{-(y-\bar{y}_i)^2}{2\sigma_i^2}\right), \quad (2.19)$$

where the distribution can be represented by a mixture of independent Gaussians having various amplitudes  $\{A_i\}$ , variances  $\{\sigma_i^2\}$ , and means  $\{\bar{y}_i\}$ .

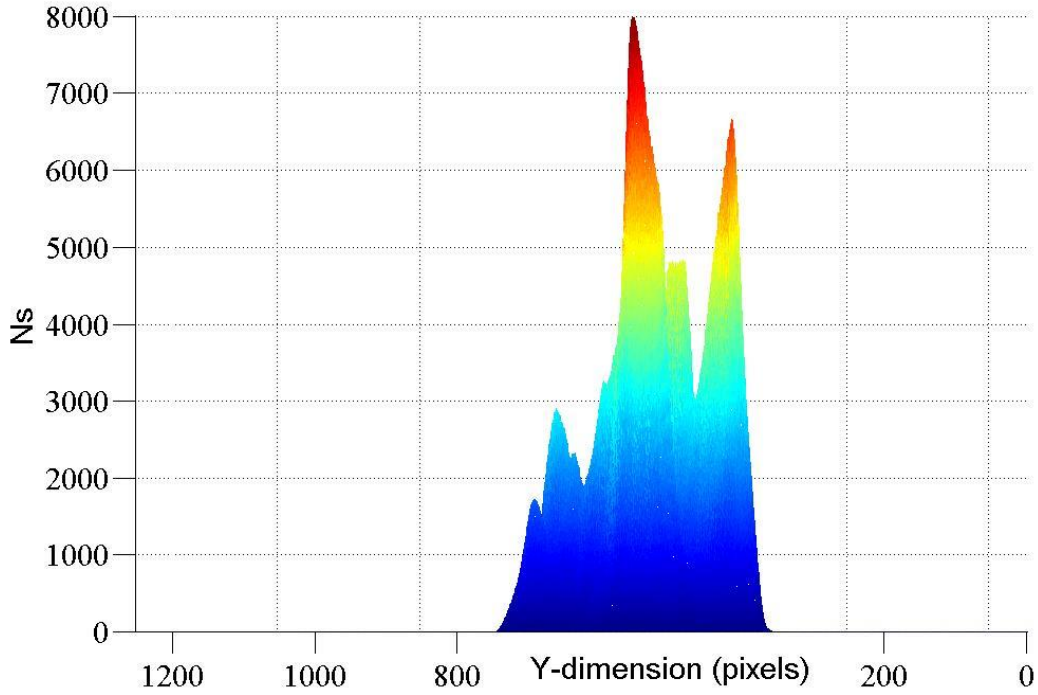


**Figure 10 - Asymmetrical intensity distribution of a LEO satellite object**

The QUAD-cell's measurement performance depends on signal intensity distribution; this is revealed by equating measured tilt,  $\widehat{W}$ , to theoretical tilt,  $W$ ,

$$\widehat{W} = \frac{\hat{I}}{K_g f} \quad (2.20)$$

$$W = \frac{\Delta a}{f} \quad (2.21)$$

Given fixed parameters for centroid gain,  $K_g$ , focal length,  $f$ , and displacement,  $\Delta a$ ,  $\hat{I}$  relates to  $\Delta a$  thru a linear relationship,

$$|\hat{I}| = K_g |\Delta a| \quad (2.22)$$

The assumptions being made are that the QUAD-cell operates in its linear region such that  $\hat{I}$  is proportional to  $\widehat{W}$  thru  $K_g$ ;  $K_g$  is optimal to make a perfect measurement of  $W$ ;  $\Delta a$  must map to a unique  $W$ .



The linear relationship of equation (2.22) means that a particular displacement, regardless of direction, must map to a unique  $|\hat{I}|$ . This condition is only satisfied for an intensity distribution that is symmetric about the QUAD-cell region as is the Gaussian distribution,

$$I(x, y) = \exp\left(\frac{-(x-x_0)^2}{2\sigma_x^2}\right) \exp\left(\frac{-(y-y_0)^2}{2\sigma_y^2}\right) \quad (2.23)$$

For the satellite intensity profile in figure 10, notice that a shift,  $|\Delta a|$ , to the right yields a different QUAD-cell result,  $|\hat{I}|$ , for the same shift to the left. This inconsistency induces unpredictable measurement errors and demonstrates a significant drawback when using the QUAD-cell to measure tilt distortion from a LEO object that has an asymmetrical intensity distribution. The preceding analysis did not directly consider the intensity spot size; the next section demonstrates that spot size also determines QUAD-cell measurement performance.

#### 2.4.4 Centroid Gain Dependence on Spot Characteristics

Up to this point, a QUAD-cell's centroid gain,  $K_g$ , has been taken as a constant; however, it does vary with spot size. This is revealed by imaging a Gaussian laser source with the ASF having tilt distortion as follows,

$$N_0 \exp\left(\frac{-2[(u-\Delta u)^2 + (v-\Delta v)^2]}{W^2(z)}\right) = N_0 \exp\left(\frac{-2(x^2 + y^2)}{W^2(z)}\right) \otimes h(u - \Delta u, v - \Delta v) \quad (2.24)$$

The convolution operation models imaging. The Gaussian source, originally having zero means, gets displaced by the coherent impulse response (ASF) such that it now has means,  $\Delta u$  and  $\Delta v$ . Here, the intensity distribution is treated as a two-dimensional photon counting

histogram having 1024 X 1024 pixels serving as bins; reference figure 11. The maximum photon arrivals is  $N_0$ .

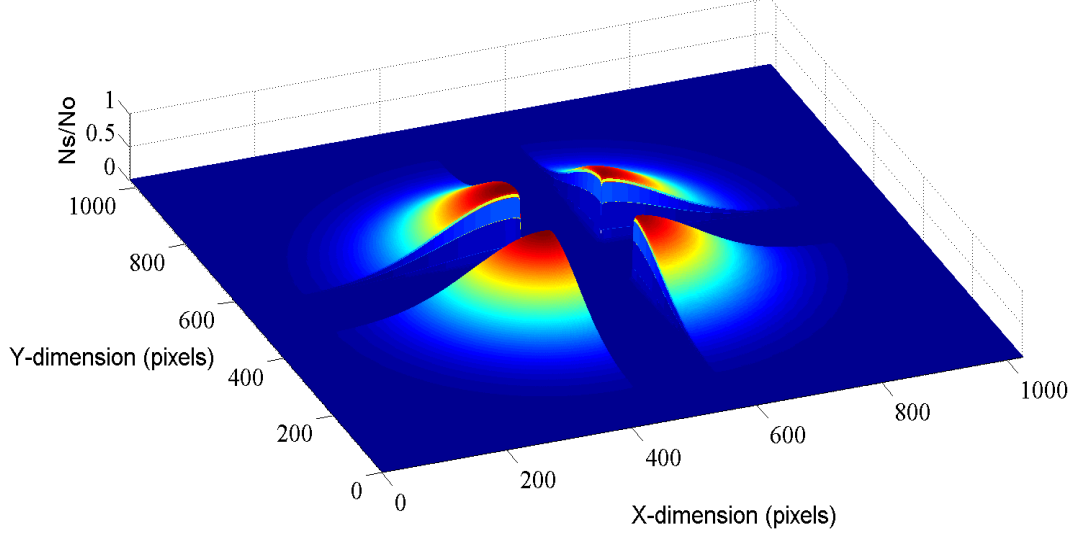


**Figure 11 - QUAD-cell partitions intensity distribution from a Gaussian laser source into four cells to measure tilt distortion**

As in figure 11, a QUAD-cell partitions the photon histogram into four regions, ( $Q_A$ ,  $Q_B$ ,  $Q_C$ , and  $Q_D$ ), to measure histogram displacements. To measure  $\hat{I}_x$ , take sums of the photons corresponding to the right and left half planes of the detector; integrating over an infinite number of bins makes the calculations tractable,

$$I_B + I_C = \left\{ N_0 \int_0^\infty \exp\left(-\frac{2u^2}{w^2(z)}\right) du \int_{-\infty}^\infty \exp\left(-\frac{2v^2}{w^2(z)}\right) dv \right\} + \Delta I(\Delta u) \quad (2.25)$$

$$I_A + I_D = \left\{ N_0 \int_{-\infty}^0 \exp\left(-\frac{2u^2}{w^2(z)}\right) du \int_{-\infty}^\infty \exp\left(-\frac{2v^2}{w^2(z)}\right) dv \right\} - \Delta I(\Delta u) \quad (2.26)$$

The original intensity distribution was equally distributed between left and right half planes; however, the tilt has shifted the distribution in favor of the right half plane. Notice the intensity shift increased the intensity (photon counts) in the right half plane by  $\Delta I(\Delta u)$ , while it decreased the intensity of the left half plane by the same amount. Of course, this

assumes the entire intensity distribution remains on the QUAD-cell. Therefore, equations (2.25) and (2.26) contribute the appropriate  $\Delta I(\Delta u)$  to the original half plane intensity distributions.

The total intensity,  $I_{total}$ , and normalized differential intensity,  $\hat{I}_x$ , are as follows,

$$I_{total} = N_0 \iint_{-\infty}^{\infty} \exp\left(-\frac{2(u^2+v^2)}{W^2(z)}\right) dudv = W(z)N_0\sqrt{\frac{\pi}{2}} \quad (2.27)$$

$$\hat{I}_x = \frac{(I_B+I_C)-(I_A+I_D)}{I_{total}} = \frac{2\Delta I(\Delta u)}{W(z)N_0\sqrt{\frac{\pi}{2}}} \quad (2.28)$$

The  $\Delta I(\Delta u)$  term corresponds to the magnitude of intensity change by shifting the intensity distribution to a new mean;  $\Delta u$  reflects the new mean since the change is referenced from a mean of zero. The resulting integral cannot be evaluated in closed form and is estimated by a Maclaurin series approximation for the Gaussian error function,  $\text{erf}(z)$ ,

$$\Delta I(\Delta u) = \left| N_0 \int_0^{\Delta u} \exp\left(\frac{-2u^2}{W^2(z)}\right) du \right| = \left| N_0 \int_{-\Delta u}^0 \exp\left(\frac{-2u^2}{W^2(z)}\right) du \right| = \frac{N_0 W(z)}{2} \sqrt{\frac{\pi}{2}} \text{erf}\left(\frac{\sqrt{2}\Delta u}{W(z)}\right) \quad (2.29)$$

$$\text{erf}(z) \approx \frac{2}{\sqrt{\pi}} \left( z - \frac{1}{3}z^3 + \frac{1}{10}z^5 - \frac{1}{42}z^7 + \frac{1}{216}z^9 - \dots \right) \quad (2.30)$$

The assumption that the ratio,  $\sqrt{2}\Delta u/W(z)$ , is much less than one is valid because  $W(z)$  is usually at least two orders of magnitude larger than  $\Delta u$ . Therefore, this allows one to discard powers higher than one of the series as follows,

$$\frac{\sqrt{2}\Delta u}{W(z)} \ll 1 \xrightarrow{\text{yields}} \text{erf}(z) \approx \frac{2}{\sqrt{\pi}}z \quad (2.31)$$

$$2\Delta I(\Delta u) \approx N_0 W(z) \sqrt{\frac{\pi}{2}} \frac{2}{\sqrt{\pi}} \frac{\sqrt{2}\Delta u}{W(z)} = 2N_0\Delta u \quad (2.32)$$

Applying the normalized differential intensity equation (2.28) yields that  $\hat{I}_x$  is linearly related to displacement,  $\Delta u$ , through a proportional term,  $K_{g_x}$ ,

$$\hat{I}_x = \frac{1}{\sqrt{\frac{\pi}{8}} W(z)} \Delta u \xrightarrow{\text{yields}} K_{gx} \Delta u \quad (2.33)$$

However, recall this result came by way of taking the  $\sqrt{2}\Delta u/W(z)$  ratio to be much less than one. If  $\Delta u$  becomes “large” or spot size,  $W(z)$ , becomes “small”, the ratio may take on values comparable to or larger than one. Then, one could not neglect the higher order terms in the Maclaurin series and equation (2.30) becomes non-linear. The same results follow for  $\hat{I}_y$ .

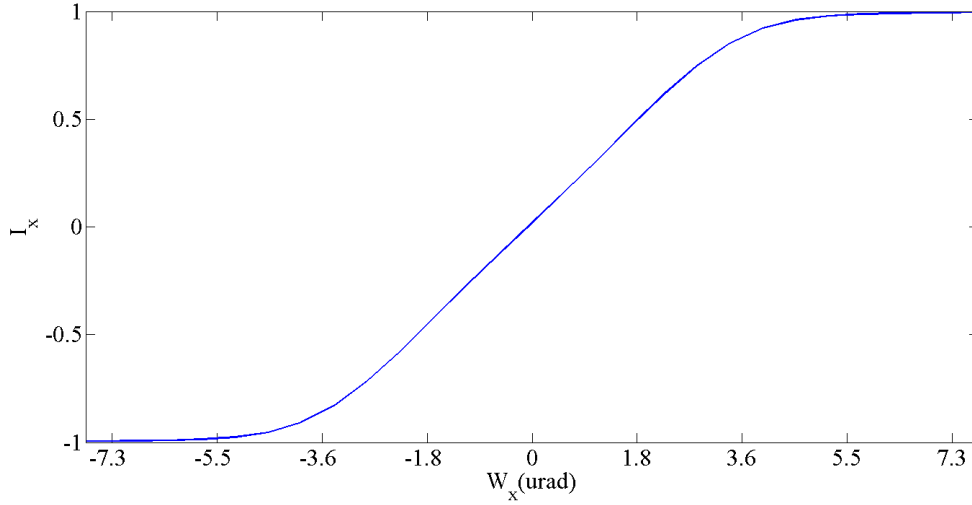


**Figure 12 - PTS response curve revealed by plotting  $\hat{I}_x$  versus  $W_x$**

Figure 12 plots  $\hat{I}_x$  versus  $W_x$ ; where the response curve that corresponds to  $K_g$  has linear and non-linear regions. Linear regions correspond to when  $\Delta u$  is kept “small” relative to spot size and detector plane dimensions. The non-linear regions correspond to saturation zones when  $\Delta u$  is “large” or  $W(z)$  is “small” relative to detector dimensions. As this work set out to show,  $K_g$  depends inversely with spot size,  $W(z)$ . This is intuitive because for a given tilt disturbance, a “large” spot size becomes less sensitive to

disturbance than a “small” spot size; essentially, the large spot would seem to displace less by inducing a smaller intensity shift. Therefore,  $K_g$ , is a sensitivity or gain term.

$$K_g \sim \frac{1}{W(z)} \quad (2.34)$$

Of course, the QUAD-cell does not operate stand-alone; it operates in concert with other optical components to realize an adaptive optics effect. As presented in the next section, the QUAD-cell’s characteristics, particularly its centroid gain, affect tilt tracker performance.

## 2.5 Adaptive Optics

### 2.5.1 Definition

Adaptive optics (AO) is a technology often employed by ground based telescopes to abate undesirable effects of atmospheric turbulence, particularly wavefront distortions. AO involves two real time processes, measurement and compensation. Measurement determines the wavefront phase distortion,  $\phi_{distortion}$ , of a complex optical field  $Ae^{-j(\phi_0 + \phi_{distortion})t}$ , where  $A$  is the field amplitude and  $\phi_0$  is the inherent field phase. Compensation involves applying a conjugate phase,  $\phi_{conjugate}$ , to null  $\phi_{distortion}$  such that the undistorted field,  $Ae^{-j(\phi_0)t}$ , is recovered.

### 2.5.2 Tilt Tracker

The focus of this research is a particular subsystem of an AO system, the tilt tracker. Tilt trackers counteract image jitter effects. Therefore, the tilt tracker only measures and compensates for tilt phase distortion,  $\phi_{tilt}$ . Without the tilt tracker, images are blurred as they “dance” randomly over a viewing cycle, effectively reducing image resolution and

intensity. The tilt tracker is only relevant for long exposure (LE) imaging systems where the shutter cycle exceeds the tilt cycle.

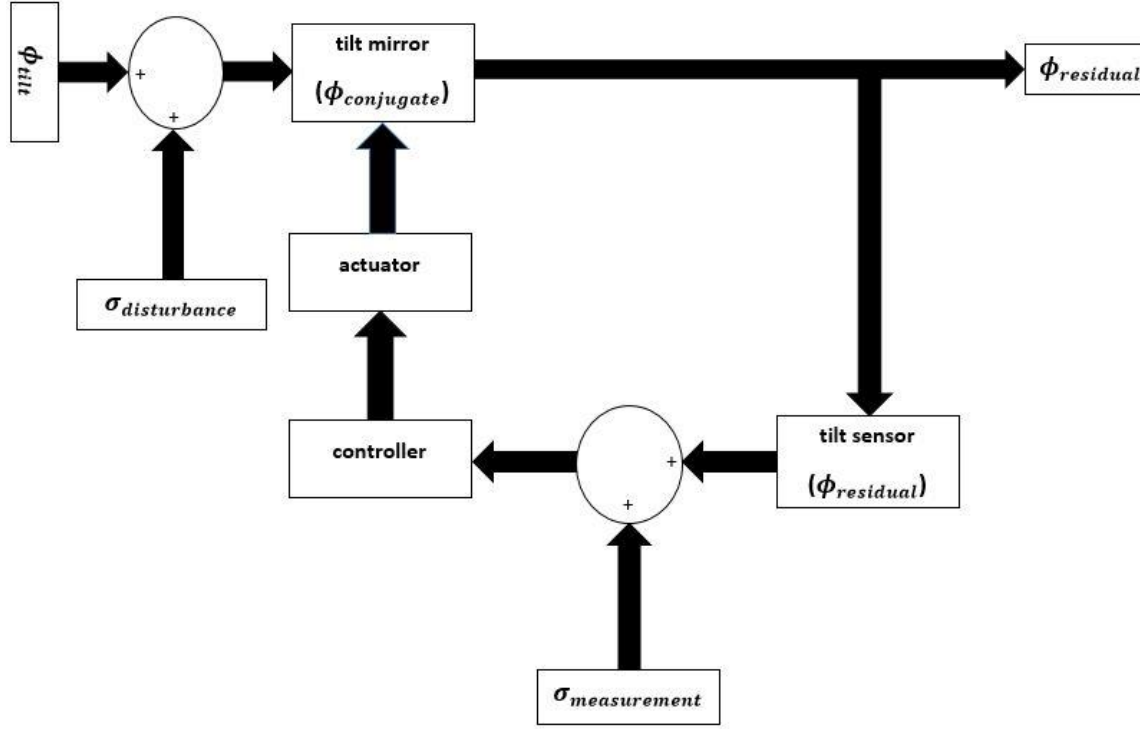


**Figure 13 - One-axis closed-loop tilt tracker schematic**

The schematic in figure 13 represents a general closed-loop (CL) control configuration with tilt mirror, tilt sensor, controller, and actuator components. The sensor assumes the tilt tracker's measurement role, while the mirror takes on the compensation role via controller commands. The CL configuration is ideal for closely tracking a random tilt process, represented as  $\phi_{tilt}$ , that is often corrupted by measurement and signal noise. CL operation allows the tracking system to respond to residual errors,  $\phi_{residual}$ , such that the dynamic range of the tilt mirror and sensor is kept relatively "small". This further translates to compact controller commands and an efficient actuator.

### 2.5.3 Tilt Tracker Performance

This work considers two persistent limitations for tilt tracker performance, residual tilt angle deviations due to temporal and measurement constraints. These constraints are represented as one-axis, one-sigma tilt angle deviations that remain after tilt compensation,

$$\sigma_{tracker} = \sqrt{\sigma_{temp}^2 + \sigma_{meas}^2}, \quad (2.35)$$

where the temporal and measurement variances are independent and contribute additively to the overall tilt angle tracker deviation,  $\sigma_{tracker}$  [7]. The temporal deviation,  $\sigma_{temp}$ , relates to tracker bandwidth requirements needed to measure and compensate for a highly dynamic tilt process when tracking a fast moving LEO object. Recall the QUAD-cell characteristics of Section 2.4 and note that deviations from optimal spot size, intensity distribution, and signal levels contribute significantly to the  $\sigma_{meas}$  term.

The tracker deviation relates to image quality through the long exposure Strehl ratio metric [2],

$$SR_{LE} = \left\{ 1 + \frac{\pi^2}{2} \left( \frac{\sigma_{tracker}}{\lambda/D} \right)^2 \right\}^{-1} \quad (2.36)$$

By definition, Strehl ratio,  $SR$ , is a ratio for the aberrated image's peak intensity versus the perfect or diffraction limited image's peak intensity. Since aberrations spread intensity distributions,  $SR$  ranges from zero to unity, where unity denotes an unaberrated image. Typically, the Strehl ratio is defined in terms of “point-like” sources and higher order aberrations than tilt distortion [7]. Recall that tilt distortion does not spread intensity distributions; rather, it can rapidly shift the distributions away from the optical axis to give an average peak intensity that is less than the diffraction limited value for LE images.

Therefore, the  $SR_{LE}$  only accounts for tilt distortion and is a useful metric to show how effective the tilt tracker is performing, even with extended objects.

### 2.5.3.1 Temporal Error

Adequate compensation for tilt distortion while considering tracker bandwidth efficiency, motivated the derivation of the Tyler frequency, the fundamental *G-tilt* tracking frequency [14],

$$f_{T_G} = 0.368D^{-1/6}(\sec \beta)^{1/2} \lambda^{-1} \left[ \int_0^L C_n^2(h) v^2 dh \right]^{\frac{1}{2}} \quad (2.37)$$

The frequency expresses the minimum tracker bandwidth to obtain a temporal, one-axis, one-sigma tilt angle deviation (*rms*),

$$\sigma_{temp} = \left( f_{T_G} / f_{3dB} \right) \left( \lambda / D \right), \quad (2.38)$$

that is equal to the diffraction angle [14] . This is seen by setting the effective tracker bandwidth,  $f_{3dB}$ , equal to  $f_{T_G}$ . The optical system's diffraction angle,  $\lambda/D$ , representing its diffraction limited resolving power, is an accepted baseline to assess tracker performance. Recall that jittering reduces resolving power because it randomly oscillates objects beyond the diffraction angle zone, making the blurring effect noticeable. However, if the tracker cages the jittering within the diffraction angle zone, the jitter will go undetected to the optical system. This is accomplished when the tracker's residual phase error correlates to a one-sigma tilt angle deviation of  $\lambda/D$  or less.

In practice,  $f_{3dB}$  is set to correspond to at least four times  $f_{T_G}$ [14]. However, its actual value depends on desired tracker performance and the  $f_{T_G}$  value. Notice the Tyler frequency's dependence on atmospheric and telescope parameters. To a certain extent,



these parameters are beyond a tilt tracker designer's control; therefore,  $f_{T_G}$  should be calculated for worst case scenarios, e.g. expected greatest turbulence, slew rate, and zenith angle.

### 2.5.3.2 Measurement Error

Section 2.4.4, Centroid Gain Dependence on Spot Characteristics, obtained a result for  $\hat{I}_x$  that depended on spot size,  $W(z)$ . This section extends that result to factor in  $SNR_v$  such that all significant factors for sensor measurement error are considered. A technique to reduce  $\hat{I}$  error during low flux conditions is to take the expectation of the denominator as follows [15],

$$\hat{I}_x = \frac{(I_B + I_C) - (I_A + I_D)}{E[I_{total}]} = \frac{2N_0\Delta u}{E\left[W(z)N_0\sqrt{\frac{\pi}{2}}\right]} = \frac{N_0\Delta u}{\sqrt{N_0}\sqrt{\frac{\pi}{8}}W(z)} = SNR_v K_{g_x} \Delta u \quad (2.39)$$

Since, photon arrivals,  $N_0$ , is Poisson distributed with mean and variance,  $\sqrt{N_0}$ , the  $SNR_v$  metric becomes apparent in equation (2.39) by noticing the following approximation,

$$SNR_v \approx \frac{N_0}{\sqrt{N_0}} = \sqrt{N_0} \quad (2.40)$$

Recall equation (2.15) for  $SNR_v$  and notice equation (2.40) is a valid approximation for a QUAD-cell with low inherent noise characteristics, that is shot noise,  $\sqrt{N_0}$ , is much more significant than the other noise terms in the denominator of equation (2.15).

Isolating the  $\Delta u$  term of equation (2.39), then dividing both sides of the resulting equation by focal length,  $f$ , provides the following expression for tilt that depends on  $SNR_v$  and  $K_{g_x}$  as desired,

$$\frac{\hat{I}_x}{SNR_v K_{g_x} f} = \frac{\Delta u}{f} = W_x, \quad (2.41)$$

where deviations from a given theoretical tilt,  $W_x$ , are due to deviations in spot size thru  $K_{g_x}$  and/or deviations in signal levels thru  $SNR_v$ . These results follow for  $\hat{I}_y$ .

Tyler and Fried exacted the following expression for tilt measurement inaccuracies while using a QUAD-cell to determine tilt distortion of an incoherently illuminated object [16],

$$\sigma_{meas} = \frac{\pi[(3/16)^2 + (n/8)^2]^{1/2}(\lambda/D)}{SNR_v} \quad (2.42)$$

$$n = \frac{(W(z)/f)}{(\lambda/D)}, \quad (2.43)$$

where the one-axis, one-sigma, error term is again referenced about the diffraction angle,  $\lambda/D$ , but intuitively depends inversely with  $SNR_v$ . As expected,  $\sigma_{meas}$  depends directly with spot size,  $W(z)$ , and this dependence is captured using equation (2.43), where the apparent object size is converted into factors of diffraction angle. However,  $\sigma_{meas}$  assumes a circular object and using it for an arbitrary LEO object is non-ideal; a more applicable measure is unknown to the author and this limitation is addressed in the methodology section.

The preceding discussions of  $\sigma_{temp}$  and  $\sigma_{meas}$  show that a tracker's performance is ultimately constrained by component limitations, particularly the tilt sensor. Assuming all other tracker components to be optimally chosen, the tilt sensor sets the stage for how accurate the tracker measures and compensates tilt distortion. Therefore, this work justifiably centers on suboptimal tracker performance due to tilt sensor limitations.

## 2.6 Centroid Gain Variance and Tracker Performance

Recall that the QUAD-cell's centroid gain,  $K_g$ , varies inversely proportional to intensity spot size,  $W(z)$ . Additionally,  $W(z)$  is an uncharacterized random variable defined by random atmospheric seeing and LEO object characteristics. Therefore,  $K_g$  assumes random values that may be less than optimal. To investigate its effect on tracker performance, consider the following CL tracker system incorporating  $K_g$  in figure 14.

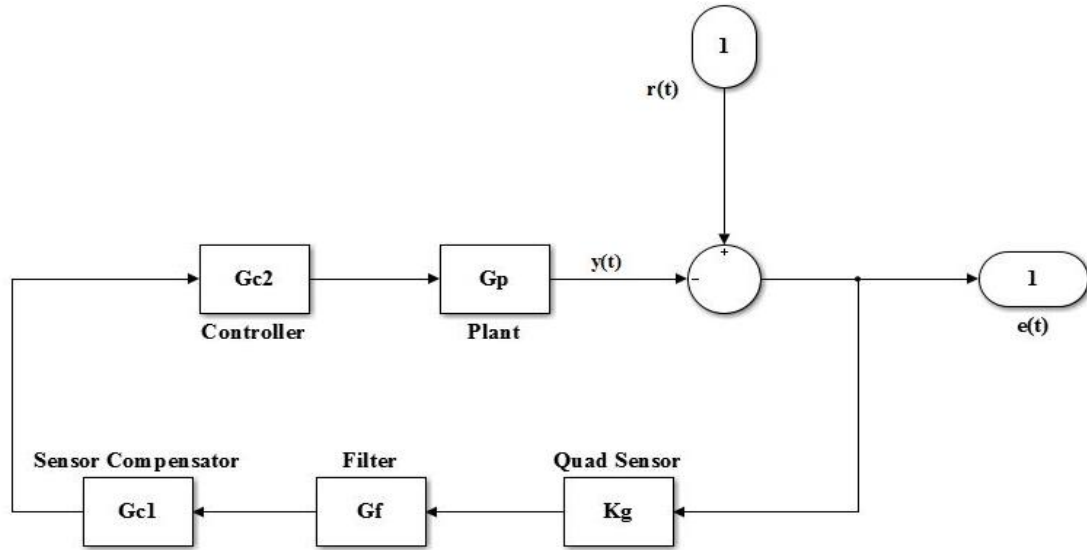


**Figure 14 - One-axis tilt tracker CL transfer function diagram**

The diagram in figure 14 translates the CL schematic from figure 13 to an interconnection of transfer functions to analyze the sensor's effect on tracker frequency response. A transfer function expresses a system's frequency dependent relationship between outputs and inputs. Each system block,  $(G_p, G_{c1}, G_{c2}, G_f, K_g)$ , is a transfer function corresponding to the component's linear time-invariant dynamic behavior, assumed to have zero initial conditions. Collectively, the component transfer functions define the tracker's CL transfer function as follows,

$$H(j\omega) = \frac{E(j\omega)}{R(j\omega)} = \frac{1}{1 + K_g G_p(j\omega) G_{c1}(j\omega) G_{c2}(j\omega) G_f(j\omega)}, \quad (2.44)$$

where  $H(j\omega)$  is the relationship between the output residual error signal,  $E(j\omega)$ , and the input reference signal,  $R(j\omega)$ .

Under the assumption that all the components are stable dynamic systems and have a collective behavior to realize a CL model with a bandwidth,  $\omega_{3dB}$ , corresponding to at least four times  $2\pi f_{T_G}$ , the model is as follows,

$$K_g G_p(j\omega) G_{c2}(j\omega) G_{c1}(j\omega) G_f(j\omega) = \frac{K_g}{K_{g\_opt}} K G'(j\omega)$$

$$H(j\omega) = \frac{1}{1 + \frac{K_g}{K_{g\_opt}} K G'(j\omega)} \quad (2.45)$$

$$H(j\omega) \approx \frac{1}{1 + \left( \frac{W(z)_{opt}}{W(z)} \right) K \left[ 1 + 2\zeta \frac{(j\omega)}{\omega_{3dB}} + \left( \frac{j\omega}{\omega_{3dB}} \right)^2 \right]^{-1}}$$

Specifically, the collective behavior approximates a second order system with design parameters of damping ratio,  $\zeta$ , and gain,  $K$ . The behavior further accounts for the effects due to a change in spot size. An optimal gain and spot size,  $K_{g\_opt}$  and  $W(z)_{opt}$ , correspond to optimal QUAD-cell measurements and a tracker operating with bandwidth,  $\omega_{3dB}$ . Considering two limiting cases for  $W(z)$  indicates two extremes of undesirable tracker performance,

$$\begin{cases} H(j\omega) \approx 1 & \text{for } (W(z) \gg W(z)_{opt}) \\ H(j\omega) \approx 1 - \frac{\Delta_{sat}(W(z), R(j\omega))}{R(j\omega)} & \text{for } (W(z) \ll W(z)_{opt}) \end{cases} \quad (2.46)$$

It is appropriate to view the tracker system as a filter whose role is to take an input tilt disturbance and provide a much attenuated output to the optical system,

$$E(j\omega) = H(j\omega) R(j\omega) \quad (2.47)$$

A “large”  $W(z)$  or a spot size comparable to the size of the sensor, makes the sensor insensitive to tilt disturbances and causes the tracker transfer function to nearly unity-pass tilt disturbances through the tracker system, such that the error approximates the reference signal

$$E(j\omega) \approx R(j\omega) \quad (2.48)$$

A “small”  $W(z)$  or a spot size comparable to a point source, makes the sensor hypersensitive and unstable. With even the slightest disturbance, the sensor saturates to a non-zero value. Although a small spot size implies a transfer function that provides significant attenuation, the opposite is true. Consider the error signal for a small spot,

$$E(j\omega) \approx R(j\omega) - \Delta_{sat}(W(z), R(j\omega)), \quad (2.49)$$

where the non-zero  $\Delta_{sat}$  term is the saturation signal that depends on spot size and reference signal. The overall effect gives a non-zero error signal corresponding to the difference between the reference and saturation signals.

## 2.7 Adaptive Tilt Tracker

The issues raised in the previous sections involving the tilt tracker motivate the need for an adaptive tilt tracker that is able to detect and compensate for deviations away from optimal settings. Suboptimal tracker performance due to measurement error can be decomposed into its two constituent contributors, suboptimal  $SNR_v$  and  $K_g$ .

To maintain a certain  $SNR_v$  and reduce noise coupling to the output at lower photon fluxes, the adaptive tilt tracker will adjust the frame rate,  $f_s$ , accordingly. Recall that the numerator term of the  $SNR_v$  equation (2.15) is a function of photon flux and frame rate for a given quantum efficiency,

$$N_s(V, f_s^{-1}) = \varphi_p(V) f_s^{-1} Q_e, \quad (2.50)$$

where now the photon flux is expressed explicitly as a function of  $V$ -mag. For the adaptive tilt tracker, the idea is to operate the PTS with a frame rate such that its signal to noise ratio can accurately be represented as,

$$SNR_v \approx \sqrt{N_s} \quad (2.51)$$

This work sets a threshold,  $SNR_{v_0}$ , defined as the minimum desired signal to noise ratio for  $V$ -mag,  $V_0$ , while operating at the maximum PTS frame rate,  $f_{max}$ .  $SNR_{v_0}$ ,  $V_0$ , and  $f_{max}$  represent design decisions to specify the dimmest  $V_0$  where  $SNR_{v_0}$  and  $f_{max}$  can be attained simultaneously; therefore, an arbitrary  $V$  above or below  $V_0$  will reflect in the resultant  $SNR_v$ .

Consider the following ratio, where an arbitrary  $SNR_v$  value is related to the threshold value,

$$\frac{SNR_v}{SNR_{v_0}} = \sqrt{\frac{\varphi_p(V) f_s^{-1} Q_e}{\varphi_p(V_0) f_{max}^{-1} Q_e}} = \left( \frac{\varphi_p(V) f_{max}}{\varphi_p(V_0) f_s} \right)^{1/2} \quad (2.52)$$

and recognize that plugging equation 2.50 into equation 2.51 transforms the  $SNR_v$  expressions to ones involving only frame rates and  $V$ -mags. Setting the  $SNR_v$  ratio equal to unity identifies the transition point as follows,

$$\frac{SNR_v}{SNR_{v_0}} = 1 \xrightarrow{\text{yields}} f_s(V) = \frac{\varphi_p(V)}{\varphi_p(V_0)} f_{max} \quad (2.53)$$

The transition point is where the PTS's frame rate needs to be adjusted lower than  $f_{max}$  when the  $SNR_v$  value dips below  $SNR_{v_0}$ .

$$\begin{cases} f_s = f_{max} & \text{for } SNR_v \geq SNR_{v_0} \\ f_s(V) = \frac{\varphi_p(V)}{\varphi_p(V_0)} f_{max} & \text{for } SNR_v < SNR_{v_0} \end{cases} \quad (2.54)$$

Accordingly, for  $SNR_v$  values equal to or above the threshold, the PTS operates with frame rate,  $f_{max}$ . For  $SNR_v$  values below the threshold, the adaptive tilt tracker adjusts the frame rate appropriately to restore at least a  $SNR_v$  value of  $SNR_{v_0}$ .

For deviations in spot size, consider the tracker transfer function explicitly incorporating the behavior of the sensor compensator,  $G_{c1}(j\omega)$

$$H(j\omega) \approx \frac{1}{1 + K_g K_c K \left[ 1 + 2\zeta \frac{(j\omega)}{\omega_{3dB}} + \left( \frac{j\omega}{\omega_{3dB}} \right)^2 \right]^{-1}}, \quad (2.55)$$

where  $K_c$  is compensator gain. Given an optimal tracker system, the compensator will adapt to changes in spot size by varying  $K_c$  in an effort to restore the optimal transfer function,

$$H(j\omega) \approx \frac{1}{1 + K \left[ 1 + 2\zeta \frac{(j\omega)}{\omega_{3dB}} + \left( \frac{j\omega}{\omega_{3dB}} \right)^2 \right]^{-1}} \quad (2.56)$$

To restore an optimal tilt measurement, the compensator applies a gain factor,

$$K_c = \frac{1}{K_{g\_opt}} \hat{I} / \tilde{I}, \quad (2.57)$$

where the origin of this term is from taking the ratio of the optimally measured tilt,  $\hat{W}$ , and the sub-optimally measured tilt,  $\tilde{W}$ ; that ratio is

$$\frac{\hat{W}}{\tilde{W}} = \frac{K_g}{K_{g\_opt}} \hat{I} / \tilde{I} \quad (2.58)$$

and solving for  $\hat{W}$  allows for  $K_c$  to be applied, given that the sensor gain is  $K_g$ . In order to apply the correct  $K_c$ , the adaptive tracker must sense a sub-optimal centroid gain thru estimating spot size; consider the following four methods.

## 2.8 Methods for Estimating an Arbitrary $K_g$

All the methods discussed here have been developed in reference to astronomical observatory AO systems having primary applications toward natural and/or laser guide stars. Additionally, these methods have been applied to higher order (aberrations) AO loops. However, these methods still provide a useful frame of reference for the different circumstances considered in this research: low order tilt distortion; a slewing telescope; a LEO object having asymmetrical and dynamic characteristics.

### 2.8.1 Utilize Focal Plane Array (FPA)

Using the FPA to measure spot size directly is the simplest of the four methods considered here. Its advantage is due to a passive and direct measuring technique, requiring no active control. As discussed in section 2.4.2, a FPA has enough pixels to sample spot size according to Nyquist sampling requirements. The Keck Observatory's laser-guide-star AO program uses an analogous technique for its higher order AO loop where a low bandwidth wavefront sensor (LB-WFS) uses a (16x16) pixel array for each sub-aperture instead of the typical (2x2) configuration [17]. A disadvantage for the FPA and LB-WFS lies with their usage of a greater number of pixels than a QUAD-cell; this results in noisy measurements of the spot size during low flux conditions and extended read times. The FPA may operate at much slower frame rates (tens of hertz) in order to provide enough signal for the pixel array; consequently, this increases process time to calibrate the tracker loop. Similarly, the LB-WFS is designed to operate with long exposure times and can average spot size measurements taken by each sub-aperture to reduce noise effects [17]. An additional concern when utilizing the FPA and LB-WFS, is that a percentage of the tilt



sensor's incident intensity may be diverted to the FPA or LB-WFS, which could be non-ideal for all sensors during low flux conditions.

### **2.8.2 Monitor Deformable Mirror (DM) Shape**

The average shape of the DM can be exploited to indirectly estimate deviations from the optimal centroid gain [18]. Typically, the wavefront measurement path of an optical train is on a different leg than the science camera. This often induces non-common path errors because the light experiences path dependent aberrations. Therefore, the DM is normally calibrated with a non-flat average shape to offset the errors. Veran and Herriot have demonstrated a strong correlation between average DM shape deviations and centroid gain deviations.

The origin of DM actuator voltage commands are from the Shack-Hartmann wavefront sensor (SH-WFS) which is typically an array of lenslets and associated QUAD-cell detectors. Each QUAD-cell maps to a DM actuator and corresponding mirror segment. Therefore, just considering one of the QUAD-cell actuator pairs is analogous to the QUAD-cell/tilt mirror relationship. A change in spot size causes a deviation from the optimal centroid gain that will erroneously drive a DM segment to a location other than its calibrated one. By monitoring time averaged actuator command voltages, one can estimate overall centroid gain deviations.

This method is attractive because it is a passive way to exploit available information from the higher order wavefront measurement and compensation loop. Also each sub-aperture may provide an independent estimate for the centroid gain where all measurements can be averaged to increase the fidelity of the estimate. However, this

method may become process intensive for many voltages being monitored and averaged over a short period of time. Additionally, the SH-WFS divides overall intensity amongst many QUAD-cells; therefore, each QUAD-cell may provide an unreliable estimate during low flux conditions.

### **2.8.3 Measure Slope Discrepancy**

Marcos van Dam highlights a potential drawback of the previous method employing the DM's average shape. Since the power for aberrations due to non-common paths and a telescope's primary mirror are typically low order, it may be difficult to accurately infer deviations of the centroid gain solely from the DM's average shape. In other words, the centroid gain measurement is corrupted by aberrations of the AO system's primary mirror. Therefore, Marcos van Dam developed the slope discrepancy method. Slope discrepancy refers to the difference between the measured wavefront slopes from the SH-WFS and the reconstructed slopes obtained by differentiating the wavefront reconstructor. The discrepancy originates from skewing the reference SH-WFS centroids off-center to account for AO system aberrations, where the aberrations are typically due to non-common path errors and lenslet array imperfections. Therefore, a portion of the power for the skewed centroids lie in the null space of the wavefront reconstructor, making it impossible for the reconstructor to perfectly recreate the SH-WFS slopes [17].

Since the reconstructor is "blind" to the null space, the slope discrepancy components are not corrupted by the AO system. This is the claimed advantage over Veran and Herriot's method [17]. For a calibrating source, the relationship between the reference and source slope discrepancy components serve as a reference to assess when an arbitrary

source deviates from the calibrating source. Therefore, an overall centroid gain estimate is made from slope discrepancy measurements that directly relates to SH-WFS performance. The advantages and disadvantages of this method are similar to those listed for Veran and Herriot's method. The principal concerns for van Dam's method is its applicability to asymmetrical LEO objects, processing time to measure and average many slope discrepancy components, and SH-WFS performance during low flux conditions.

#### **2.8.4 Dither Tilt Mirror (TM)**

This research employs the TM dithering method to estimate centroid gain indirectly; it induces a known artificial tilt disturbance to the QUAD-cell by commanding the tilt mirror to move with a known throw and frequency. By measuring the resultant  $\tilde{I}$ , then comparing to the known optimal,  $\hat{I}$ , the unknown centroid gain can be estimated. The general idea is that a larger or smaller spot than optimal will reflect in the  $\tilde{I}$  values. Amongst all the methods considered, the dither method is more likely to provide a robust way to rapidly determine  $K_c$  during low flux conditions because it employs a single QUAD-cell detector. The primary disadvantage of this method is the active measuring technique of dithering the TM. Marcos van Dam noted the TM dithering method was implemented successfully for the ALTAIR AO system where the dithering induced a 50 nm rms wavefront error; this was mainly attributed to dithering the TM at high frequencies where it experienced significant oscillations [17]. However, the TM method for this research is applied to the lower order AO loop where a high dither frequency is not necessary. Additionally, the dither method provides a singular estimate for centroid gain as opposed to an array of estimates made with the other methods employing the SH-WFS. Finally, the

dithering method may require a disruption in tilt measurement to allow for a calibration period when the unknown centroid gain is estimated.

### III. Optical Modeling and Methodology

#### Chapter Overview

This work requires extensive computer modeling; therefore, this chapter details the modeling process, design decisions, and applicable assumptions the author uses to realize models that accurately represent concepts introduced in Chapter II. Furthermore, this chapter develops the methodology in parallel with the modeling process, eventually leading to a thorough characterization of the pyramid track sensor to be used with the adaptive tilt tracker in Chapter IV.

#### 3.1 Model Tilt Process

This research uses AOTools<sup>®</sup>, an adaptive optics toolbox application for MATLAB<sup>®</sup>, to develop tilt processes. Recall from Section 2.2.2.1, spatial and temporal aspects define tilt processes along with telescope operating parameters. The atmospheric

	Altitude 1	Altitude 2	Slant Rng	Vel1 (m/s)	Slew(deg/s)
Propagation path (km):	0	450	450	0	1

Zenith Angle (deg):	0
Aperture Diam (m):	3.5
Wavelength (micron):	0.5
Source Range (km):	Inf

r0 (cm)	5.01
theta0 (microrad)	6.88
sigma_l^2 (Rytov)	0.0587
sig_jit (1-ax)(microrad)	2.03
f_G (Greenwood) (Hz)	370
f_TG (Tracking) (Hz)	44.2

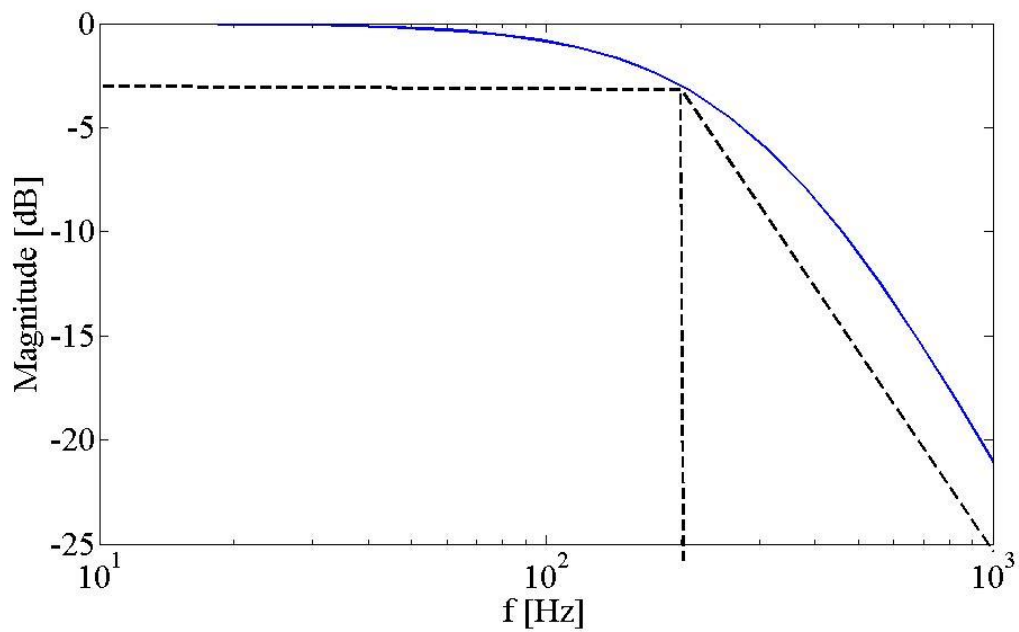
Update All

Figure 15 - AOTools<sup>®</sup> atmospheric statistics menu

propagation statistics menu in figure 15 accepts user inputs representing expected telescope operating conditions. Accordingly, this model sets up a vertical seeing and slewing telescope. The telescope has a 3.5 meter diameter aperture and operates at a 0.5 micron center-band wavelength. The H-V  $5/7 C_n^2$  profile evaluated with a 450 km propagation path and a Bufton wind model define turbulence conditions. A slew rate of one degree per second approximates tracking an LEO object having a range and velocity of 450 km and 7.8 km/s respectively.

In response to the inputted data, the program displays spatial and temporal data depicting atmospheric seeing conditions. Coherence parameters,  $r_0$  and  $\theta_0$ , of about 5.0 cm and 7.0  $\mu$ rad result as expected. Additionally, the Tyler frequency value of 44.2 Hz is eleven times higher than the value for a non-slewing telescope, which corresponds to a more dynamic tilt process.

Notice the inputted parameters to the atmospheric statistics menu can also define the tilt PSD. Therefore, this work creates and imports an atmospheric characteristics file into another AOTools<sup>®</sup> application, the atmospheric tilt PSD menu, to generate a tilt PSD. With specified minimum and maximum frequencies, a *G-tilt* PSD is calculated to have a frequency range that corresponds to the FSM's frequency response; reference figures 16 and 17.



**Figure 16 - CL FSM magnitude frequency response depicted by the solid curve with dashed lines to indicate a 3 dB bandwidth point of about 200 Hz**

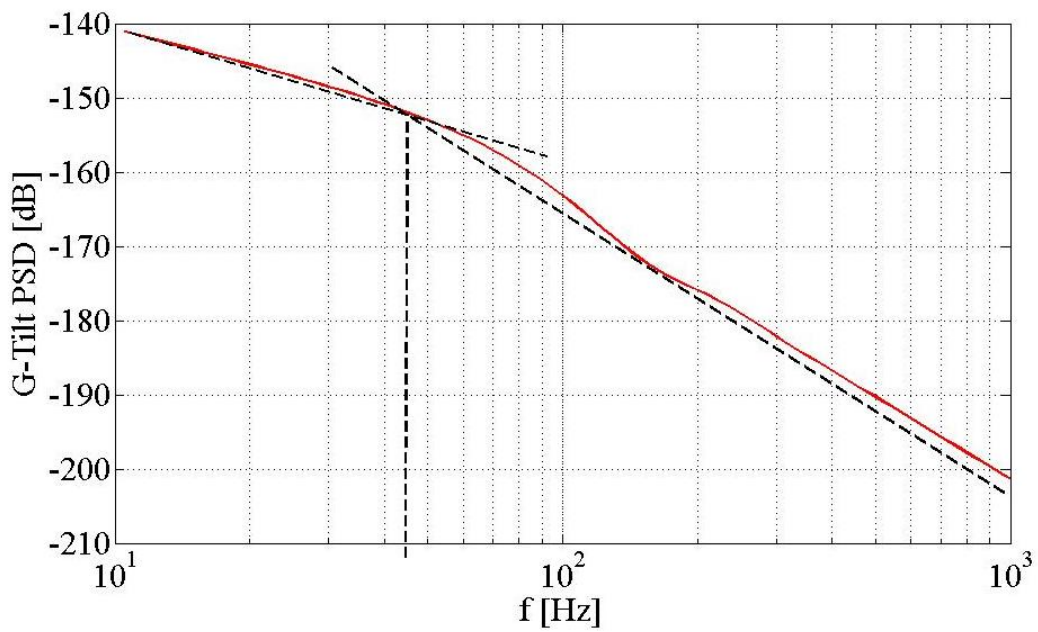


**Figure 17 - G-Tilt PSD depicted by solid curve with dashed lines to indicate a Tyler frequency of about 44 Hz**

The dashed lines of figures 16 and 17 represent asymptotic slope approximations to the frequency response curves. In figure 16, the intersection of the lines corresponds to the steering mirror's 3dB bandwidth point of about 200 Hz. Likewise, the intersection of the lines in figure 17 corresponds to the Tyler frequency of about 44 Hz, the effective bandwidth of tilt disturbance used for this work.

### 3.1.1 Tilt Filter Realization

This work uses the generated PSD in figure 17 to time correlate a normal distribution of tilts having a  $G_{tilt}$  spatial variance envelope. Reference figure 18, the 'white' or uncorrelated tilt process gets shaped by a filter having a frequency response according to the tilt PSD of figure 17.

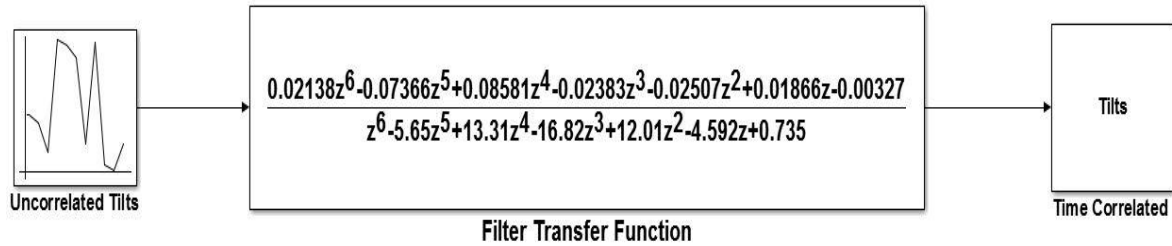


**Figure 18 - Yule-Walker filter time correlates the inputted 'white' tilt process according to G-tilt PSD**

MATLAB<sup>®</sup> function, `yulewalk.m`, generates a recursive digital filter to mimic the PSD response by least-squares fitting the PSD data. Given desired filter order for fit accuracy, PSD magnitude and frequency data, and Nyquist sampling rate, the function outputs coefficients corresponding to the numerator and denominator terms of a PSD filter transfer function, as in figure 18.



### 3.1.2 Filter Verification

This work verifies the filter's accuracy using two methods. The first method obtains the filter's frequency response, blue-dotted curve of figure 19, and compares it to the reference PSD (red-solid curve). The comparison shows the filter is accurate over most of the frequency range considered; however, there is slight disagreement of the responses at the edges of the frequency range as the filter response feathers away from the reference PSD.

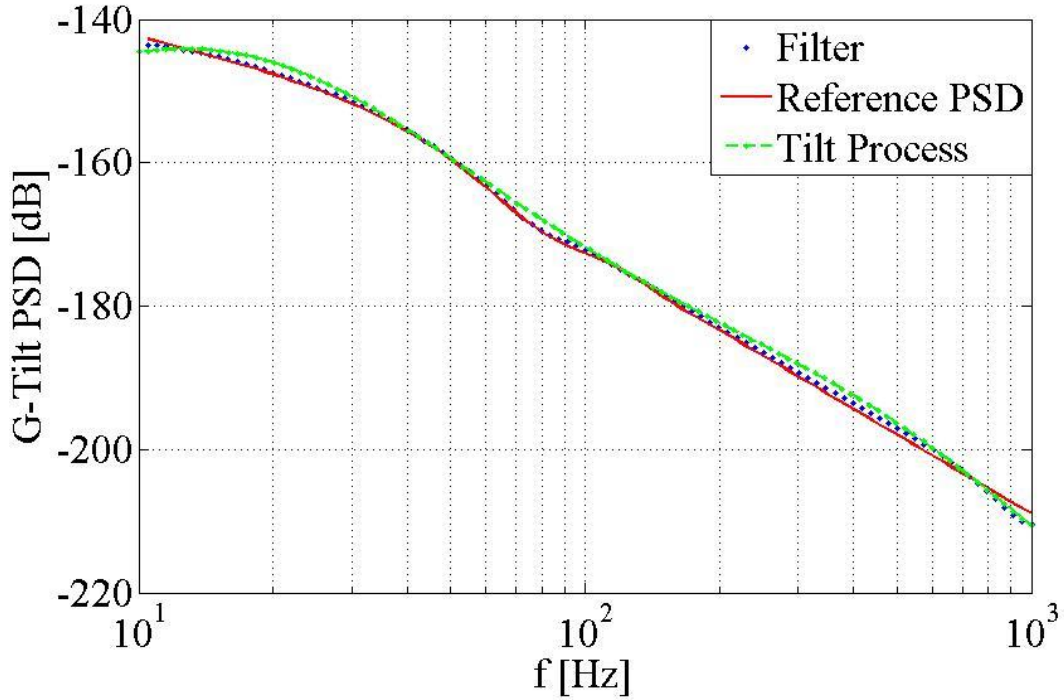


**Figure 19 - Verification of G-tilt filter frequency response**

The second method inputs a 'white' tilt process of 100,000 random tilts with a specified *G-tilt* spatial variance thru the filter, shown in figure 18, to verify the filter's accuracy by measuring the frequency response and variance of the output tilt process. This method also confirmed the filter's accuracy as the variance of the output process is within 2% of

the input process variance. Additionally, the PSD of the output process, green-dashed plot of figure 19, agrees with the reference PSD where the green plot is a polynomial fit to a noisy PSD curve and therefore deviates slightly from the reference. The next step in the modeling process is to model the optical system that is affected by tilt distortion.

### 3.2 Model Optical Setup

The SOR telescope model abstracts from the complexities of the actual system without loss to the overall goal of measuring tilt distortion. Therefore, a simple model employs an annular aperture with primary and secondary mirror diameters,  $D_p$  and  $D_s$ , respectively. This is a very fast imager with a focal ratio of 1.5; reference table 1 for telescope parameter values.

**Table 1. Telescope Parameters**

Parameter	Value (meters)
Primary Mirror Diameter: $D_p$	3.5
Secondary Mirror Diameter: $D_s$	0.75
Focal Length: $f$	5.25
Center-band operating wavelength: $\lambda$	0.5e-6

Furthermore, this simulated system assumes diffraction limited performance in the absence of tilt aberrations,  $W_{tilt}$ , with no inherent aberrations factored into the generalized pupil function,

$$\mathcal{P}(x_1, y_1, x_2, y_2) = [circ(x_1, y_1, D_o) - circ(x_2, y_2, D_i)]e^{-j2\pi W_{tilt}}, \quad (3.1)$$

where a MATLAB<sup>®</sup> function,  $circ(x_i, y_i, D)$ , instantiates a circular pupil given arguments for spatial coordinates and pupil diameter. The pupil function realizes the annular aperture by subtracting the secondary mirror's circular area with spatial coordinates,  $x_2$  and  $y_2$ , from the primary mirror's circular area having coordinates,  $x_1$  and  $y_1$ .

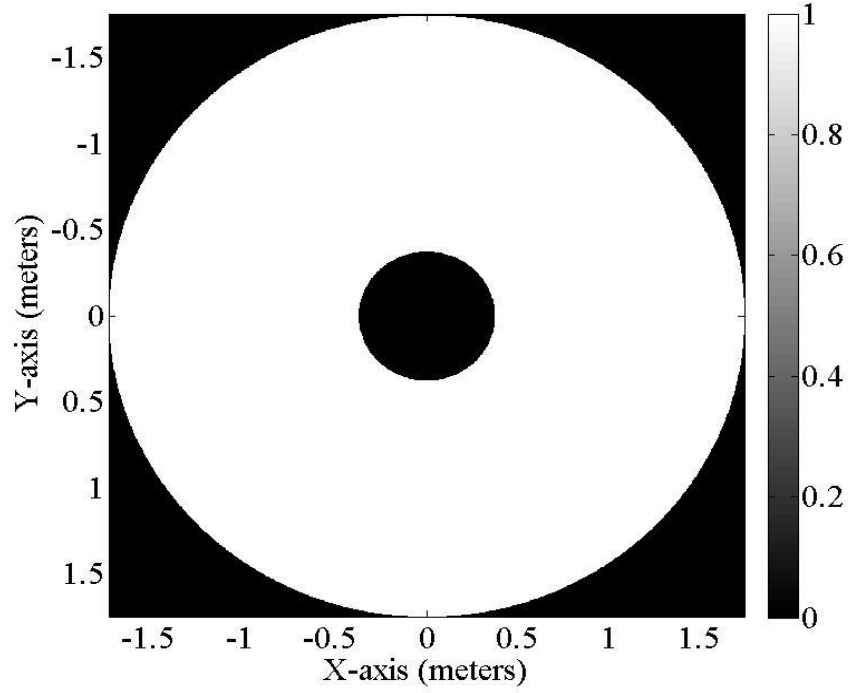


**Figure 20 - Simulated 3.5 meter annular aperture where optical signals are passed within the white region**

Notice the depicted annular aperture in figure 20 creates a binary optical effect as follows

$$\begin{cases} \mathcal{P}(x_1, y_1, x_2, y_2) = 1 & \text{for } (0.375 \leq |x, y| \leq 1.5) \\ \mathcal{P}(x_1, y_1, x_2, y_2) = 0 & \text{for } (|x, y| \text{ otherwise}) \end{cases}, \quad (3.2)$$

where the pupil unity passes optical signals within the white region and blocks optical signals elsewhere. The optical model utilizes the point spread function (PSF), which generalizes the optical impulse response,  $h(u, v)$ , to accomplish incoherent imaging as follows [11],

$$|h(u, v)|^2 = \left| \frac{1}{\lambda z_i} \mathcal{F}\{\mathcal{P}(x, y)\} \right|^2, \quad (3.3)$$

where the square of the ASF's magnitude is taken to only account for object intensity. As previously stated, the convolution operation models imaging as follows [11],

$$I_i(u, v) = |h(u, v)|^2 \otimes I_o(u, v), \quad (3.4)$$

where  $I_o(u, v)$  is object intensity and  $I_i(u, v)$  is image intensity. The telescope imager presents the result of equation 3.4 to different legs of an optical train to facilitate various measurement and compensation functions. This work models two particular legs involving the focal plane array and the pyramid track sensor.

### 3.2.1 Pyramid Track Sensor (PTS)

The PTS is a type of tilt sensor that employs an optical pyramid and a detector array; reference figure 21. An incident light beam having no tilt disturbance gets divided equally into four intensity spots when focused to the pyramid's apex.

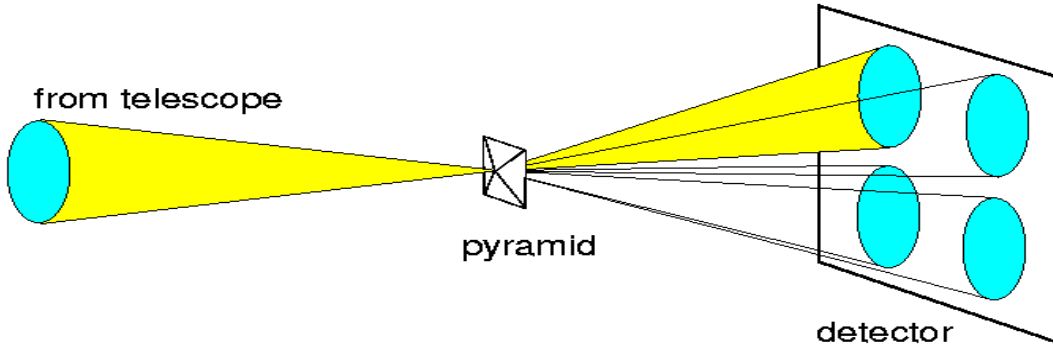


**Figure 21 - Optical pyramid creating four intensity spots to be measured by the detector [19]**

A tilt disturbance registers as an intensity imbalance when the pyramidal faces bias the tilted beam in favor of one or more of the intensity spots in relation to the others. The detector array samples the intensity spots to report the presence of tilt disturbance. Generally, the detector array size is variable; however, this work considers the case when the detector array is a QUAD-cell. Consider figure 22 where the QUAD-cell shows a partitioned intensity distribution to indicate a tilt disturbance.

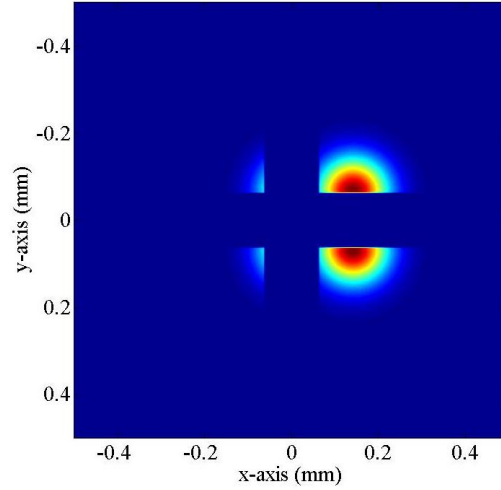


**Figure 22 - PTS QUAD-cell detecting tilt disturbance by measuring cell intensity imbalances**

Figure 22 shows a clearly resolved image being partitioned amongst the QUAD-cell. As discussed in Chapter II, a QUAD-cell cannot resolve an image; it can only indicate cell intensity values. However, the author uses resolved images hereafter to illustrate concepts involving LEO object characteristics and image modulation effects.

This work determines the required QUAD-cell size by imaging a LEO object having a vertical distance of 250 km from the telescope and maximum planar dimensions of 24 m x 24 m; this translates to an image having planar dimensions of about  $500\ \mu\text{m}$  x  $500\ \mu\text{m}$  at the detector. Therefore, this work sets the effective QUAD-cell dimensions to 1 mm x 1 mm where the image has ample dynamic range to move when under the influence of tilt disturbance. The PTS receives the image intensity via a collimated beam and 50 mm entrance pupil; thereafter, the intensity is focused to the pyramid's apex. Setting the PTS's distance with respect to the entrance pupil and choosing the optical properties for the pyramidal faces determine how much image intensity displacement happens at the QUAD-cell for a given tilt disturbance. This work abstracts from the optical setup for the PTS to

only specify that a maximum expected open loop (OL) tilt phase disturbance of  $\pm 67$  radians translates to an absolute intensity displacement of about  $67 \mu\text{m}$  at the QUAD-cell or 67 pixels for a 1 mm x 1 mm pixel array. Similarly, a maximum expected closed loop (CL) tilt phase disturbance of  $\pm 2$  radians corresponds to an absolute intensity displacement of about  $2 \mu\text{m}$  at the QUAD-cell or two pixels for the 1 mm x 1 mm pixel array. Additionally, this work models the QUAD-cell as a Geiger mode avalanche photo-diode (APD) array. Geiger mode refers to biasing the diode arrays to count individual photons. The diode arrays have a readout time of  $20 \mu\text{sec}$  and no read noise. However, APD performance is limited by dark current noise and detector-to-detector crosstalk [20]; this work does not consider crosstalk effects. Reference table 2 for QUAD-cell specifications.

**Table 2. QAUD-cell Specifications**

Specification	Value
Quantum efficiency ( $Qe$ ) @ ( $\lambda_c = 0.5 \mu\text{m}$ )	0.50
Photo-detector size (square side)	$500 \mu\text{m}$
Read noise per pixel ( $n_e$ ) @ ( $\lambda_c = 0.5 \mu\text{m}$ )	$0.0 e^-$
Dark current per pixel ( $n_d$ ) @ ( $\lambda_c = 0.5 \mu\text{m}$ )	$4.0 e^-$
Maximum frame rate	10 kfps
Readout latency	$20 \mu\text{sec}$
Sensor FOV	$26 \mu\text{rad}$
Spectral Bandwidth ( $BW$ )	$(0.4 \text{ to } 0.7) \mu\text{m}$
Number of photo-detectors ( $N_p$ )	4

The pyramid can have reflective or refractive optical properties. This research models a mirror prism that has a singular purpose to create and vary four cell intensities as tilt varies across the prism's apex. Four transfer mask functions represent the prism faces that introduce phase delays to the incident beam as follows,

$$\begin{aligned} T_1 &= H_1(u, v)e^{-j2\pi W_1} \\ T_2 &= H_2(u, v)e^{-j2\pi W_2} \end{aligned} \tag{3.5}$$

$$\begin{aligned} T_3 &= H_3(u, v)e^{-j2\pi W_3} \\ T_4 &= H_4(u, v)e^{-j2\pi W_4}, \end{aligned}$$

where a switch term,  $H_i(u, v)$ , and a tilt distortion term,  $W_i$ , define each transfer mask function. The switch term has a binary effect that simply activates a particular phase delay over a specified quadrant of space as follows,

$$\begin{cases} H_1(u, v) = 1 \text{ for } (-u, -v) \mid H_1(u, v) = 0 \text{ otherwise} \\ H_2(u, v) = 1 \text{ for } (+u, -v) \mid H_2(u, v) = 0 \text{ otherwise} \\ H_3(u, v) = 1 \text{ for } (+u, +v) \mid H_3(u, v) = 0 \text{ otherwise} \\ H_4(u, v) = 1 \text{ for } (-u, +v) \mid H_4(u, v) = 0 \text{ otherwise} \end{cases} \tag{3.6}$$

The prism faces shift the intensity distribution away from the optical axis in an analogous manner to tilt distortion; therefore, this model employs Zernike tilt polynomials to realize prism face phase effects as follows,

$$\begin{aligned} e^{-j\phi_i} &= e^{-j2\pi W_i} \\ W_i &= \alpha_2 Z_2(r, \theta) + \alpha_3 Z_3(r, \theta), \end{aligned} \tag{3.7}$$

where  $\phi_i$  is the phase induced by a prism face. The tilt distortion term,  $W_i$ , is a linear combination of orthogonal Zernike polynomials for *x-tilt*,  $Z_2$ , and *y-tilt*,  $Z_3$ , with respective

weights  $\alpha_2$  and  $\alpha_3$ . The weights give the model flexibility in tuning the amount of desired prism face phase effects.

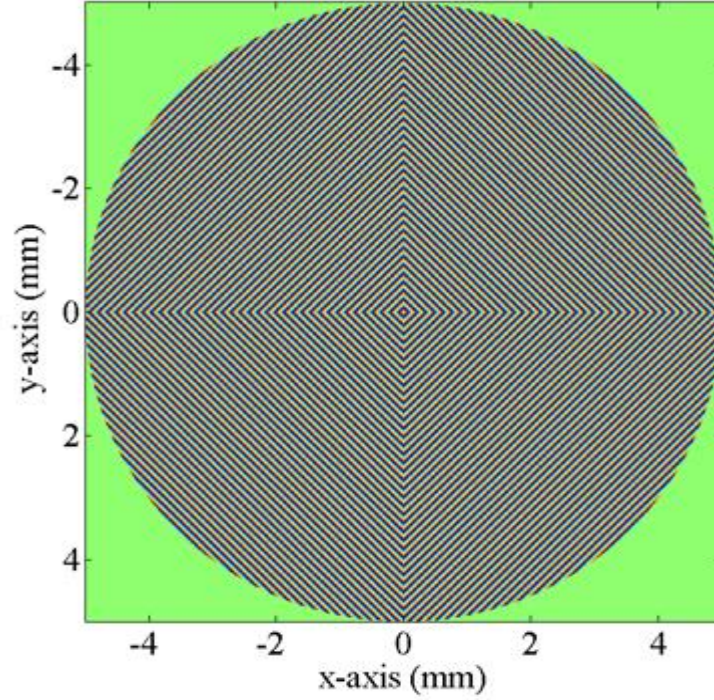


**Figure 23 - Phase mask to simulate PTS pyramidal face effects**

Consider figure 23 where a MATLAB<sup>®</sup> script models the apex as another pupil to receive the tilted input beam from the telescope's pupil. The apex pupil is divided into four regions as defined by the four transfer masks.

### **3.2.2 Focal Plane Array (FPA)**

As previously discussed, the QUAD-cell cannot determine spot size; therefore, this work simulates a FPA to measure spot size. Although the FPA is not employed in the implemented tracker system; the FPA enables characterizing the PTS sensor performance



as spot size varies. Therefore, the second leg of the optical train involves the FPA having the specifications listed in table 3.

**Table 3. Focal Plane Array Specifications [20]**

Specification	Value
Quantum efficiency (Qe)	0.85
Pixel size (square side)	21 $\mu\text{m}$
Read noise per pixel ( $n_e$ ) @ ( $\lambda_c = 0.5 \mu\text{m}$ )	4.0 $e^-$
Dark current per pixel ( $n_d$ ) @ ( $\lambda_c = 0.5 \mu\text{m}$ )	2.0 $e^-$
read out latency	100 $\mu\text{sec}$
pixel FOV	103.9 nrad
Spectral Bandwidth (BW)	(0.4 to 0.7) $\mu\text{m}$
Number of pixels ( $N_p$ )	1024 x 1024

### 3.3 Model LEO Objects

This work models both intercontinental ballistic missile (ICBM) and satellite LEO objects as presented in figure 24. A MATLAB<sup>®</sup> script translates portable network graphics (PNG) files for each object to arrays of values ranging about (0 to 255). The values are normalized where unity corresponds to the maximum object intensity as indicated by the red colored pixels of figure 24.

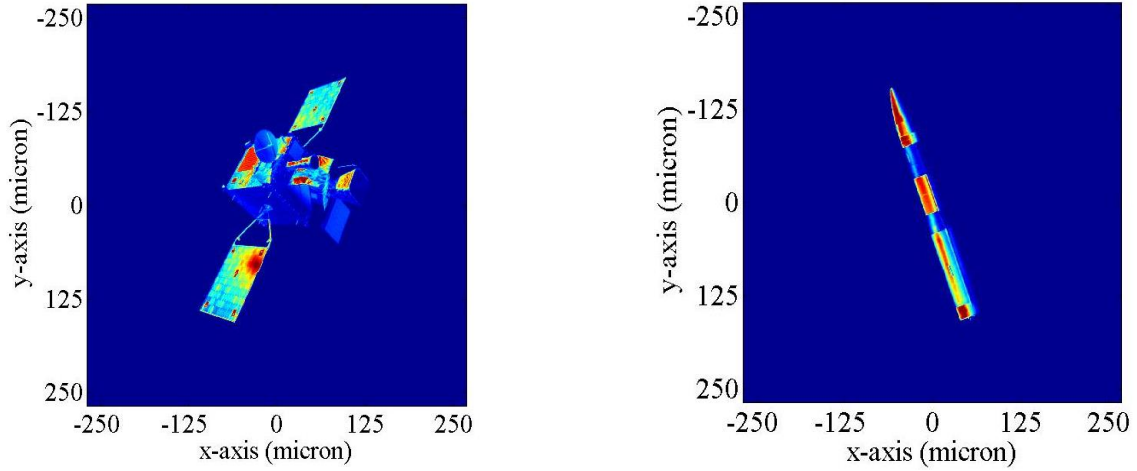


**Figure 24 - Simulated Satellite and ICBM LEO objects**

The modeled ICBM and satellite are ideal for this work because they enable a rigorous PTS characterization when measuring tilt distortion of a LEO object. Each modelled object has an asymmetrical shape to generate different PTS responses,  $Kg_x$  and  $Kg_y$ , for  $x$  and  $y$  extents. Additionally, both objects have asymmetrical intensity distributions that deviate substantially from the ideal Gaussian distribution. As expected, these non-ideal object characteristics adversely affect PTS measurement performance. Recall that most LEO objects are comparatively dim; therefore, it is vital to determine photon flux levels based on expected astronomical brightness magnitudes.

### 3.4 Model Signal Flux

The photon flux,  $\varphi_p$ , from an object is determined from its astronomical brightness magnitude. This model only considers magnitudes of the visual band, ( $V-mag$ ), and does not consider changes of  $V-mag$  due to a telescope's zenith angle beyond zero degrees. The flux unit or jansky (Jy) is a non-SI unit of spectral flux density and it relates to an arbitrary  $V-mag$  as follows [5],

$$1J_y = 10^{-26} \frac{W}{\text{m}^2\text{Hz}}$$

$$J_y^0(V=0) = 3640 J_y \quad (3.8)$$

$$J_y(V) = J_y^0 10^{(-0.4V-26)} \frac{W}{\text{m}^2\text{Hz}},$$

where the signal power,  $W$ , is measured with respect to a certain bandwidth, Hz, over a specified area. Additionally, the zero value for  $V$  serves as a baseline to relate  $J_y$  to  $V$ -mags. For a circular aperture with diameter,  $D$ , the photon flux is as follows,

$$\varphi_p(V) = \left[ J_y(V) \pi \frac{D^2}{4} \frac{c}{\lambda_c} \right] (h\nu)^{-1}, \quad (3.9)$$

where  $c$  is the velocity of light in vacuum;  $\lambda_c$  is the center-band wavelength;  $h$  is Planck's constant having units Joule seconds (J·s), where it corresponds to a photon's energy; and  $\nu$  is the photon's frequency. This work now uses the obtained result for  $\varphi_p(V)$  to characterize sampling rates for the PTS.

### 3.5 PTS Frame Rate Characterization

This research identifies minimum and maximum bounds for PTS frame rate; the bounds reflect the need to maintain a suitable  $SNR_v$  value while minimizing control loop delays due to PTS operation.  $SNR_v$  and frame rate,  $f_s$ , are competing factors as one must be compromised to sustain the other for waning signal levels.

#### 3.5.1 Determine Threshold $SNR_v$ Value

Consider again the  $SNR_v$  expression for the PTS where its signal level is limited by shot noise,  $\sqrt{N_s}$ , and dark current noise,  $\sqrt{4(n_D)}$ ,

$$SNR_v = \frac{N_s}{\sqrt{N_s + 4(n_D)}} \quad (3.10)$$

However, Chapter II showed that for higher signal levels, the PTS's signal level is limited predominately by shot noise and can be approximated as

$$SNR_v \approx \sqrt{N_s} \quad (3.11)$$

Recall the  $SNR_v$  numerator term represents the number of photo-electrons counted over a sampling period,

$$N_s = \chi \varphi_p f_s^{-1} Q_e \quad (3.12)$$

$$0 < \chi < 1,$$

where the  $\chi$  term reflects that a fraction of the incident photons collected by the 3.5 meter aperture are applied to the PTS optical leg. After considering optical losses and the division of photons amongst the different optical legs, this work sets  $\chi$  to a conservative value of 0.30.

**Table 4. PTS Frame Rate Characterization [ $Q_e = 0.50$ ;  $\chi = 0.30$ ;  $N_p = 4$ ]**

$V(+)$	$f$ [kfps]	$N_s$ [ $e^-$ ]	$SNR_v$
7	10.0	12558	112*
8	10.0	4999	71*
9	10.0	1990	45*
10	10.0	792	28*
11	10.0	315	17
12	10.0	126	11
13	10.0	50	6
14	10.0	20	3
15	10.0//5.0	8//16	--//3
16	5.0//1.0	6//32	--//5
17	1.0//0.2	13//63	2//7
18	0.2	25	4

\* (Shot limited)

Reference table 4 where  $f_{max}$  is set to 10 kfps. The chosen  $f_{max}$  originates from a technical specification for a 24 x 24 sub-aperture wavefront sensor that employs APD QUAD-cells for each sub-aperture [20]. Therefore,  $f_{max}$  is realistic for a single APD QUAD-cell to measure tilt distortion. The table columns correspond to  $V-mag$ , frame rate, QUAD-cell photo-electrons, and  $SNR_v$  where the tradeoff between frame rate and  $SNR_v$  becomes evident. The PTS operates at  $f_{max}$  up to a  $V-mag$  of 14; thereafter,  $SNR_v$  descends below a value of two (indicated by the double dashes). In order to restore  $SNR_v$  to two or better for  $V-mags$  dimmer than 14, the frame rate is reduced from 10 kfps to an eventual 0.2 kfps in table 4.

A design decision is made to identify a  $SNR_v$  threshold,  $SNR_{v,0}$ , such that when the tracker operates below  $SNR_{v,0}$ , tracker performance is less than desired. Recall the expression for residual tracker error due to temporal and measurement constraints,

$$\sigma_{tracker}(SNR_v) = \left\{ \left( f_{TG} / f_{3dB} \right)^2 + \left( 3\pi/16 SNR_v^{-1} \right)^2 \right\}^{\frac{1}{2}} (\lambda/D), \quad (3.13)$$

where it becomes only a function of  $SNR_v$  for a constant Tyler frequency, tracker bandwidth, and diffraction angle. The dependence on image spot size is suppressed from equation 3.13 because centroid gain deviations of the PTS, which are modeled separately, already account for measurement error due to spot size. Setting  $f_{TG}$  and  $f_{3dB}$  of equation 3.13 to their respective values of 44 Hz and 200 Hz, then normalizing the tracker error by  $\lambda/D$ , equation 3.13 becomes,

$$\frac{\sigma_{tracker}(SNR_v)}{\lambda/D} = \left\{ (44/200)^2 + \left( 3\pi/16 SNR_v^{-1} \right)^2 \right\}^{1/2}, \quad (3.14)$$

where this error expression is plotted versus increasing values for  $SNR_v$  in figure 25.

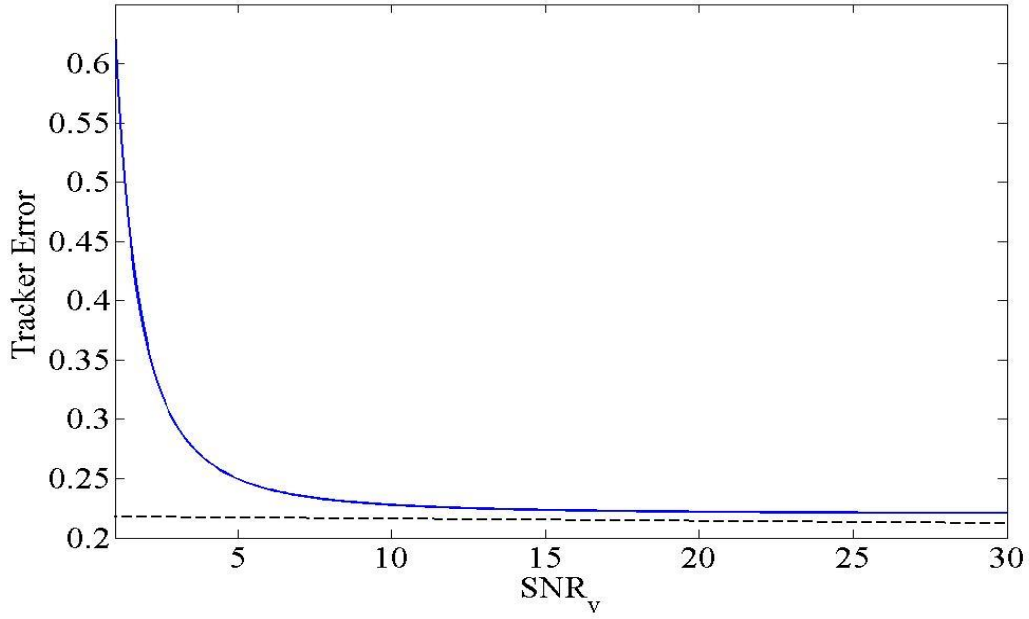


**Figure 25 - Normalized tracker error where the dashed line shows the minimum tracker error being limited by temporal tracker error**

The normalized tracker error is a fraction of the optical system's diffraction angle and figure 25 shows that it quickly approaches a minimum for increasing  $SNR_v$  values as follows,

$$\frac{\sigma_{tracker}(SNR_v)}{\lambda/D} = 44/200 = 0.22 \quad \text{for } SNR_v \gg 1, \quad (3.15)$$

where the minimum normalized tracker error of 0.22, shown by the dashed line of figure 25, is the limited performance of the tracker due to temporal constraints (tracker bandwidth). Having a tracker bandwidth much larger than the recommended  $4f_{T_G}$  offers negligible tilt compensation while coupling high frequency disturbances into the tracker.

Recall from Chapter II that  $f_{3dB}$  is generally set such that the temporal tracker error is at most 25% of the diffraction angle. From figure 25, a  $SNR_v$  value of five or higher

corresponds to a tracker error at or below  $0.25 \left( \lambda/D \right)$  as desired. Therefore, this work sets  $SNR_{v_0}$  to five.

### 3.5.2 Determine Threshold Frame Rate

For waning signal levels, decreasing  $f_s$  to sustain a  $SNR_v$  value of at least five may compromise tilt tracker performance. As stated in Chapter II, maximizing detector frame rate has the advantage of minimizing tracker system loop delay due to detector operation. Unchecked loop delay erodes gain and phase stability margins, eventually making an otherwise robust system more susceptible to disturbances and/or driving a stable system to instability. Consider figure 26 where the tilt tracker system is shown as a simplified sampled-data system in the  $s$ -domain, ( $s = j\omega$ ).

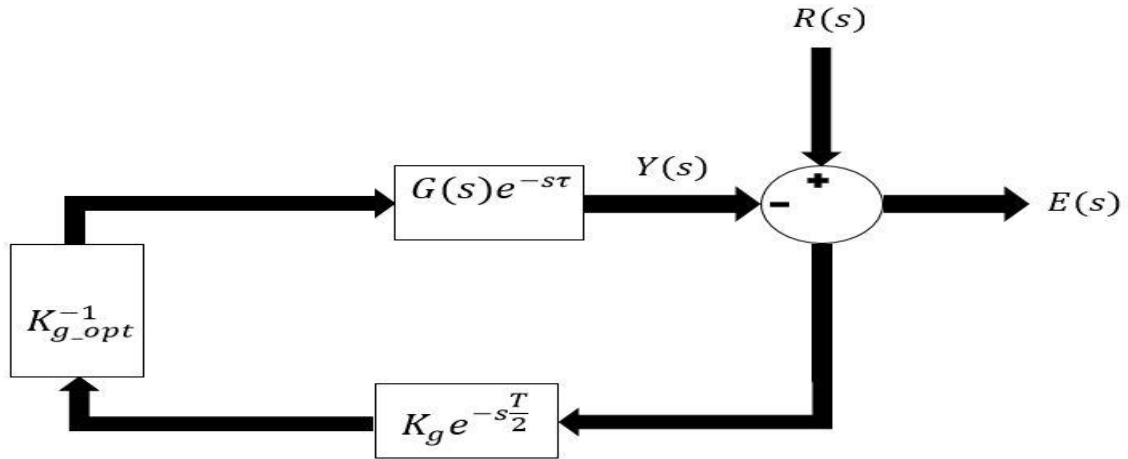


**Figure 26 - Tilt tracker system represented as a sampled-data system in the  $s$ -domain to show phase delay effects due to detector operation**

The detector,  $K_g e^{-sT/2}$ , samples the tracker error,  $E(s)$ , every  $T$  seconds and provides discrete feedback to the system;  $\exp(-sT/2)$  is the delay term due to sampling alone [21].

$K_g$  is the random detector response where it is referenced about the optimal response using the  $K_{g\_opt}^{-1}$  term as follows,

$$\frac{K_g}{K_{g\_opt}} = \alpha \quad (3.16)$$

A unity value for  $\alpha$  corresponds to optimal detector response. Compensator and plant dynamics are incorporated into the  $G(s)e^{-s\tau}$  term where delay time,  $\tau$ , is due to detector readout, zero-order holds, and other processing functions; therefore, the total delay accounted to the detector is

$$\bar{\tau} = \tau + \frac{T}{2} \quad (3.17)$$

For the tilt tracker system shown in figure 26, the open-loop transfer function is accurately approximated by second order dynamics having a natural frequency of  $\omega_n$ ,

$$G_{OL}(j\omega) \cong \frac{\alpha\omega_n^2}{j\omega(j\omega+2\zeta\omega_n)} e^{-j\omega\bar{\tau}} \quad (3.18)$$

To investigate the effect of a delay on phase margin,  $PM$ , first find the gain crossover frequency,  $\omega_{gc}$ , where the magnitude of  $G_{OL}(j\omega)$  is unity [21],

$$|G_{OL}(j\omega_{gc})| = \frac{\alpha\omega_n^2}{\sqrt{\omega_{gc}^4 + (2\zeta\omega_n)^2\omega_{gc}^2}} = 1 \quad (3.19)$$

For a critically damped system where  $\zeta$  is unity, equation (3.19) yields an expression for  $\omega_{gc}$  in terms of  $\omega_n$  and  $\alpha$ ,

$$\omega_{gc} = \omega_n(-2 + \sqrt{4 + \alpha^2})^{1/2} \quad (3.20)$$

After obtaining an expression for the phase of  $G_{OL}(j\omega)$ , the definition for  $PM$  is applied,

$$\phi(\omega) = -\omega\bar{\tau} - \tan^{-1}\left(\frac{\omega}{2\omega_n}\right) - \frac{\pi}{2} \quad (3.21)$$

$$PM = \phi(\omega_{gc}) + \pi \xrightarrow{yields} -\phi(\bar{\tau}, \alpha) - \phi(\alpha) + \frac{\pi}{2}, \quad (3.22)$$



where

$$\begin{aligned}\phi(\bar{\tau}, \alpha) &= \omega_n(-2 + \sqrt{4 + \alpha^2})^{1/2} \bar{\tau} \\ \phi(\alpha) &= \tan^{-1} \left\{ \frac{1}{2} (-2 + \sqrt{4 + \alpha^2})^{1/2} \right\}.\end{aligned}\quad (3.23)$$

Since  $PM$  must be positive for a stable closed loop system to exist, the phase contributions due to delay and detector response must be less than  $90^\circ$  in equation (3.22). The first term of equation (3.22) does not exist for zero delay; the second term typically contributes and has an absolute value of  $13.7^\circ$  when  $\alpha$  is unity.

Similarly, to show the effect of delay on the gain margin,  $GM$ , first determine the phase crossover frequency,  $\omega_{pc}$ , where the phase for  $G_{OL}(j\omega)$  is equal to  $-\pi$  [21].

$$\text{Im}\{G_{OL}(j\omega_{pc})\} = 0 \quad (3.24)$$

Since the imaginary part of  $G_{OL}(j\omega)$  is equal to zero at  $\omega_{pc}$ , the resulting expression yields

$$\tan(\omega_{pc} \bar{\tau}) = \frac{2\omega_n}{\omega_{pc}} \quad (3.25)$$

Typically  $\omega_{pc} \bar{\tau}$  is less than unity because the delay time is much less than the phase crossover frequency; therefore,

$$\omega_{pc} \bar{\tau} < 1 \xrightarrow{\text{yields}} \tan(\omega_{pc} \bar{\tau}) \approx \omega_{pc} \bar{\tau} + \frac{(\omega_{pc} \bar{\tau})^3}{3} \quad (3.26)$$

$$\omega_{pc} \approx \sqrt{\frac{2\omega_n}{\bar{\tau}}} \quad \text{for } \omega_n \bar{\tau} < 3/8$$

Applying the definition for  $GM$  allows for the following expression that is a function of  $\bar{\tau}$  and  $\alpha$ ,

$$GM = \frac{1}{|G_{OL}(j\omega_{pc})|} \approx \frac{2}{\alpha \omega_n \bar{\tau}} \sqrt{1 + \frac{\omega_n \bar{\tau}}{2}} \quad (3.27)$$

$$\frac{\omega_n \bar{\tau}}{2} \ll 1 \xrightarrow{\text{yields}} \sqrt{1 + \frac{\omega_n \bar{\tau}}{2}} \approx 1 + \frac{\omega_n \bar{\tau}}{4} \quad (3.28)$$

$$GM \approx \frac{1}{\alpha} \left( \frac{2}{\omega_n \bar{\tau}} + 0.5 \right) \quad (3.29)$$

From equation (3.29), notice the  $GM$  is infinite for zero delay as expected for a second order system. However, the  $GM$  ebbs with increases in delay and any increase in  $K_g$  above the optimal value compounds the effect.

The derived expressions for  $PM$  and  $GM$  allow one to make a design decision that specifies the maximum desired effect where the PTS's operation alters the stability margins. This section only considers the effect due to a delay; therefore,  $\alpha$  is set to unity for optimal sensor response. For optimal sensor response the  $PM$  is  $76.3^\circ$  and the  $GM$  is infinite for zero delay.  $PM$  is more of a limiting condition than  $GM$ ; therefore, the delay effect on  $PM$  is addressed first. The author makes a design decision to not allow the  $PM$  to dip below  $60^\circ$ ; this means that the phase loss due to detector operation should not exceed  $16.3^\circ$ .

$$\frac{16.3^\circ}{180^\circ} \pi = 1.96e3 \left( -2 + \sqrt{4 + 1^2} \right)^{1/2} \bar{\tau} \quad (3.30)$$

With  $\omega_n$  equal to  $1.96e3$  rad/sec, equation (3.30) is used to determine the maximum allowable  $\bar{\tau}$  of  $298.75 \mu s$ .

$$T = 2(\bar{\tau} - \tau) = 2(298.75 - \tau) \mu s \quad (3.31)$$

Recalling that equation (3.17) expresses  $\bar{\tau}$  in terms of detector sampling,  $T$ , and loop delay,  $\tau$ , allows for equation (3.31), where the maximum loop delay must be less than  $298.75 \mu s$ .

**Table 5. Minimum allowable frame rate versus loop delay**

$f_o(\text{fps})$	$\tau(\mu\text{s})$
1794	20
2010	50
2516	100
3361	150
5063	200
10256	250

Table 5 shows the minimum allowable frame rate as a function of loop delay. If the detector operates below specified minimums, then the  $PM$  will be less than  $60^\circ$ . Notice for a  $\tau$  of  $250 \mu\text{s}$ ,  $f_o$  is 10.256 kfps; this is unreasonable for the modeled PTS that has an  $f_{max}$  of 10 kfps. Therefore, this work sets  $\tau$  to  $100 \mu\text{s}$  for a threshold frame rate,  $f_o$ , of 2.520 kfps (rounded to the nearest tens digit). The corresponding  $PM$  and  $GM$  are about  $60^\circ$  and 11.9 dB respectively.

### 3.6 PTS Centroid Gain Characterization

The previous section discussed detector frame rate and how it relates to PTS measurement performance and control loop dynamics. Recall the tracker error dependence on spot size was suppressed from the analysis conducted in Section 3.5.1. This section investigates PTS measurement performance in regards to image spot characteristics.

### 3.6.1 Centroid Gain and Spot Spread Relationship

This work empirically characterizes the centroid gain's relationship to spot spread that enables a mathematical expression describing the relationship. The spot spread,

$$\sigma_s = \frac{W(z)}{L_D} \times 100, \quad (3.32)$$

is a percentage that relates image spot size to detector size, where  $L_D$  is the side dimension of the QUAD-cell detector. A MATLAB<sup>®</sup> script calculates the spot spread for an arbitrary intensity distribution, using the simulated FPA to measure spot size measurement at full width at half maximum (FWHM).

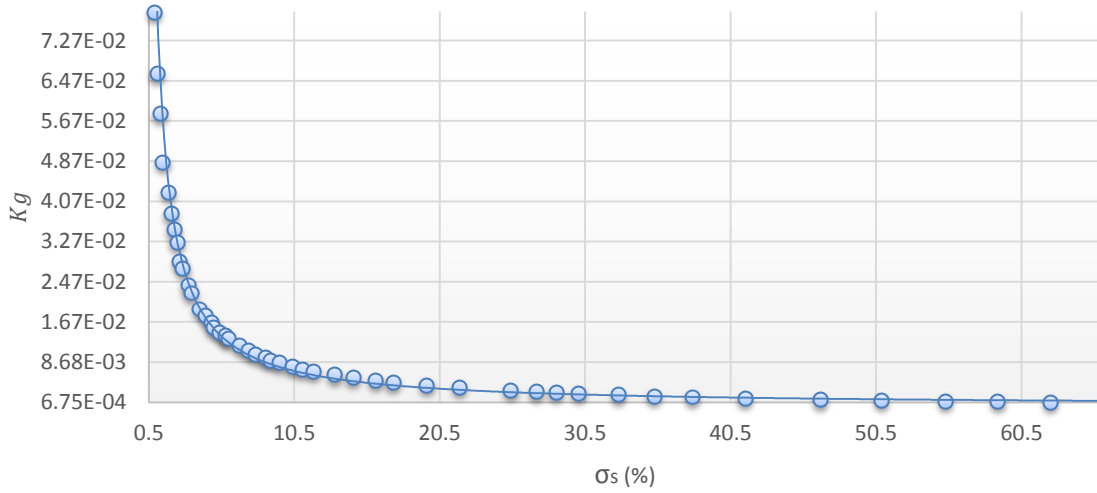


**Figure 27 - Normalized  $K_g$  plotted versus spot spread to show inverse relationship**

A PTS's response to a known set of tilt stimuli characterizes that sensor. Accordingly, a MATLAB<sup>®</sup> routine tilts a simulated Gaussian laser source over a range of 28 tilt phase stimuli to determine  $K_g$ . Figure 27 presents the results for  $K_g$  versus 47 different spot spreads ranging about 0.9% to 66%. A best fit curve of the data gives the following expression,

$$K_g(\sigma_s) = 0.0855\sigma_s^{-1.07}, \quad (3.33)$$

where the result closely agrees with the theoretical expression, equation (2.34). A slight difference amongst the exponents is due to an imperfect curve fit. The  $R^2$  coefficient, a measure of fit integrity, equals 0.9895 where a unity value is considered a perfect fit. The constant coefficient depends on detector characteristics and the tilt phase stimuli. Additionally,  $K_g$  in equation (3.33) is dimensionless because spot size is normalized with respect to the detector's dimensions.

Figure 27 reinforces the need to monitor spot spread from an arbitrary LEO object.  $K_g$  varies three orders of magnitude over the range of spot spreads where the steep portion of the curve corresponds to hyper-sensitivity and the tail end of the curve corresponds to torpid sensitivity. The next section identifies a range of spot sizes to yield optimal sensor response.

### **3.6.2 Tilt Phase Measurement**

This methodology uses a simulated Gaussian laser source to serve as a baseline to assess the PTS's performance when measuring tilt distortion of LEO objects. The goal is to identify a range of Gaussian spot spreads and corresponding centroid gains that most accurately track tilt distortion over a given dynamic range of tilt phase. Note; the tilt phase processes shown throughout section 3.6 appear jagged because they are down-sampled from their originating processes. Down-sampling reduced processing times for process intensive simulations without compromising simulation results.

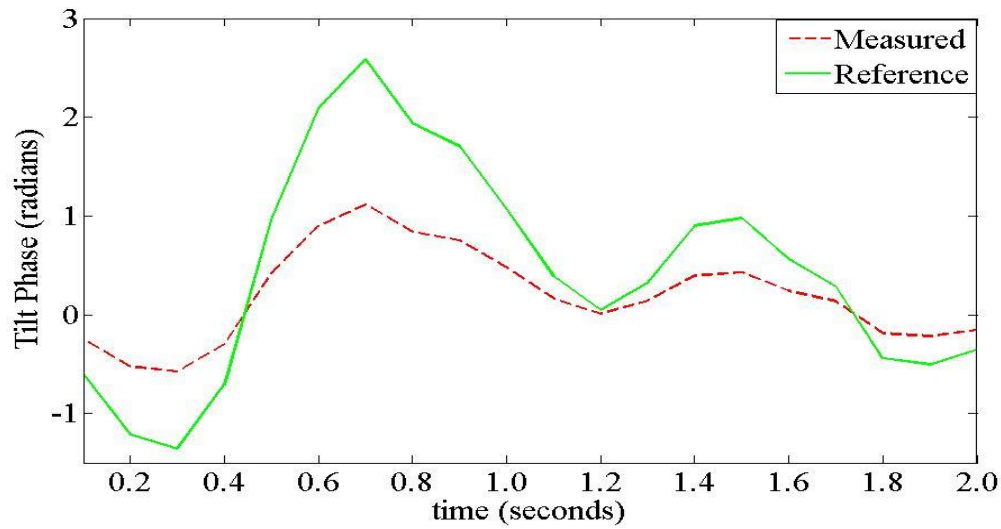


**Figure 28 - Torpid sensor response using a spot spread of 40.5%**

Consider figure 28 that corresponds to a large spot spread and a small tilt phase envelope. For large spot spreads, notice the PTS becomes insensitive to small tilt distortions as it reports a tilt phase well below the reference signal. Increasing the spot spread and/or decreasing the reference phase envelope further, drives the measured signal to zero. Conversely, a small spot spread deflects with even the slightest tilt disturbance. Reference figure 29; the PTS saturates to a non-zero boundary when values of the large phase envelope drive and confine the small spot spread's movement to only one quarter or one half of the QUAD-cell's region. This is an important result that shows the PTS is inaccurate if the intensity distribution does not lie in all four cells during tilt measurement.

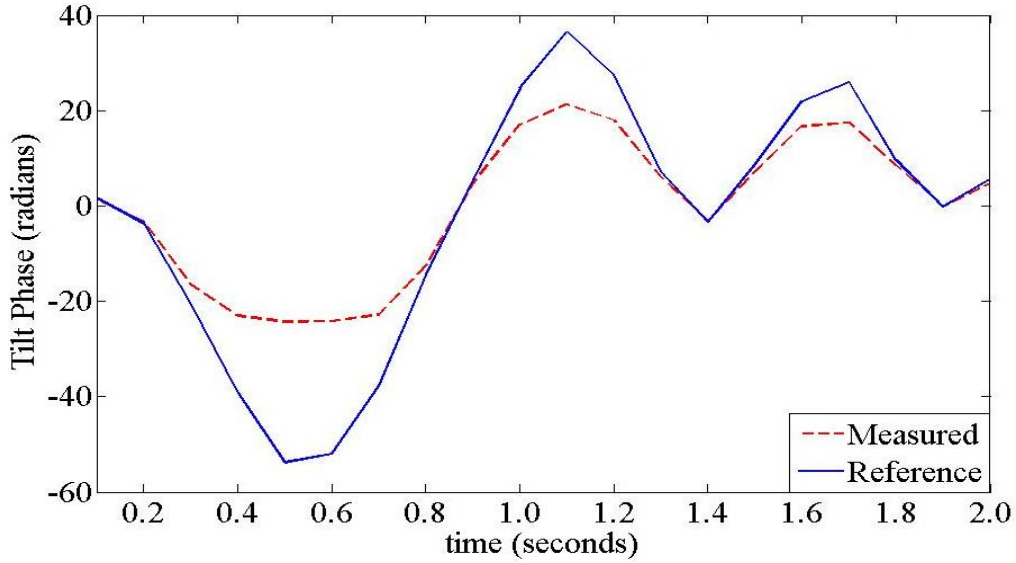


**Figure 29 - Hyper-sensitive PTS response using a spot spread of 6.0%**

The preceding results motivate the need to define an expected tilt phase envelope for the optical system under consideration. The dynamic phase range over the telescope's aperture is set to  $3\sigma_{G\_tilt}$  or  $\pm 67$  radians as to account for approximately 99% of all phase deviations. However, as the PTS operates in CL, the tracker's performance determines the phase deviation envelope. Recall the tracker's optimal performance is approximated by  $\sigma_{tracker}$  where  $3\sigma_{tracker}$  corresponds to a phase envelope of about  $\pm 2$  radians. Both phase envelopes are applicable; when the tilt tracker first initializes, it is likely to experience tilt phases from the  $3\sigma_{G\_tilt}$  envelope; however, as the tilt tracker tunes down to the residual tilt phase errors in CL operation, the  $3\sigma_{tracker}$  becomes most relevant. Therefore, this work identifies a range of Gaussian spot spreads that enable optimal PTS performance for both tilt phase envelopes.

### 3.6.2.1 Tilt Measurement Using Gaussian Source

To identify a range of Gaussian spot spreads that enable optimal PTS performance for both tilt phase envelopes, this work systematically measures simulated  $x$  and  $y$  tilt phase processes corresponding to CL and OL envelopes. The measurement involves recording the root mean square error (RSME) corresponding to 32 different spot spreads ranging from 2.4% to 80%; reference figures 30 and 31.

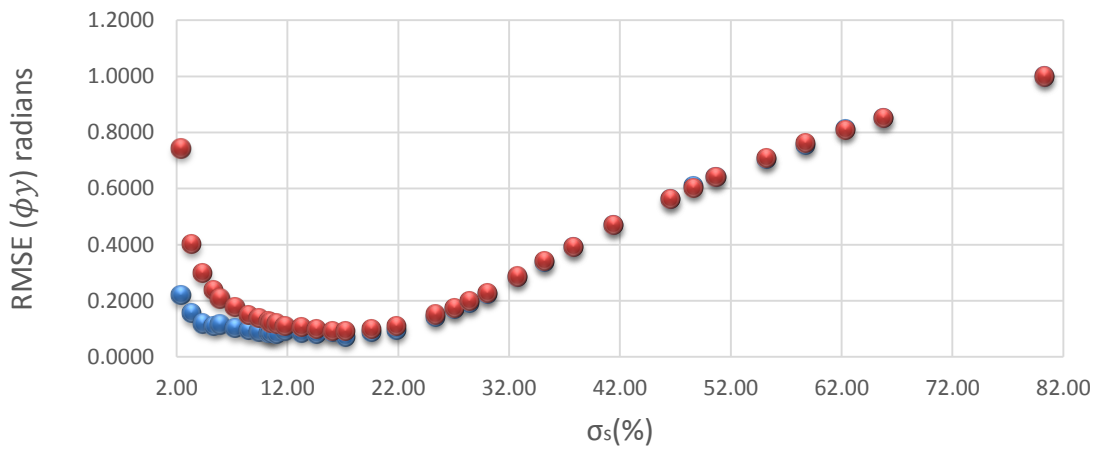


**Figure 30 - Overlay of normalized RMSE curves for CL (blue) and OL (red)  $y$ -tilt phase processes identify the same optimal spot region; maximum CL RMSE = 0.6589 and maximum OL RMSE = 15.656**



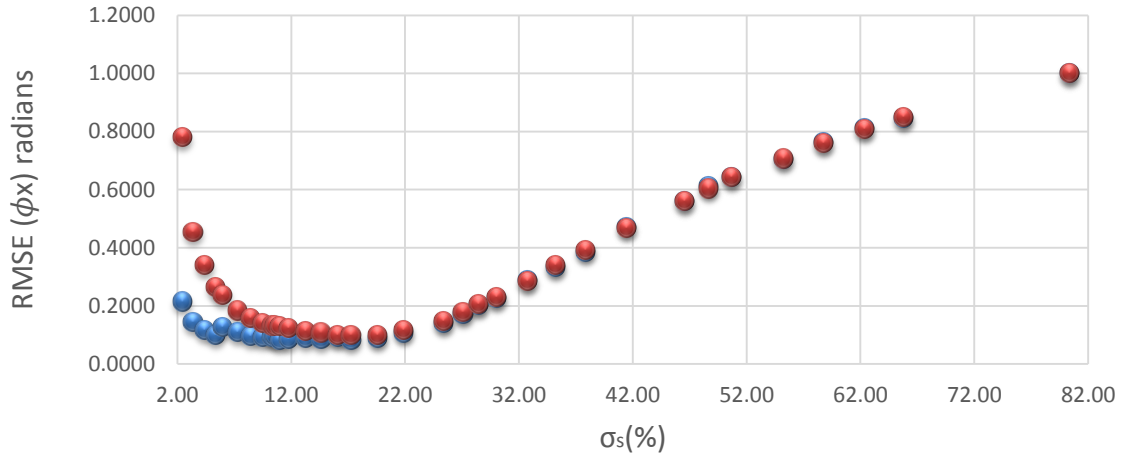


**Figure 31 - Overlay of normalized RMSE curves for CL (blue) and OL (red) y-tilt phase processes identify the same optimal spot region; maximum CL RMSE = 0.4418 and maximum OL RMSE = 14.694**

Most discernible from figures 30 and 31 is that the RMSE curves experience a minimum and maximum over the range of spot spreads as depicted by the bowl effect for the curves. The edges of the bowl correspond to large measurements errors induced by hyper-sensitive and torpid sensor responses. The minimum region implies the location for optimum spot spreads. This work normalizes RMSE values in reference to the maximum CL and OL RMSE values experienced such that process dependent measurement errors are suppressed. Furthermore, the normalization allows one to overlay the OL and CL RMSE curves on the same graph to identify an optimal spot spread region that simultaneously satisfy both OL and CL tilt phase envelopes. Therefore, figures 30 and 31 indicate the optimum spot spread region centers at about 17% for both phase envelopes.

### 3.6.2.2 Tilt Measurement Using Satellite and Missile Objects

Employing the results of the previous section, this work uses a Gaussian laser source having a spot spread of 17% to make optimal tilt phase measurements. Hereafter, this source serves as a baseline to assess PTS measurement performance with LEO objects.

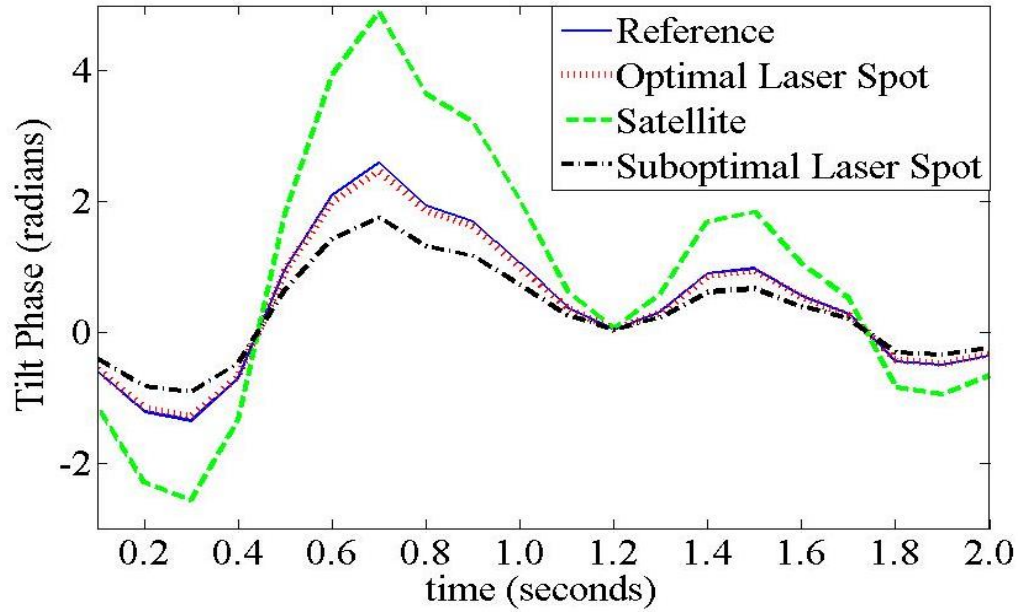


**Figure 32 - CL  $y$ -tilt phase measurement using satellite object as source**

Figure 32 depicts the measuring of a reference CL  $y$ -tilt phase process (blue-solid plot) using three sources. For conciseness, only satellite plots for  $y$ -tilt are presented; the plots for  $x$ -tilt allow the same conclusions. As expected, the optimal source (red-dotted plot) provides the best measurement having RMSE values of 0.0478 radians for  $y$ -tilt and 0.0362 radians for  $x$ -tilt; slight measurement offsets are due to fit inaccuracies of equation (3.33). The satellite object's  $y$ -spread and  $x$ -spread are about 47% and 56% respectively; setting the laser's spot spread to 47% and 56% results in sub-optimal measurements (black dash-dotted plot) having RMSE values of 0.3697 radians for  $y$ -tilt and 0.2480 radians for  $x$ -tilt. Measuring the tilt phase with the satellite object (green-dashed plot) results in RMSE

values of 1.0311 radians for *y-tilt* and 0.4179 radians for *x-tilt*. The significant measurement error means the satellite object provides an unreliable tilt phase measurement. Furthermore, the important conclusion to be made by comparing the green-dashed and black dash-dotted plots is that the satellite object's asymmetrical intensity distribution induces significant measurement error.

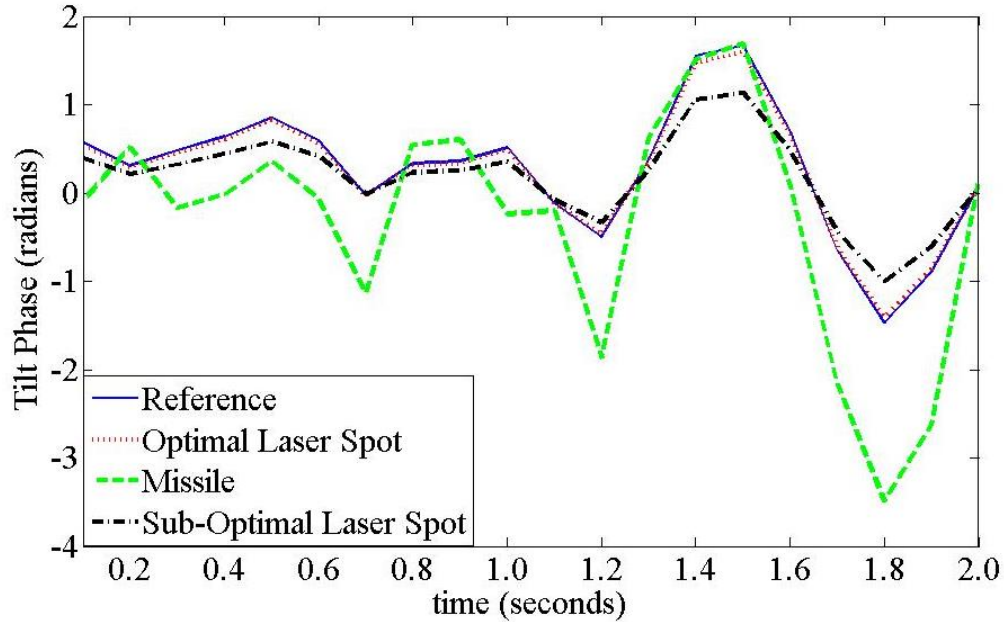


**Figure 33 - CL *x-tilt* phase measurement using missile object as source**

Likewise, figure 33 shows the results of measuring reference CL *x-tilt* phase process using three sources, but now the LEO object is a missile body. For conciseness, only missile plots for *x-tilt* are presented; the plots for *y-tilt* allow the same conclusions. The missile's (*y* and *x*) spreads are nearly identical at 44% because the missile body is set at a 45 degree angle with respect to the PTS. Setting the laser's spot spread to 44% results in a sub-optimal tilt phase measurement (black dash-dotted plot) having RMSE values of 0.3269 radians for *y-tilt* and 0.2280 radians for *x-tilt*. Measuring the tilt phase with the missile

object (green-dashed plot) results in RMSE values of 0.9147 radians for  $y$ -tilt and 0.9091 radians for  $x$ -tilt. Again, the important conclusion to be made by comparing the green-dashed and black dash-dotted plots is that the missile body's asymmetrical intensity distribution induces significant measurement error. Furthermore, the tilt phase measurements conducted with the LEO objects reveal that the satellite and missile objects elicit markedly different measurements, even for the same reference tilt process applied at the aperture. This only confirms the analysis in Chapter II that tilt phase measurement for LEO objects depend on their shape and intensity distribution.

### **3.6.3 Pseudo-tilt Phase**

This research reveals an additional complexity when measuring tilt phase from an LEO object with a PTS. If the object appears to rotate over the QUAD-cells during tilt measurement, then the cells will experience an intensity imbalance that registers as a false tilt phase disturbance. Object rotation may be inherent to the object's motion or induced by the imaging system. Telescopes employing a Coudé path may induce image rotation as the telescope slews to track an object [22].

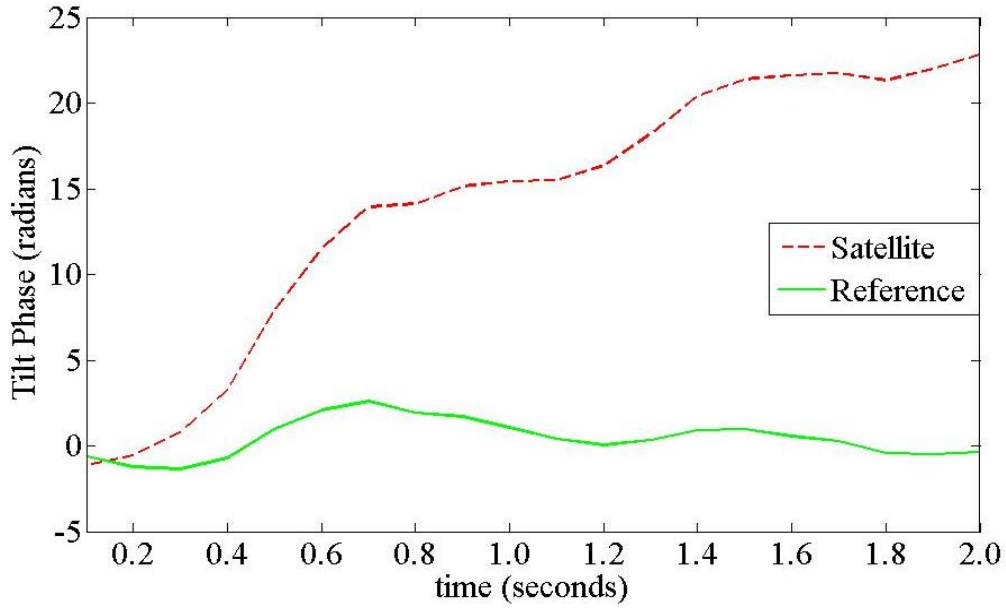


**Figure 34 - Tilt measurement using a CW rotating satellite**

Consider figure 34; the green-solid curve is the random reference tilt phase applied at the aperture and the red-dashed curve is the measured tilt phase using the satellite image. The measured tilt phase due to the clockwise (CW) rotating satellite object deviates substantially from the reference phase; this is reflected by a RMSE value about 17.2 radians.

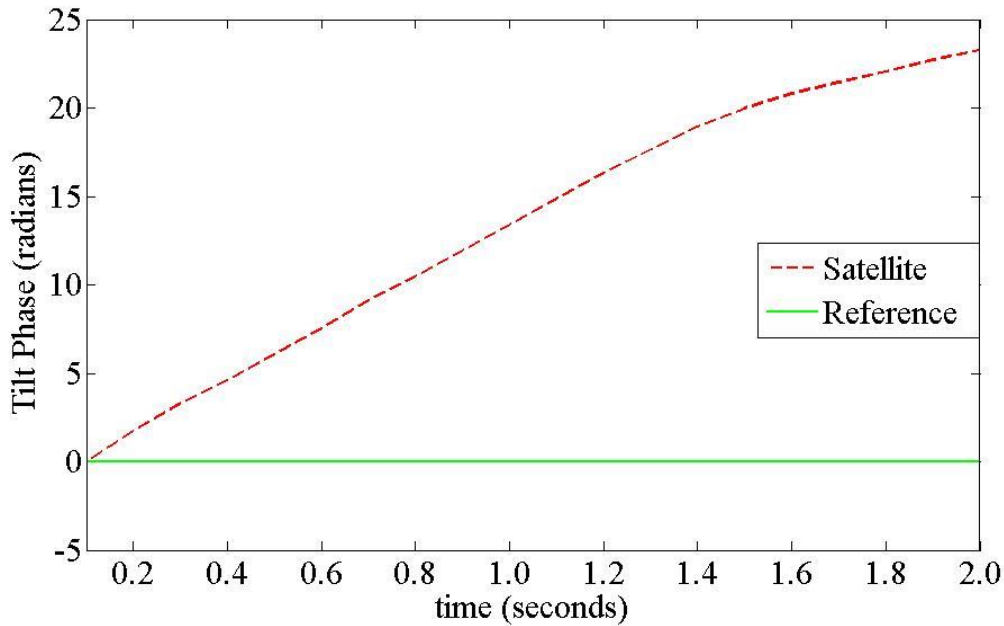


**Figure 35 – Green-solid curve represents zero reference tilt being applied at the aperture; red-dashed curve shows a non-zero measured tilt for the CW rotating satellite**

By setting the reference disturbance tilt to zero and rotating the satellite object at different rates and directions, this work isolates the pseudo-phase contribution. For example, the satellite image having no tilt disturbance is rotated CW at a moderate rate with respect to the PTS detector plane; this induces a pseudo-tilt phase having a positive phase slope contribution over the measuring period as shown by figure 35. Rotating the satellite counterclockwise (CCW) results in a negative phase slope contribution; the rate of satellite rotation affects the magnitude of the phase slope. Although not shown for conciseness, the rotating missile body elicit different tilt phase curves while allowing for the same conclusions to be made. Therefore, it is important to conclude that the pseudo-tilt phase contribution is arbitrary and depends on random LEO object shape, motion, and intensity distribution. Therefore, LEO objects present considerable measurement challenges to a

QUAD-cell detector; the following section proposes a methodology to address the respective challenges.

### 3.6.4 Create Symmetrical Intensity Distribution

The first task of the methodology is to transform the LEO object's asymmetrical intensity distribution to a symmetrical one. Recall the important conclusion made previously is that the QUAD-cell must have a symmetrical intensity distribution to optimally measure tilt distortion.

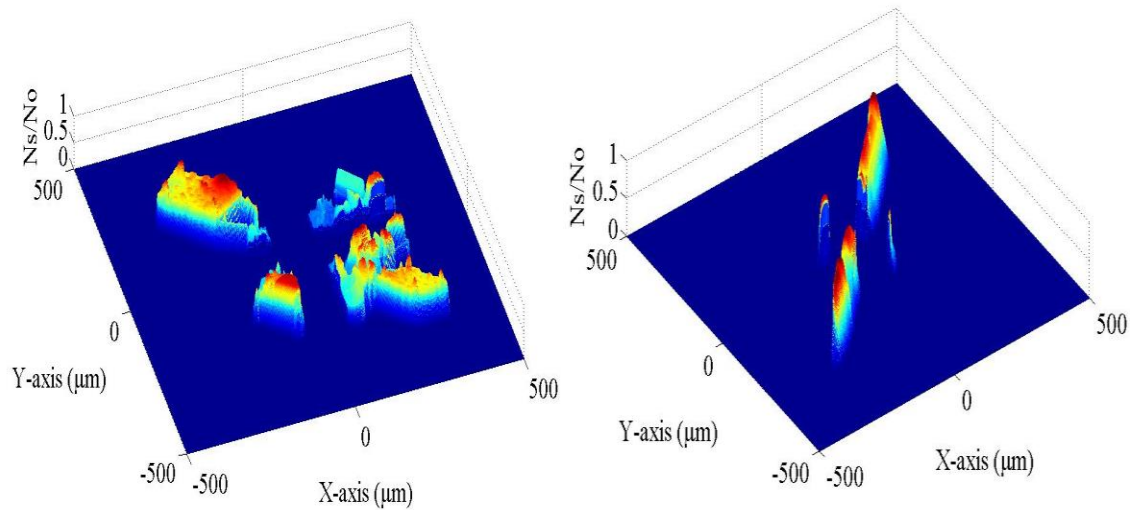


**Figure 36 - Satellite and missile intensity distribution over QUAD-cell region**

Consider figure 36 where the intensity distribution for the satellite and missile objects are displayed. The QUAD-cell partitions the asymmetrical distribution amongst the four cells and the source of measurement error becomes clearly evident, as each cell's intensity distribution differs markedly from the others. This condition makes it impossible for the PTS to map a given tilt disturbance to a unique intensity shift, as required. Therefore, this work proposes rotating the image of the satellite and missile objects like a spinning top over the QUAD-cell. As long as the rotation rate is faster than the PTS's frame rate, the

rotation creates an average intensity distribution that is symmetrical; reference figure 37. Additionally, the image rotation will null any pseudo-tilt phase effect. This work does not specify how to rotate LEO object images over the QUAD-cell region or rotation rates and therefore abstracts from these aspects of the methodology. Therefore, it is assumed a suitable image rotator exists to present a properly rotating image to the PTS optical leg.

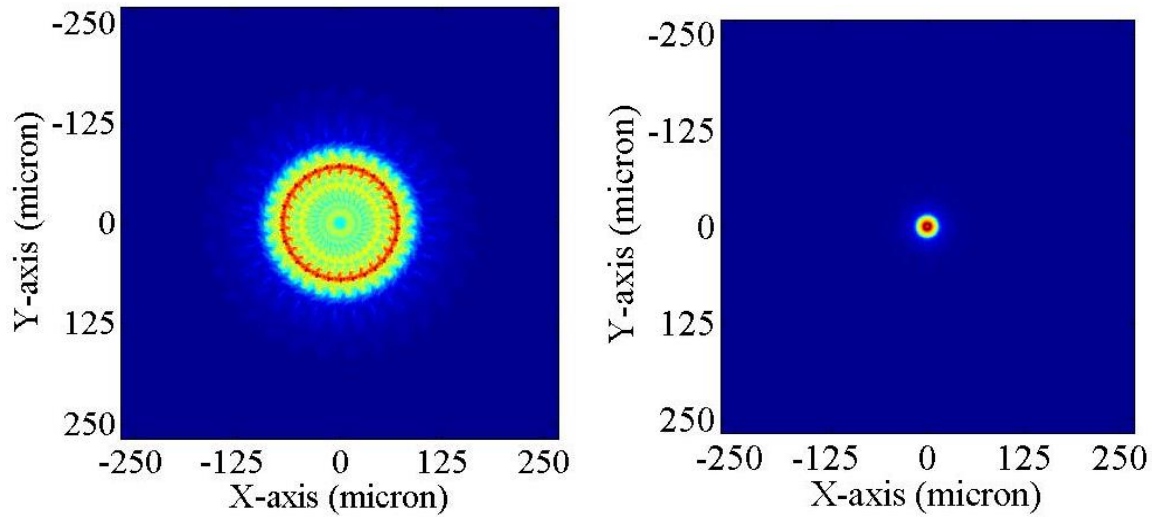


**Figure 37 - Rotated satellite (left) and missile (right) intensity distribution over the FPA**

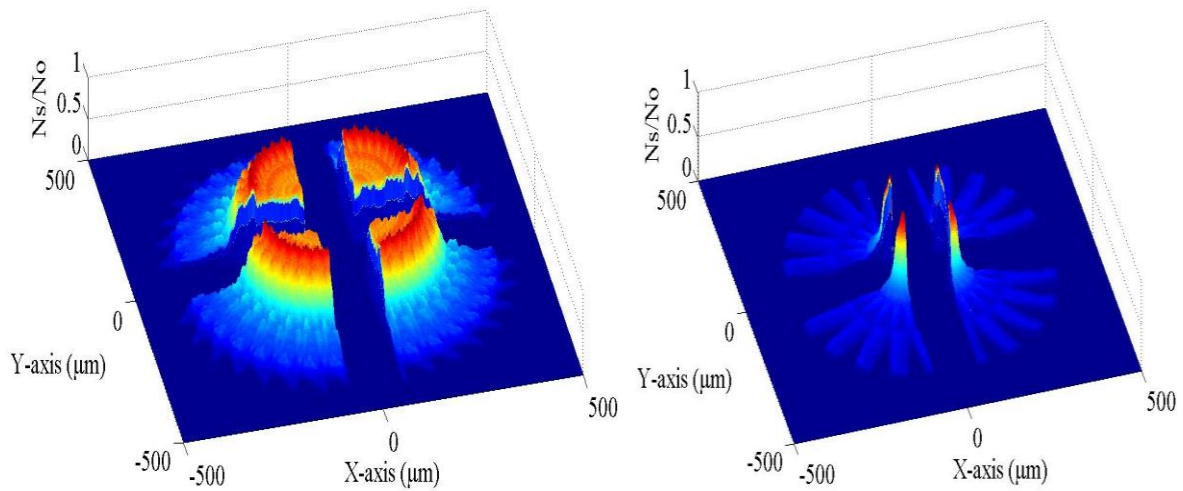


**Figure 38 - Rotated satellite (left) and missile (right) intensity distribution over the QUAD-cell**



Figures 37 and 38 particularly show the advantage of rotating the LEO objects over the QUAD-cell. The object rotation clearly creates an average intensity distribution that is symmetrical about the QUAD-cell region. Therefore, as tilt disturbance displaces the intensity distribution, the PTS can now map intensity shifts uniquely to a particular tilt disturbance. Using the rotated image as a source to the PTS, this work re-accomplishes the tilt measurements conducted in the previous section. Figure 39 shows the satellite object where the green-dashed plot is the measurement having no image rotation, the red-dotted plot is with image rotation, and the black dash-dotted plot is with image rotation and a compensation term (adaptive gain).

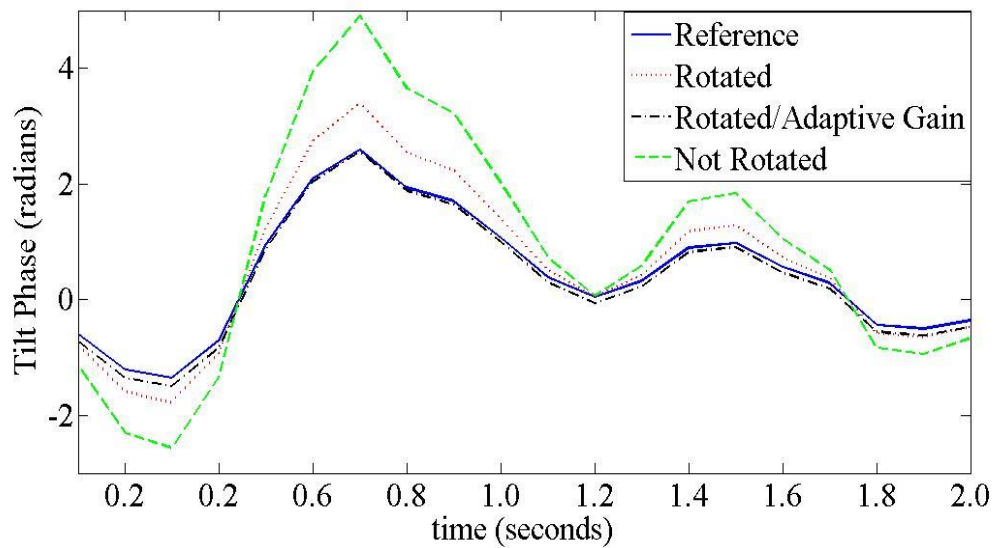


**Figure 39 – Tracking performance for rotating satellite image and adaptive gain to improve PTS y-tilt phase measurement**

**Table 6. Satellite Tilt Phase Measurements**

PTS Measurement Mode	RMSE_y (radians)	RMSE_x (radians)
Image Not Rotated	1.0311	0.4179
Rotated Image	0.3590	0.2410
Rotated Image + Gain	0.0888	0.0935

According to the RMSE values in table 5, measurement improvements of about 65% for *y-tilt* and 43% for *x-tilt* are attained thru image rotation. However, the rotated image still has a non-optimal spot spread and this methodology applies an adaptive gain term to restore optimal tilt measurement.

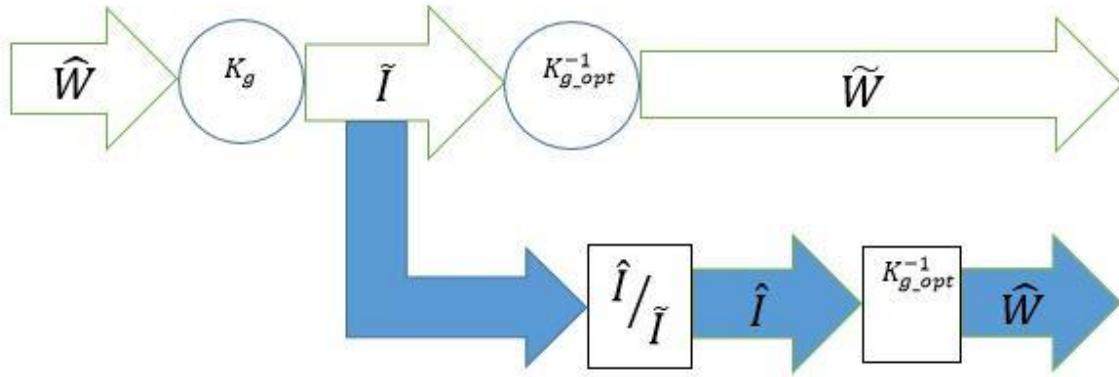


**Figure 40 - Adaptive gain term (blue path) being applied to recover original tilt disturbance,  $\hat{W}$**

Figure 40 displays the tilt signal path where the blue path represents the adaptive gain term,

$$K_c = \frac{1}{K_{g\_opt}} \hat{I}/\tilde{I}, \quad (3.34)$$

to compensate for a sub-optimal centroid gain,  $K_g$ . Recall that this term was derived in Section 2.7. Using the adaptive gain term along with image rotation, results in significant measurement improvements of about 91% for *y-tilt* and 76% for *x-tilt* with the simulated tilt processes.

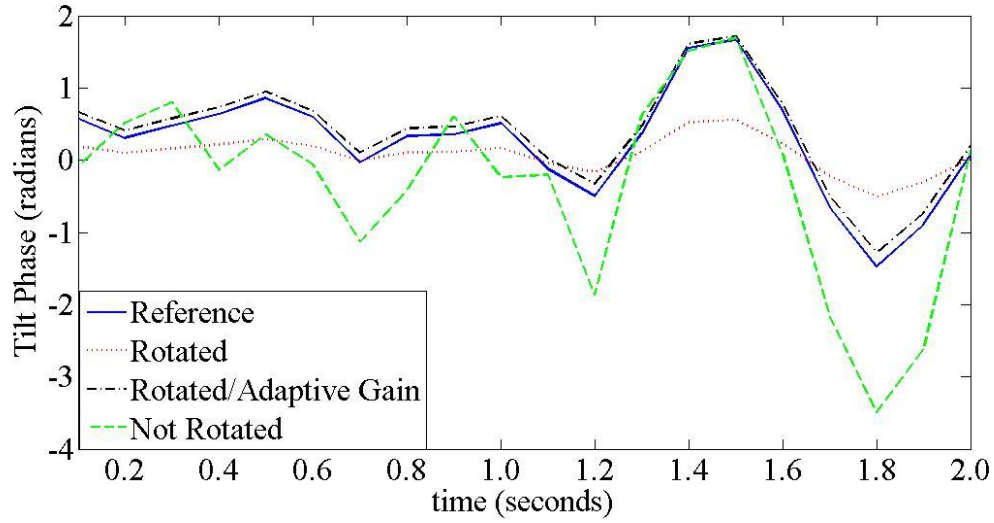


**Figure 41 – Tracking performance for rotating missile image and adaptive gain to improve PTS *x*-tilt phase measurement**

**Table 7. Missile Tilt Phase Measurements**

PTS Measurement Mode	RMSE_y (radians)	RMSE_x (radians)
Not Rotated	0.9147	0.9091
Rotated	0.7726	0.5193
Rotated + Adaptive Gain	0.1204	0.1183

Similarly, applying the image rotation and adaptive gain technique to the missile object results in significant measurement improvement about 87% for *y-tilt* and *x-tilt*; reference figure 41 and table 7. Although the proposed methodology reduces measurement errors substantially, some measurement error still remains on the order of 8% to 12%. There are two contributing sources of the residual measurement errors. The rotated images have large spot spreads and recall that the fit inaccuracy of equation (3.33) becomes pronounced for large spot spreads, as previously discussed. The other source of measurement error is due to the  $\hat{I}/\tilde{I}$  term of the adaptive gain being inexact for some intensity distributions.

Ultimately, the simulated methodology shows that it enables accurate tilt distortion measurement of an LEO object having an asymmetrical shape and/or intensity distribution. Any slight measurement offsets can be compensated for with a tilt tracker having sufficient bandwidth.

## IV. Analysis and Results for the Adaptive Tilt Tracker

The culmination of this work is the development and demonstration of an effective adaptive tilt tracker. Therefore this section aims to coalesce the different concepts introduced in Chapter II and employ the methodology born out of Chapter III. Specifically, the tracker will operate under the assumption that a suitable image rotator has created a symmetrical intensity distribution for the PTS such that the application of an adaptive gain restores optimality. As discussed in Chapter II, the goal of the adaptive tracker is to detect and counteract deviations from optimal  $SNR_v$  and  $K_g$  parameters. What follows is a thorough description of adaptive tilt tracker behavior and concepts where the tracker uses the dither mirror technique to measure an arbitrary  $K_g$ .

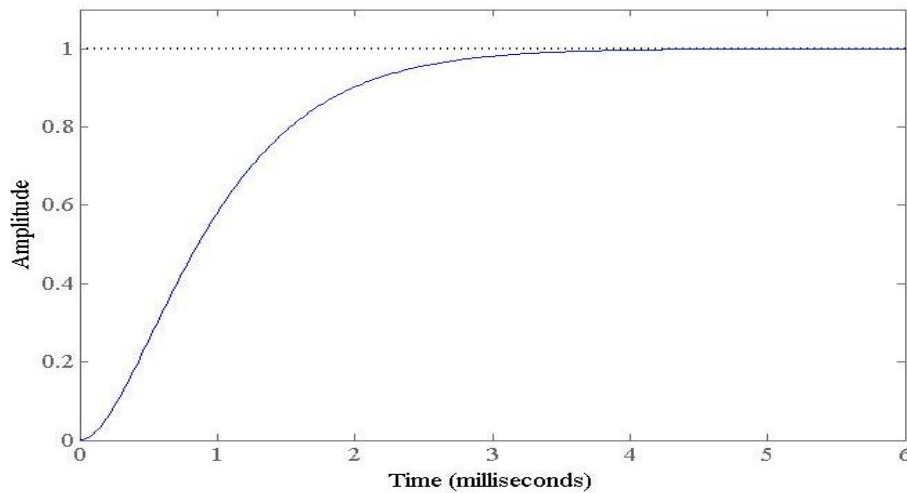
### 4.1 System Description

#### 4.1.1 Fast Steering Mirror (FSM)

The tracker's frequency response and robustness mirrors that of the FSM; therefore, a description of its qualities is warranted. The modeled FSM has suitable compensation qualities for the modeled optical system. It has a maximum throw of  $\pm 7 \mu\text{rad}$ ; about  $\pm 6.82 \mu\text{rad}$  correspond to approximately 99% of all tilt phase deviations over the telescope's aperture; therefore, the FSM provides ample compensation over the expected dynamic range of tilt distortion. Furthermore, the FSM has a maximum bandwidth of 200 Hz that exceeds the tilt bandwidth by about 455%. Reference table 8 for FSM specifications.

**Table 8. FSM Specifications**

Specification	Value
Maximum Throw	+/- 7 $\mu$ rad
$f_{3dB}$	200 Hz
Settling time, $t_s$	3.0 ms
Damping ratio, $\zeta$	1.0
Phase Margin, $\gamma_{PM}$	76.3°
Gain Margin, $\gamma_{GM}$	26.8 dB

**Figure 42 - Step response for a critically damped FSM**

This work applies adaptive techniques to a tracker that has an optimally controlled FSM; therefore, the modeled FSM has excellent gain and phase margins. Furthermore, the FSM is critically damped, having a response that resembles a fast first order system as shown by figure 42.

#### 4.1.2 Determine $K_{g\_opt}$

Recall the results of Section 3.6.2.1 where a set of Gaussian spot spreads correlate to an optimum spot spread region. Within this region, a spot spread of about 17% resulted in the smallest RMSE values; therefore, this work uses this spot spread and corresponding centroid gain of 0.0049 for  $K_{g\_opt}$ . For a fixed optical system configuration, the measurements conducted in Section 3.6.2.1 occur during a one-time system calibration; therefore,  $K_{g\_opt}$  is considered a system constant.

#### 4.1.3 Determine Dither Throw and Frequency

Once  $K_{g\_opt}$  is determined, the adaptive tracker must use this term to detect a sub-optimal  $K_g$  by dithering the FSM with a known throw and frequency. As described in Chapter II, any deviation from  $K_{g\_opt}$  is detectable by comparing PTS output signals,  $\hat{I}$  for  $K_{g\_opt}$  and  $\tilde{I}$  for an arbitrary  $K_g$ .

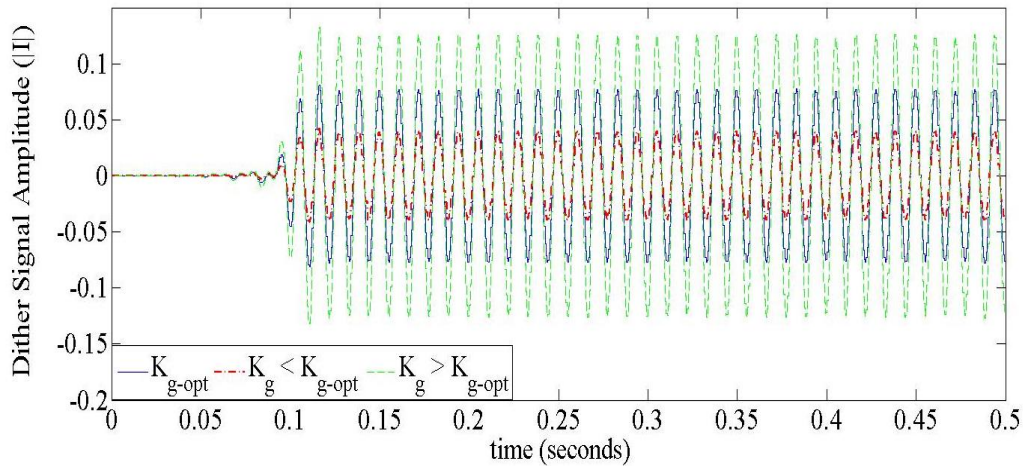


**Figure 43 - Comparison of dither signals that correspond to optimal and suboptimal centroid gains**

Consider figure 43 where the reference dither signal for  $K_{g\_opt}$  (blue-solid plot) is compared to two general cases for an arbitrary  $K_g$  dither signal. The green-dashed plot represents a suboptimal gain greater than  $K_{g\_opt}$  that results in an amplified dither signal. The red dash-dotted plot is for a suboptimal gain less than  $K_{g\_opt}$  that results in an attenuated dither signal. Therefore, deviations from  $K_{g\_opt}$  are readily detectable and map correspondingly to variations of dither signal amplitude.

This work chooses a sinusoidal waveform for dither signals where the reference and arbitrary dither signals are respectively described by,

$$\begin{aligned} |\hat{I}| \cos(\omega t) \\ |\tilde{I}| \cos(\omega t), \end{aligned} \tag{4.1}$$

where  $|\hat{I}|$  is determined by the commanded dither throw. This research commands the FSM to dither at  $\pm 1.73 \mu\text{rad}$  for an average  $|\hat{I}|$  of 0.077. The command signal operates well within the mechanical constraints of the mirror while generating a  $|\hat{I}|$  that is detectable amongst noise. Additionally, the FSM dithers at 90 Hz to oscillate the dither signal approximately twice as fast as the Tyler frequency.

#### 4.1.4 Determine Dither Filter

The dither signal for an arbitrary LEO object will be disturbed by band-limited white noise (BLWN) and atmospheric tilt disturbance as shown by figure 44. Essentially, the atmospheric tilt disturbance creates a wandering average for the dither signal to oscillate about and the BLWN noise varies the dither signal's peak to peak amplitude.



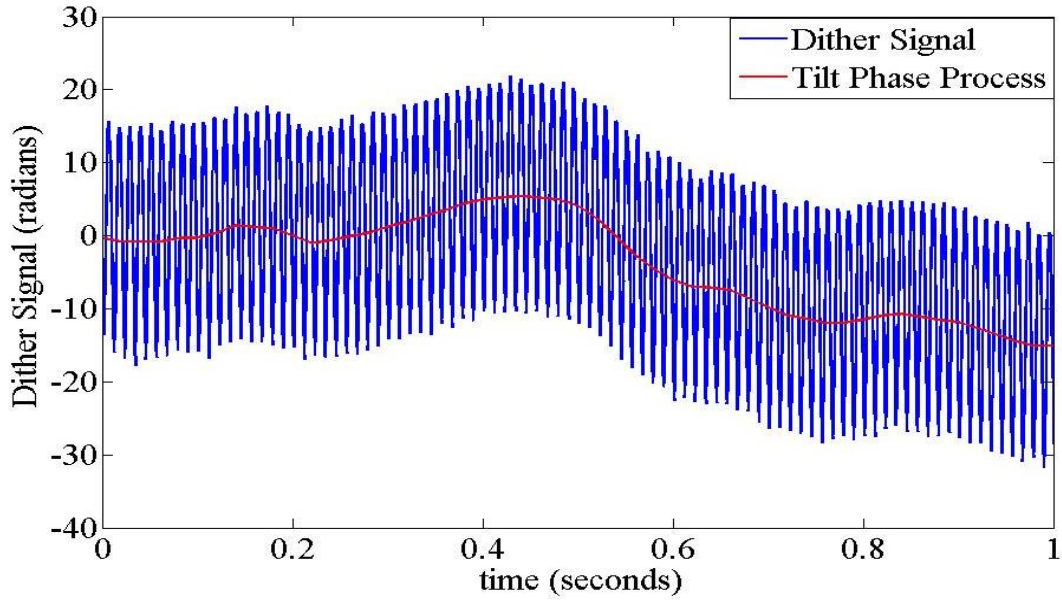


**Figure 44 - Dither signal shown in tilt phase units being disturbed by atmospheric tilt disturbance and band-limited white noise**

This work implements a dither band-pass filter to suppress disturbance sources such that the intended object dither signal,  $|\tilde{I}| \cos(\omega t)$ , is recovered. The filter shown in figure 45 has a center-band frequency corresponding to the dither frequency. Furthermore, frequencies below 50 Hz and above 140 Hz are attenuated at about -65 dB.

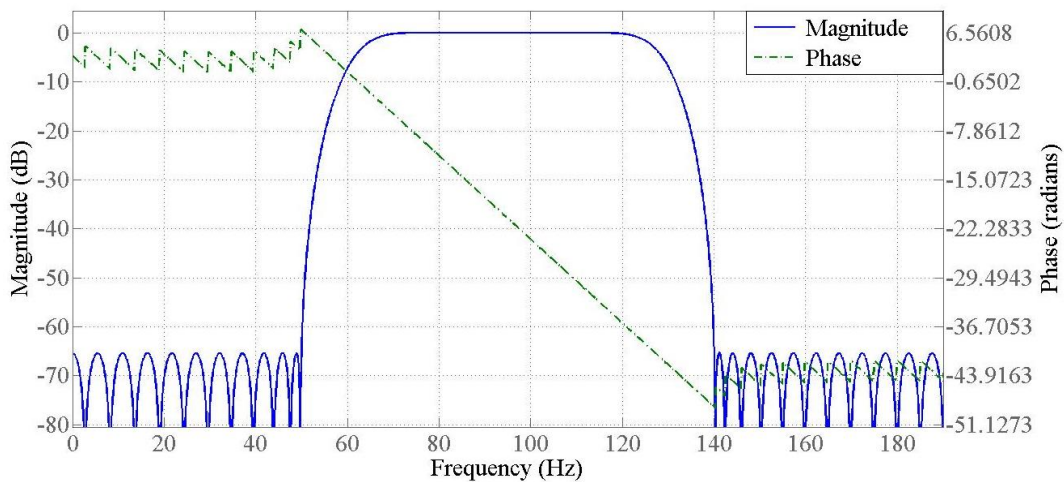


**Figure 45 - Dither band-pass filter response with a center-band frequency of 90 Hz**

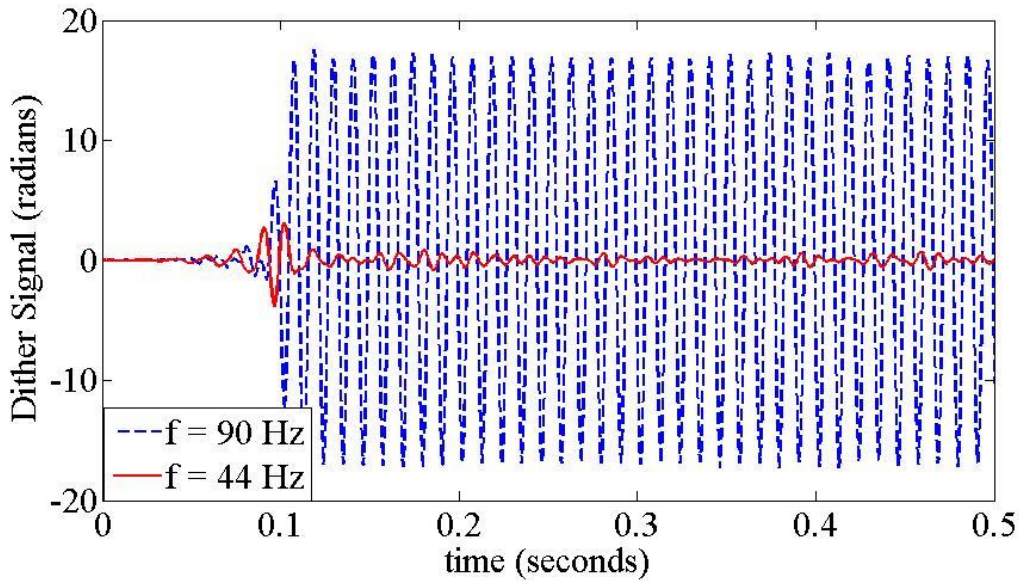


**Figure 46 - Dither filter passing dither signal at 90 Hz (dashed-plot) while suppressing signal oscillating at tilt bandwidth frequency of 44 Hz**

Therefore, the atmospheric tilt process having an effective bandwidth of 44 Hz is severely attenuated and for many dither cycles, the BLWN contribution can be made fairly negligible over the pass-band of the filter; reference figure 46. Also, notice the time delay of the filter output corresponding to the dither signal (dashed-plot) where it does not reach steady state until about 0.13 seconds. The delay is due to the filter's linear phase delay response throughout the pass-band region as depicted by the green-dashed plot of figure 45; therefore, the dither signal has a phase delay of about 17.7 radians.

#### **4.1.5 Determine Dither Period**

The calibration period to determine an arbitrary  $K_g$  must balance the constraints of being short as possible while providing a suitable dither signal. In general, both FSM axes may require dithering which increases the overall dither period and processing time. Since the intensity distribution is symmetrical, only one FSM axis needs to be dithered because

the  $K_{gx}$  and  $K_{gy}$  gains are identical. Therefore, this work only dithers the FSM  $x$ -axis. Another reason for dithering the FSM at 90 Hz is to provide enough dither cycles over a relatively short period of time. Accordingly, this work sets a dither period of 0.26 seconds where 12 steady state dither cycles are achieved from 0.13 to 0.26 seconds; furthermore, the dither period accounts for about six tilt time constants,  $6\tau_T$ , where  $\tau_T$  is the reciprocal of  $f_{TG}$ .

#### 4.1.6 Determine Adaptive Gain, $K_c$

Applying the correct  $K_c$  term involves taking the ratio of the reference and object dither signals and scaling the result by  $(K_{g\_opt})^{-1}$  as follows,

$$K_c = \frac{|\hat{I}| \cos(\omega t)}{|\tilde{I}| \cos(\omega t)} (K_{g\_opt})^{-1} = \left| \frac{\hat{I}}{\tilde{I}} \right| (K_{g\_opt})^{-1} = \Delta I (K_{g\_opt})^{-1}, \quad (4.2)$$

where the ratio of signals only considers the amplitudes and therefore reduces to a ratio of amplitudes. Since  $|I|$  occurs twice over a dither cycle, the dither period yields 24 measurements of dither amplitude. Averaging the 24 measurements reduces BLWN effects; therefore,  $|\hat{I}|$  and  $|\tilde{I}|$  correspond to average amplitudes over the dither period. Since the average  $|\hat{I}|$  value is a known constant of 0.077, only  $|\tilde{I}|$  needs to be determined during the dithering process.

#### 4.1.7 Determine Frame Rate, $f_s$

As discussed in Chapter II, the adaptive tilt tracker adjusts the PTS's frame rate,  $f_s$ , in order to keep measurement error relatively low for waning signal levels. Consider figure 47 where  $f_s$  ranges (10.0 to 2.52) kfps; recall these values were determined for  $f_{max}$  and  $f_0$  in Sections 3.5.1 and 3.5.2.

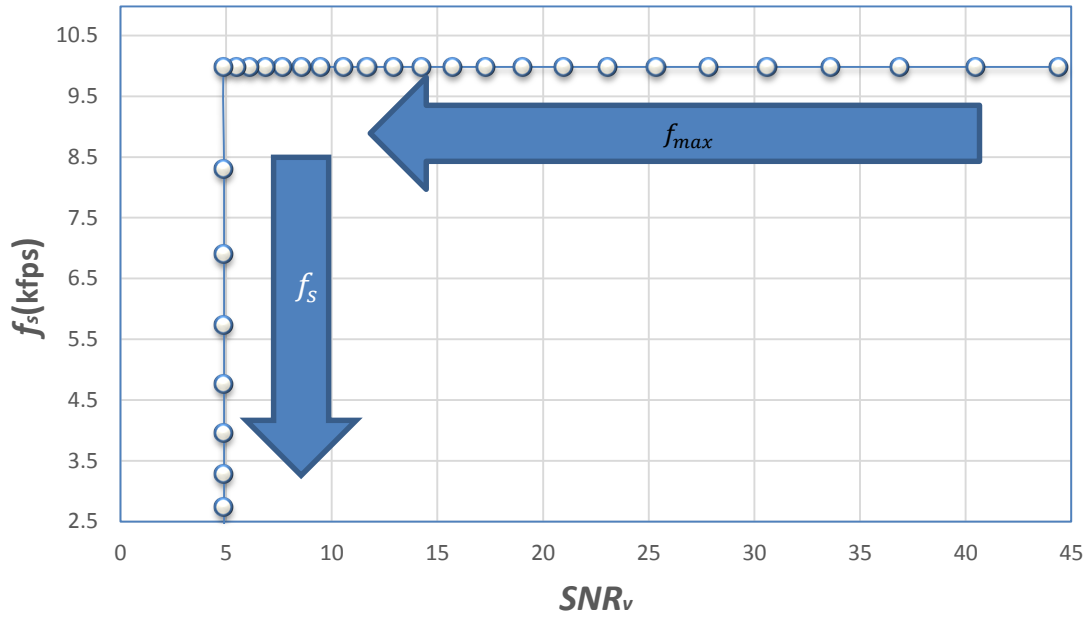


**Figure 47 – Detector’s frame rate is being adjusted according to  $SNR_v$ ; the horizontal arrow represents  $f_{max}$  as long as  $SNR_v > 5$ . The downward arrow represents  $f_s$  to sustain  $SNR_{v_0}$**

The horizontal arrow of figure 47 shows that as long as the  $SNR_v$  value is greater than or equal to  $SNR_{v_0}$ , the PTS will operate at  $f_{max}$ . Once the signal level wanes such that the PTS cannot sustain a signal level of at least  $SNR_{v_0}$ , the frame rate must be reduced from  $f_{max}$ . The downward arrow of figure 47 shows the frame rate being adjusted along a vertical line that corresponds to  $SNR_{v_0}$ . The downward trending dots along the vertical line particularly show the tradeoff in frame rate for signal level.

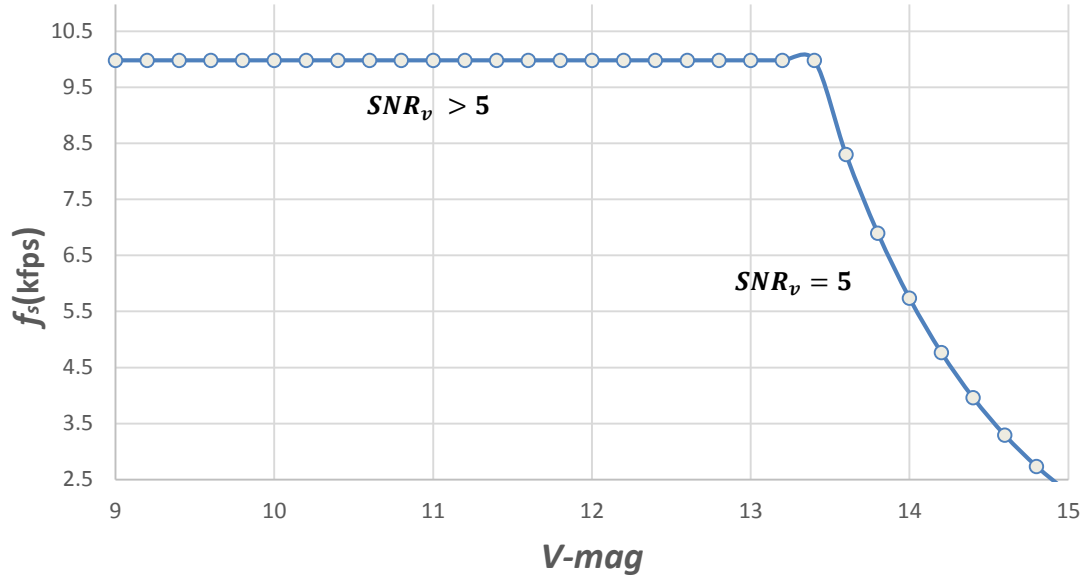


**Figure 48** – Flat portion of curve shows that for V-mags that correspond to a  $SNR_v > 5$ , the tracker operates at  $f_{max}$ . Decaying portion of curve shows detector frame rate being adjusted downward from  $f_{max}$  to sustain a  $SNR_v = 5$ . The V-mag value at  $f_0$  corresponds to the limiting V-mag for the tracker.

Figure 48 presents an alternate view for frame rate being adjusted according to signal levels. The frame rate dependence on V-mag allows the determination of the limiting V-mag for the tilt tracker. Accordingly, for a  $f_0$  of 2520 Hz, the limiting V-mag for the tracker is about 14.8.

## 4.2 Non-Adaptive Tilt Tracker Behavior

Before demonstrating the adaptive tilt tracker, it is important to demonstrate and analyze the behavior of the non-adaptive tilt tracker when the PTS's response deviates from optimal in the presence of a loop delay. Although the tilt tracker tracks a time varying tilt process, the tracker's performance can adequately be characterized by the tracker's step response. By definition, a tracker operating at  $f_{T_G}$  has a residual temporal error,  $\sigma_{temp}$ , of  $\lambda/D$  [14]. Consider the following ratio,

$$\sigma_{temp}/\sigma_{G\_tilt} \approx 0.07, \quad (4.3)$$

where the residual error is compared to the aperture  $G\_tilt$ . The value of equation (4.3) means that approximately 93% of the one-axis, one-sigma  $G\_tilt$  deviation over the aperture occurred at frequencies no greater than  $f_{T_G}$ . Additionally, the  $G\_tilt$  PSD of figure 17 indicates that tilt distortion beyond  $f_{T_G}$  is severely attenuated. Therefore, the effective tilt distortion is approximately constant over a compensation cycle if a tilt tracker operates (compensates) at a frequency greater than  $4f_{T_G}$ . Since the simulated trackers operate at 200 Hz, the simulated tilt processes with a  $f_{T_G}$  of 44 Hz appear as a series of gradually varying step inputs to the tracker.

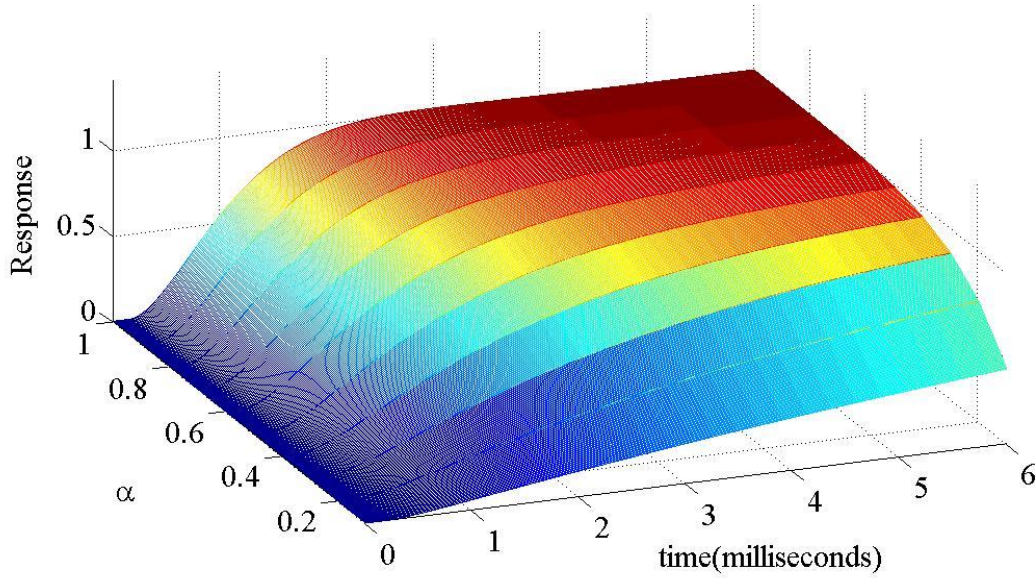


**Figure 49 - Non-adaptive tracker response curves for a unit step input and total delay time of 150  $\mu$ s where the curves are evaluated over varying normalized detector response,  $\alpha$ .**



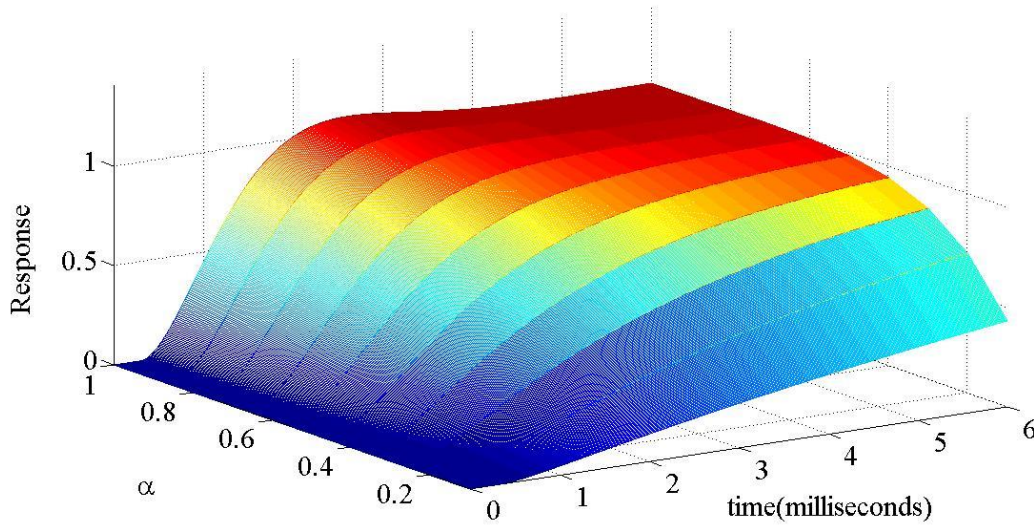


**Figure 50 - Non-adaptive tracker response curves for a unit step input and total delay time of  $298.75 \mu s$  where the curves are evaluated over varying normalized detector response,  $\alpha$ .**

Consider figure 49 where the non-adaptive tracker operates at  $f_{max}$  for a total delay time of  $150 \mu s$ . The unit step response is chosen to evaluate the tracker's transient and steady state performance versus varying normalized detector response,  $\alpha$ . Recall a unity value for  $\alpha$  corresponds to optimal PTS response; consequently, this is when the tracker has its optimal response to the step input of figure 49. As  $\alpha$  trends downward from unity to 0.10, the tracker response becomes increasingly sluggish, a signature indicator that the tracker's bandwidth is decreasing. Above an  $\alpha$  of about 0.50, the transient response suffers the most as the rise time increases; however, the steady state performance is still preserved. Below an  $\alpha$  of about 0.50, the transient and steady state performances suffer, eventually leading to a torpid tracker response at an  $\alpha$  of 0.10. Figure 50 shows the tracker response where the tracker operates at  $f_0$  and the total delay is  $298.75 \mu s$ . Besides a greater time delay for the response, the most salient difference shown by figure 50 in relation to figure

49 is a slight overshoot for the optimal response; otherwise, the response curves are nearly identical. Additionally, figures 49 and 50 show there is seemingly no risk of the tracker becoming unstable as  $\alpha$  trends downward from unity; this actually confirms the derived equations (3.22) and (3.29) for respective  $GM$  and  $PM$  where an  $\alpha$  less than unity, in the presence of a delay, increases the stability margins.

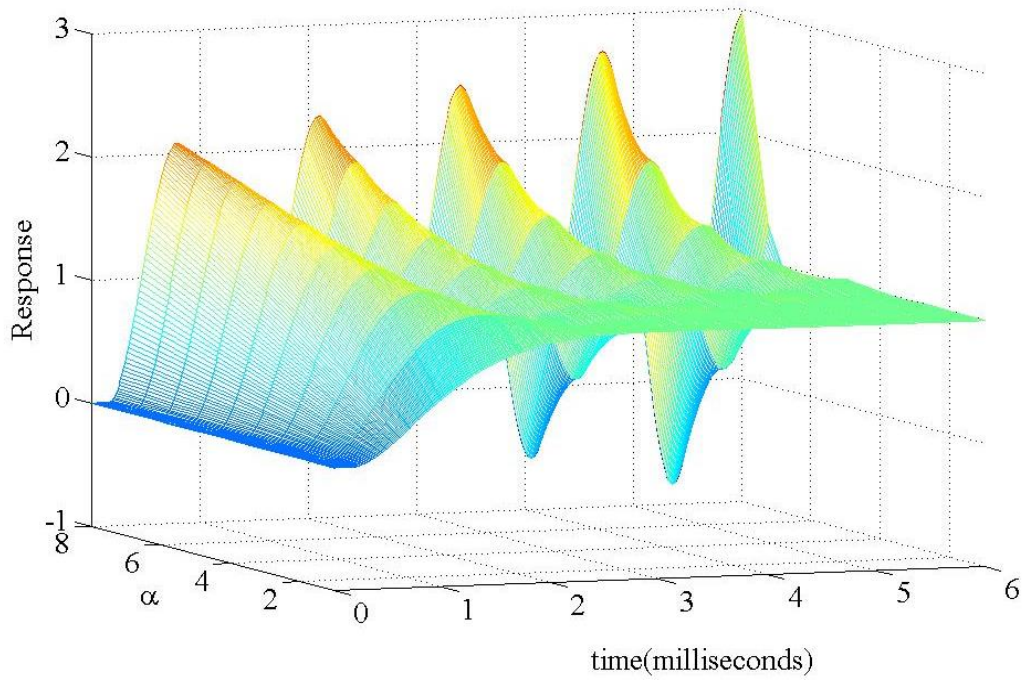


**Figure 51 - Non-adaptive tracker response curves for a unit step input and total delay time of  $150 \mu s$  where the curves are evaluated over varying normalized detector response,  $\alpha$ .**



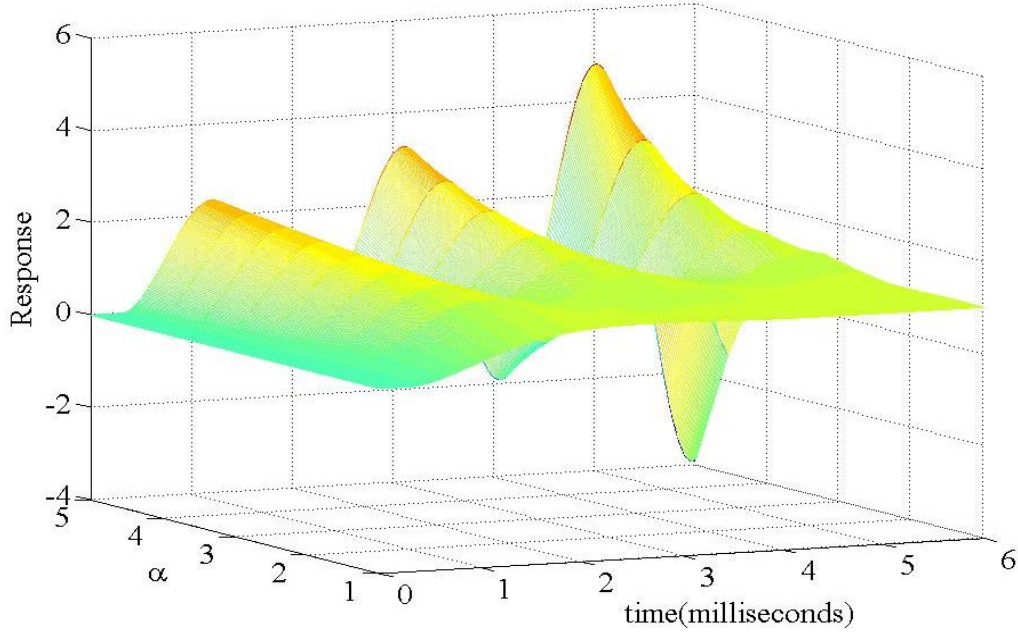


**Figure 52 - Non-adaptive tracker response curves for a unit step input and total delay time of  $298.75 \mu\text{s}$  where the curves are evaluated over varying normalized detector response,  $\alpha$ .**

Figures 51 and 52 present the results for an upward trending  $\alpha$  from unity. Again, the figures show a unity value for  $\alpha$  corresponds to optimal tracker response. Consider figure 51 where the tracker operates at  $f_{max}$  and notice that as  $\alpha$  increases from unity to eight, the tracker's response correspondingly exhibits oscillations and overshoot. Furthermore, the tracker clearly becomes unstable when  $\alpha$  is about eight. Figure 52 shows the tracker operating at  $f_0$  and therefore having a larger delay than when operating at  $f_{max}$ . Notice the increase in delay time causes the tracker to reach instability sooner at  $\alpha$  equal to five, as opposed to eight when operating at  $f_{max}$ . This confirms the conclusions made from the derived *PM* and *GM* equations that a delay erodes stability margins and in the presence of a delay, an increasing  $\alpha$  beyond unity compounds the effect. Clearly, an increasing  $\alpha$  beyond unity carries the risk of tracker instability.

### 4.3 Demonstration of the Adaptive Tilt Tracker

This work uses SIMULINK®, a MATLAB® tool, to model and simulate the non-adaptive and adaptive tilt trackers; only the adaptive tracker is shown for conciseness. Furthermore, tracker models are sampled-data control systems that sample the residual tracker error via the PTS. Therefore, the discrete time control systems have a sample rate equal to the PTS's frame rate. The adaptive tracker model is shown in figures 52 and 53 and briefly discussed in table 9.

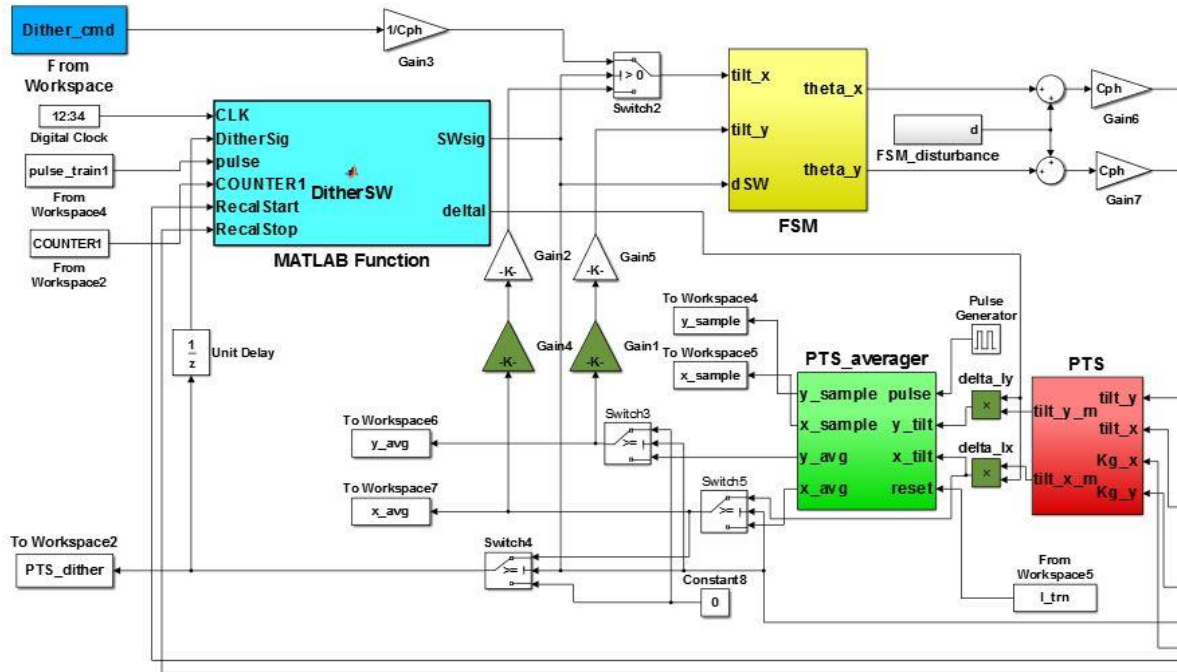


**Figure 53 - Left-half of adaptive tilt tracker model where the significant features are highlighted and discussed in table 9.**

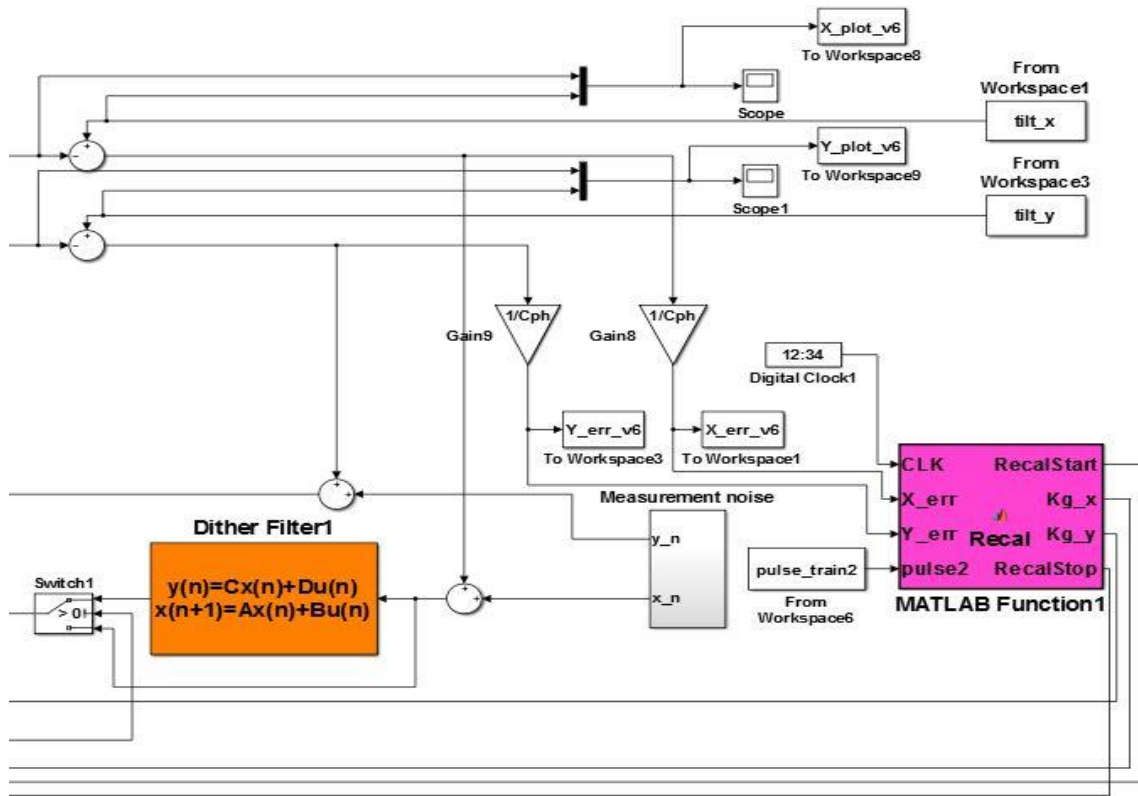
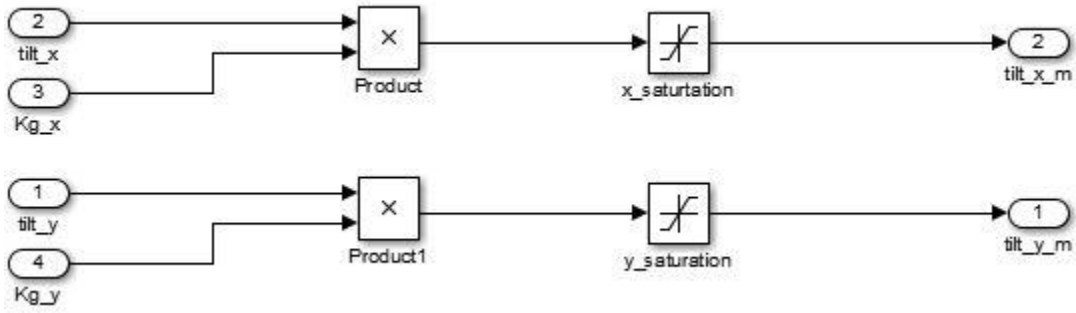


Figure 54 - Right-half of adaptive tilt tracker model where the significant features are highlighted and discussed in table 9.

**Table 9. Adaptive Tracker Component Description**

<b>Component Color Code</b>	<b>Component Description and Functions</b>
Dither command	Dithers only the FSM $x$ -axis when the tracker is in open loop configuration at an amplitude of $\pm 1.73 \mu\text{rad}$ and frequency of 90 Hz
Dither Mode Switch	MATLAB <sup>®</sup> script places the tracker in dither or track mode; commands dither when tracker first initializes or when the tracker's average tilt angle error deviates beyond optical system's diffraction angle zone; measures arbitrary dither signal, calculates and applies $\Delta I$ term for adaptive gain, $K_c$
FSM	Discrete time model for $x$ and $y$ FSM axis having identical responses; model incorporates plant, controller, and loop delay; output of discrete model is made continuous through a zero-order hold operation; FSM outputs have saturation limits of $\pm 7.0 \mu\text{rad}$
$K_c$	Represents adaptive gain composed of $\Delta I$ and $(K_{g\_opt})^{-1}$ terms; adaptive gain is identical for $x$ and $y$ tracker legs
PTS signal "averager"	MATLAB <sup>®</sup> script that samples and averages PTS output signals to reduce the variance envelope in the presence of band limited white noise
PTS	Model for identical $x$ and $y$ PTS responses; responses are represented by identical, arbitrary centroid gain terms; PTS outputs have saturation limits at $\pm 1$
Dither Filter	Discrete model for a band-pass filter that filters the dither signal to abate atmospheric tilt disturbance and band limited white noise; only active when tracker is in dither mode
Tracker Recalibration	MATLAB <sup>®</sup> function measures average residual tilt angle error for $x$ and $y$ tracker outputs, then compares values to specified threshold (optical system's diffraction angle); when threshold is reached/exceeded, the recalibration function triggers the dither switch function to recalibrate the tracker
Measurement Error	Induces measurement error according to equation 2.41; dependence on spot size error is suppressed such that the measurement error only depends on $SNR_v$



**Figure 55 - SIMULINK<sup>®</sup> model for PTS having independent  $K_{g_x}$  and  $K_{g_y}$  responses that are determined by image spot characteristics**

It is important to reemphasize that the image spot characteristics for the PTS are determined by atmospheric turbulence, optical set-up, and object characteristics such as size, shape, motion, and intensity distribution. All of these variables that determine spot size are encapsulated in two parameters in the SIMULINK<sup>®</sup> model,  $K_{g_x}$  and  $K_{g_y}$ , for the PTS's response. Assuming an image rotator creates a symmetrical spot,  $K_{g_x}$  and  $K_{g_y}$  become identical. Figure 55 shows the PTS's model treating the centroid gain term as a signal to be multiplied with the tilt disturbance signal; this is to model the centroid gain as a parameter that arbitrarily changes in real-time as it realistically does. Consider the following comparisons for the non-adaptive and adaptive tilt trackers where their responses to varying  $K_{g_x}$  and  $K_{g_y}$  are demonstrated.

For the following scenarios discussed, the PTS operates at either  $f_{max}$  or  $f_0$  to sustain a  $SNR_v$  of five, so measurement error due to signal levels is not a significant limitation for the simulated tracker performance. Additionally, the trackers are evaluated for a uniform distribution of  $\alpha$  ranging from 0.10 to 2.45. The uniform distribution reflect the realistic approximation that a particular  $\alpha$  value is no more likely than another. The range reflects that  $\alpha$  does not assume extreme values where the adaptive tracker is ineffective. For point-like spot sizes (very large  $\alpha$ ) or very large spot sizes (very small  $\alpha$ ), the adaptive tracker has little to no effect.

Since tracker performance is typically referenced about an optical system's diffraction angle, the tracker's residual phase error is converted to residual tilt angle error using the following relationship,

$$\begin{aligned}\theta_{err} &= \phi_{err} \left( \frac{4}{kD} \right) \\ k &= \frac{2\pi}{\lambda},\end{aligned}\tag{4.3}$$

where the conversion factor,  $4/kD$ , uses the angular wave number,  $k$ , to translate the optical phase,  $\phi_{err}$  (radians), to tilt angle,  $\theta_{err}$  (nanoradians). Over a tracking period, the trackers report average residual tilt angle error and corresponding standard deviation, given by

$$Tracker\ Error = \bar{\theta} \pm \sigma_{\theta},\tag{4.4}$$

where  $\bar{\theta}$  is the mean of a series of error measurements taken over a time period;  $\sigma_{\theta}$  accounts for the variability from the mean.

#### 4.3.1 Scenario 1 ( $\alpha$ less than unity for $f_{max}$ )

With a normalized non-optimal PTS response corresponding to an  $\alpha$  of 0.10, the non-adaptive tracker response lags the aperture  $x$ -tilt phase process as expected; reference figure 56. The tracker response translates to an absolute average residual tilt angle error,  $|\bar{\theta}| \pm \sigma_{\theta}$ , of  $33.95 \pm 290.84$  nrad. Since the tracker error deviates beyond the optical system's diffraction angle of 142.86 nrad, the tracker is not effective in caging the residual error within the diffraction angle zone. Therefore, tilt distortion of the image becomes noticeable.

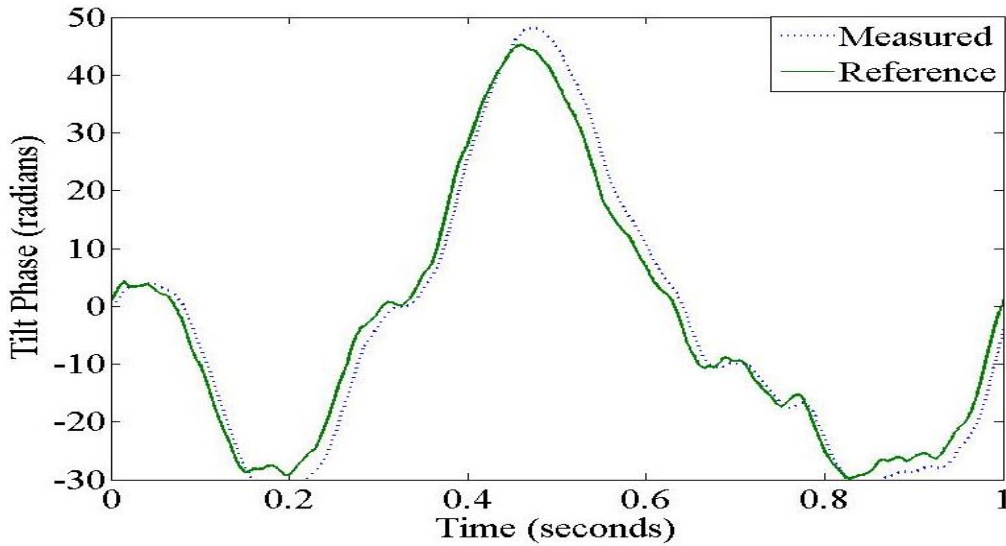


**Figure 56 - Response for non-adaptive tilt tracker with  $\alpha$  equal to 0.10 is shown by the dotted blue curve lagging the aperture tilt phase reference, shown by the solid green curve.**

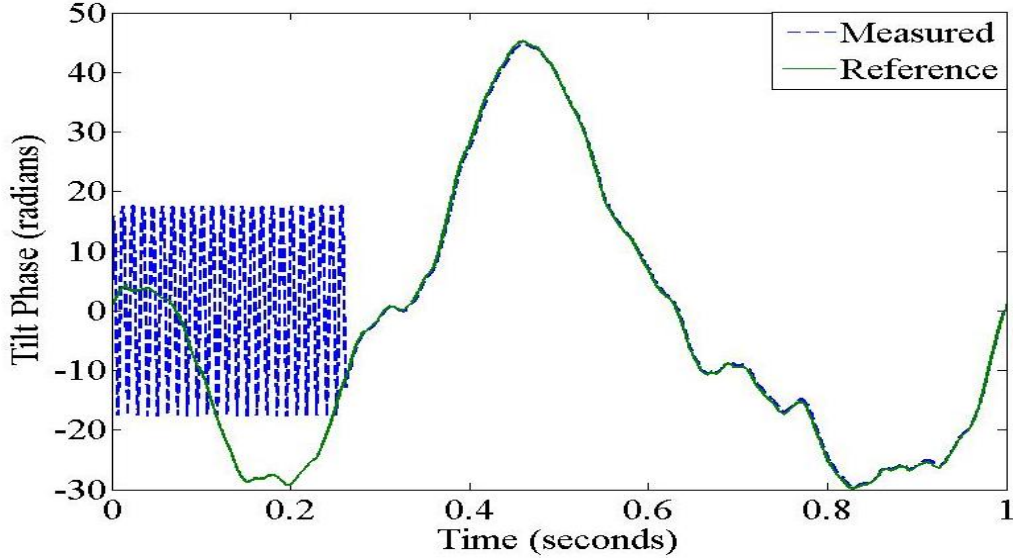


**Figure 57 - Adaptive tilt tracker calibrating for non-optimal  $\alpha$  of 0.10 is shown by the dashed blue curve; after calibration, tracker response tracks aperture tilt phase reference, shown by the solid green curve.**

The performance for the adaptive tracker shown by figure 57 is markedly different; the tracker dithers up to 0.26 seconds to detect the non-optimal  $\alpha$  of 0.10 such that the correct adaptive term is applied. The tilt process is shown to start at zero seconds while the tracker starts to track the process after 0.26 seconds; this is just an artifact of simulation. In reality, it is unknown when a tilt process starts and since the tracker's bandwidth is nearly 4.55 times greater than the tilt process bandwidth, the start time for the process is effectively when the tracker starts to track. The resulting absolute average tracker error,  $|\bar{\theta}| \pm \sigma_{\theta}$ , is  $19.54 \pm 38.53$  nrad, an approximately 750% reduction of the non-adaptive tracker's error deviation. Therefore, the error is well within the diffraction angle zone and denotes the effectiveness of the adaptive tilt tracker for the simulated tilt process. For a  $SNR_p$  value of five, recall that the theoretical best for the residual tracker error deviation is about  $0.25 \lambda/D$  or 35.71 nrad, so the adaptive tilt tracker's performance is realistic. Of



course, one test case for the adaptive tilt tracker does not adequately demonstrate the tracker's effectiveness; therefore, this work first evaluates the adaptive tracker's performance over a range of  $\alpha$  from 0.10 to 0.51; consider figures 58 and 59.

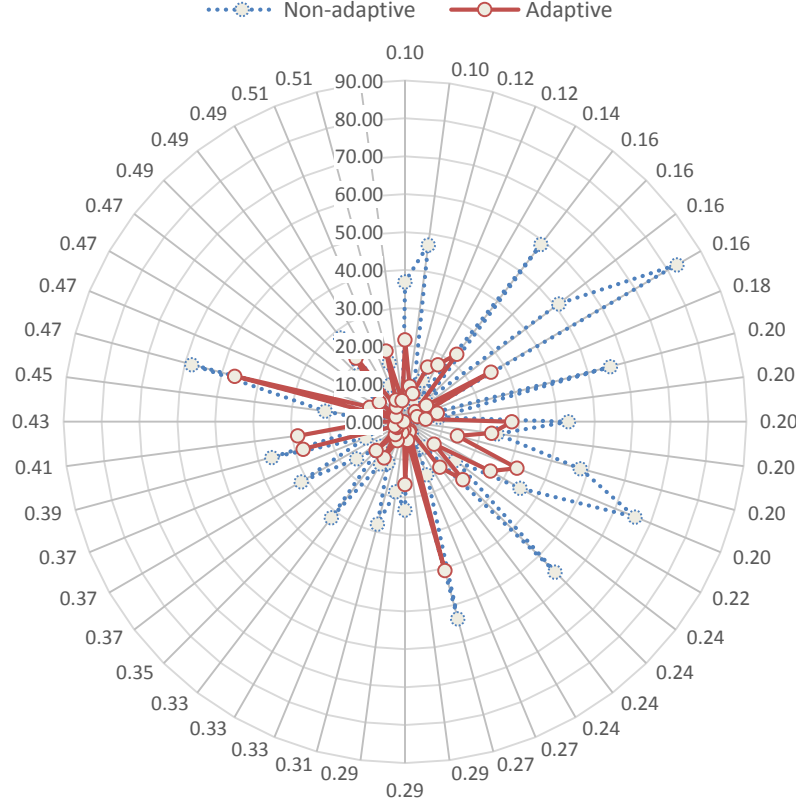


**Figure 58 - Absolute averages,  $|\bar{\theta}|$  (nrad), for residual tracker error are recorded for each randomly drawn,  $\alpha$ . Each dot intersecting a radial for  $\alpha$  indicates a measurement. The solid-red plot represents the adaptive tracker performance; the dashed-blue plot represents the non-adaptive tracker. Both trackers operate at  $f_{max}$ .**

Scenario 1 randomly selects  $\alpha$  over a range from 0.10 to 0.51 to evaluate the non-adaptive and adaptive tracker for the same  $x$  and  $y$  tilt processes. For each random draw of  $\alpha$ , a different  $x$  and  $y$  tilt process is generated for the trackers to track while operating at  $f_{max}$ . Additionally, the tilt processes have two second durations. Therefore, 50 random draws result in a total of 100 independent test cases where the average residual tracker error

is recorded for both trackers. For conciseness, figure 58 only shows the results for  $x$ -tilt processes, the results for  $y$ -tilt processes allow for the same conclusions. Accordingly, the randomly drawn  $\alpha$  is shown around the circumference of the graph where the values are placed in increasing order in the CW direction. The corresponding absolute average value,  $|\bar{\theta}|$  (nrads), for each tracker error measurement is indicated by a dot along the radial line for  $\alpha$ . With the exception of possibly two outlier values, the absolute average values for the adaptive tilt tracker typically lie within the 30 nrad curve of figure 58, while most of the values for the non-adaptive tracker extend beyond the 30 nrad curve up to a maximum of about 85 nrads.

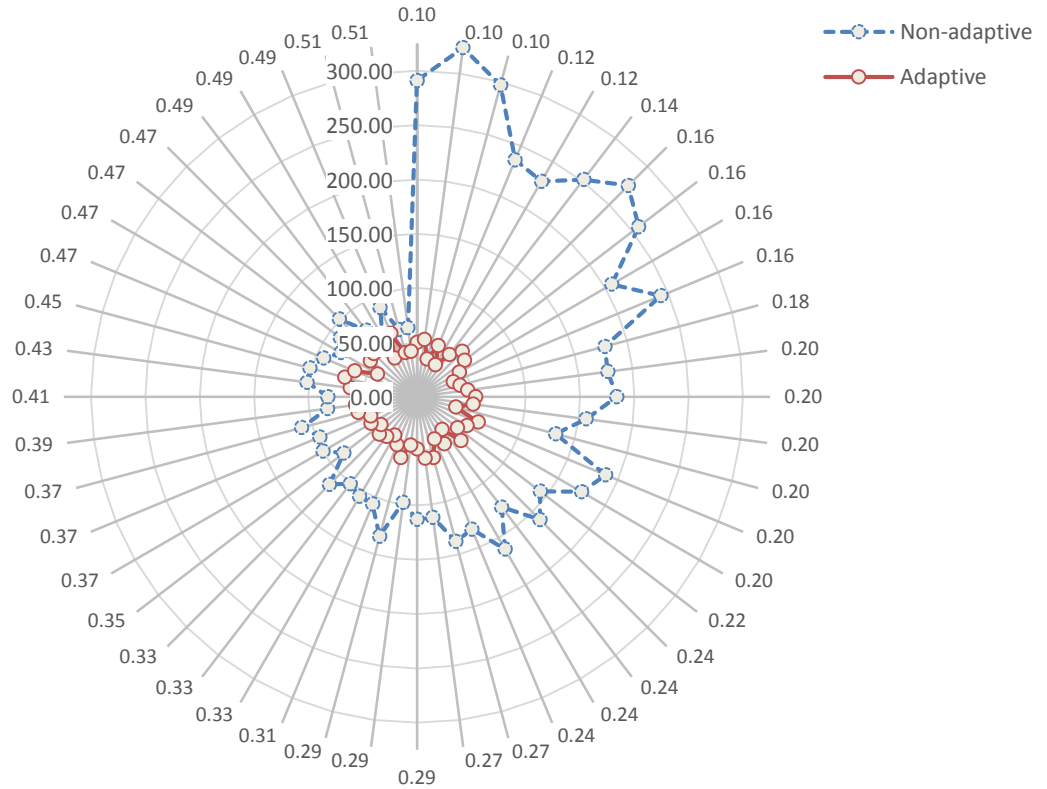


**Figure 59 - Standard deviations,  $\sigma_{\theta}$  (nrads), for residual tracker error are recorded for each randomly drawn,  $\alpha$ . Each dot intersecting a radial for  $\alpha$  indicates a measurement. The solid-red plot represents the adaptive tracker performance; the dashed-blue plot represents the non-adaptive tracker. Both trackers operate at  $f_{max}$ .**

The best indicator for the adaptive tracker's effectiveness is the standard deviation,  $\sigma_\theta$  (nrads), that corresponds to each absolute average value of figure 58. In figure 59, the adaptive tracker clearly outperforms the non-adaptive tracker. Notice how the adaptive tracker effectively cages the standard deviation well within the 100 nrads curve over the range of  $\alpha$ . Contrarily, the non-adaptive tracker's performance is unacceptable for  $\alpha$  ranging from 0.10 to 0.27, where the maximum standard deviation is above 300 nrads. Furthermore, the non-adaptive tracker's performance only becomes acceptable for  $\alpha$  values above 0.27 where the measurements begin to draw closer to the center of the plot.

#### **4.3.2 Scenario 2 ( $\alpha$ less than unity for $f_0$ )**

Scenario 2 carries out the same simulation as Scenario 1 in regards to the  $\alpha$  range, but now the trackers operate at  $f_0$ . Figure 60 shows the absolute average,  $|\bar{\theta}|$  (nrads), results for y-tilt processes. Notably, the adaptive tracker error reports averages comparable to or larger than the non-adaptive tracker. Similar results (not shown) occur for the  $x$ -tilt processes with the adaptive tracker reporting slightly better averages than the non-adaptive version.

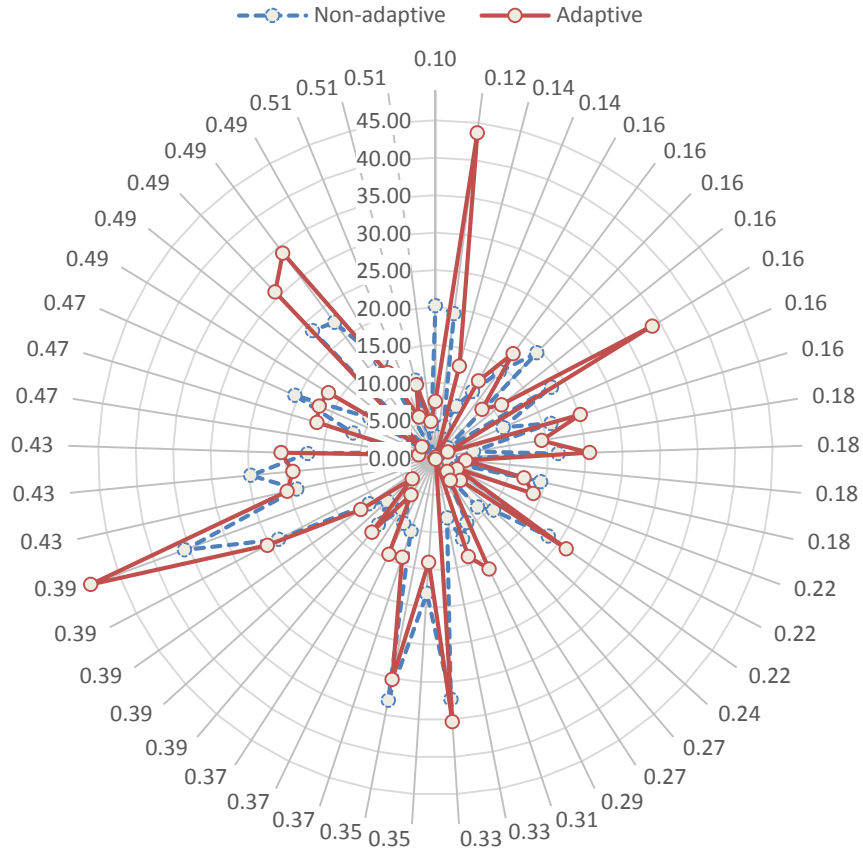


**Figure 60 - Absolute averages,  $|\bar{\theta}|$  (nrads), for residual tracker error are recorded for each randomly drawn  $\alpha$ . Each dot intersecting a radial for  $\alpha$  indicates a measurement. The solid-red plot represents the adaptive tracker performance; the dashed-blue plot represent the non-adaptive tracker. Both trackers operate at  $f_0$ .**

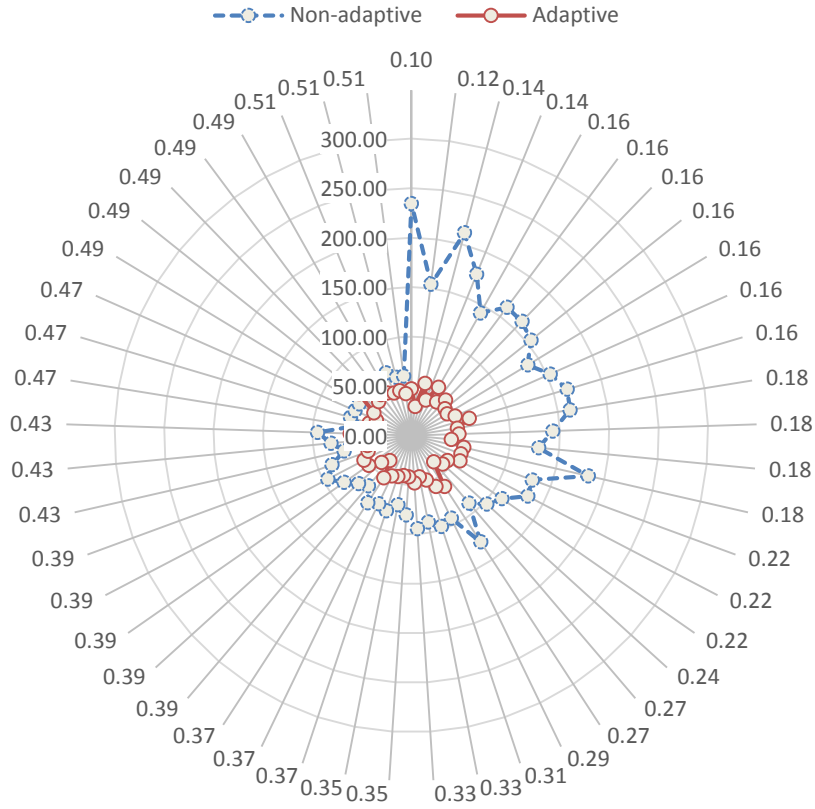


**Figure 61 - Standard deviations,  $\sigma_\theta$  (nrads), for residual tracker error are recorded for each randomly drawn,  $\alpha$ . Each dot intersecting a radial for  $\alpha$  indicates a measurement. The solid-red plot represents the adaptive tracker performance; the dashed-blue plot represents the non-adaptive tracker. Both trackers operate at  $f_0$ .**

Again, the measurements for standard deviation,  $\sigma_\theta$  (nrads), seem to be the best indicator for the adaptive tracker's effectiveness. Figure 61 shows the adaptive tracker caging the standard deviation well within the 100 nrad curve. Without the adaptive feature, the tracker is shown to be unreliable over the  $\alpha$  range from 0.10 to 0.18 for  $y$ -tilt and from 0.10 to 0.27 for  $x$ -tilt. Comparing the results for Scenarios 1 and 2 suggests the adaptive tracker is effective in adapting to non-optimal  $\alpha$  values ranging about 0.10 to 0.51. Additionally, operating the adaptive tracker at  $f_0$  as opposed to  $f_{max}$  showed no significant difference in tracker performance. Contrarily, the non-adaptive tracker seemed to perform

better in Scenario 2 with smaller absolute averages and a smaller  $\alpha$  range where standard deviation was unacceptable for y-tilt. However, the noted differences are mainly attributed to the different tilt processes encountered in Scenario 1 as opposed to Scenario 2 and shows that tracker performance depends on tilt process characteristics.

### 4.3.3 Scenario 3 ( $\alpha$ greater than unity)

Figures 62 and 63 allow for a comparison of the non-adaptive and adaptive trackers when  $\alpha$  is 1.61 and frame rate is  $f_{max}$ . The non-adaptive tracker response shows a steadily increasing oscillation about the reference  $x$ -tilt phase process as time elapses.

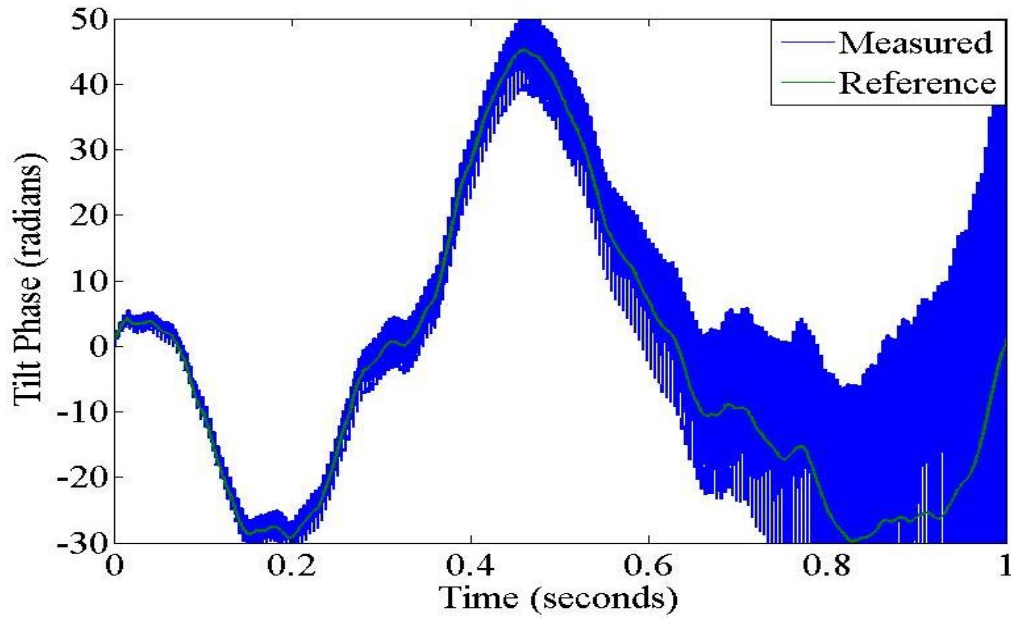


**Figure 62 - Non-adaptive tilt tracker operating with  $\alpha$  equal to 1.61 shows a response that has steadily increasing oscillations about the aperture tilt phase reference.**

The non-adaptive tracker response is unexpected for an  $\alpha$  of 1.61; recall from figure 51 that the tracker's step response experiences notable oscillations when  $\alpha$  approaches a value of about three. From figure 52, increasing total delay time from  $150 \mu s$  to  $298.75 \mu s$

reduced the margin that  $\alpha$  can increase above unity before the step response experienced notable oscillations and eventual instability. Therefore, the author can only posit that other functions and processes for the tracker model induce additional delay to reduce the expected  $\alpha$  margin. Also, the step response for an  $\alpha$  of 1.61 experiences a 11% overshoot; this may be more of a contributing factor to the oscillations for the tilt process input as opposed to the unit step input. Therefore, the non-adaptive tracker yields an unacceptable performance with an absolute average error,  $|\bar{\theta}| \pm \sigma_{\theta}$ , of  $15.39 \pm 3333.9$  nrad. The adaptive tilt tracker reports an absolute average error of  $20.33 \pm 51.14$  nrad, an approximately 6500% reduction of the non-adaptive tracker's error deviation.

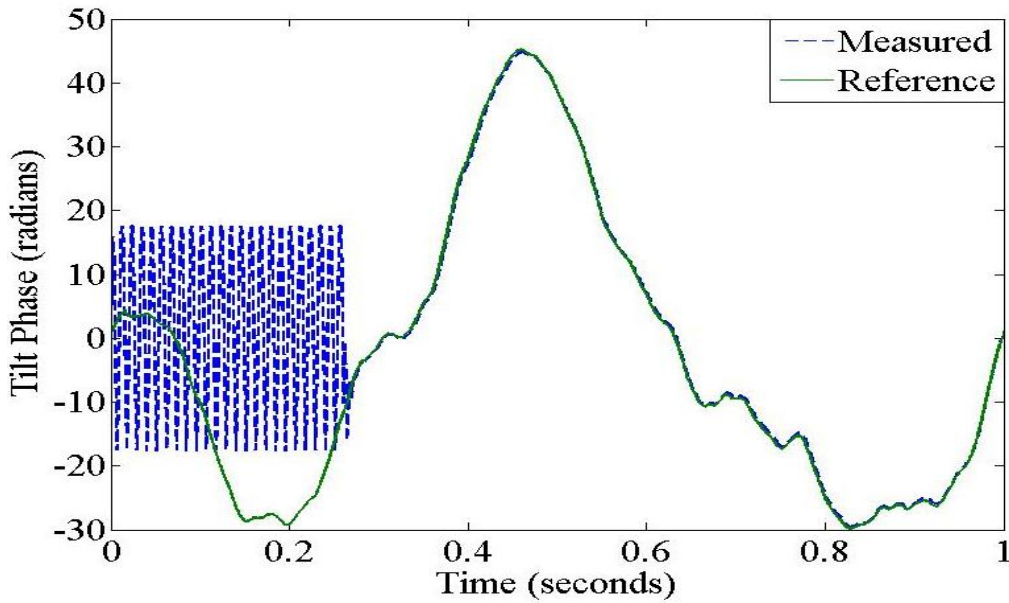


**Figure 63 - Adaptive tilt tracker calibrating for non-optimal  $\alpha$  of 1.61 is shown by the dashed blue curve; after calibration, tracker response tracks aperture tilt phase reference, shown by the solid green curve.**

Recall that an increasing  $\alpha$  above unity may amplify tracker noise disturbances. To show the non-adaptive tracker's behavior in the presence of band limited white noise (BLWN), this work simulates tilt measurement noise with a root mean square (rms) value of about 0.50 nrad. Figure 64 shows that when the non-adaptive tracker operates at  $f_{max}$  with an  $\alpha$  of 1.53, the subsequent increase in bandwidth couples higher frequency noise components into the tracker's response. This results in a greater deviation for the absolute average tracker error,  $|\bar{\theta}| \pm \sigma_{\theta}$ , of  $19.08 \pm 248.42$  nrad. In figure 65, the adaptive tracker appropriately compensates for the non-optimal  $\alpha$  of 1.53 such that the tracker operates at the desired bandwidth of 200 Hz; this is apparent in the reduced noise envelope and an absolute average tracker error of  $23.11 \pm 101.31$  nrad.

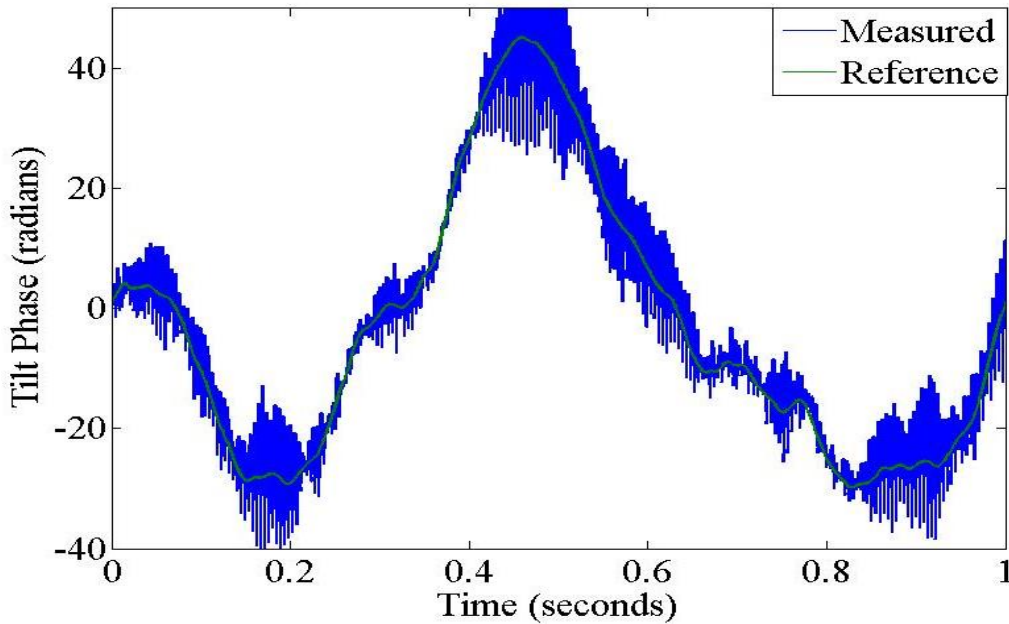


**Figure 64 - Non-adaptive tilt tracker operating with  $\alpha$  equal to 1.53 in the presence of band limited white noise; response shows an amplification for the noise envelope about the aperture tilt phase reference.**



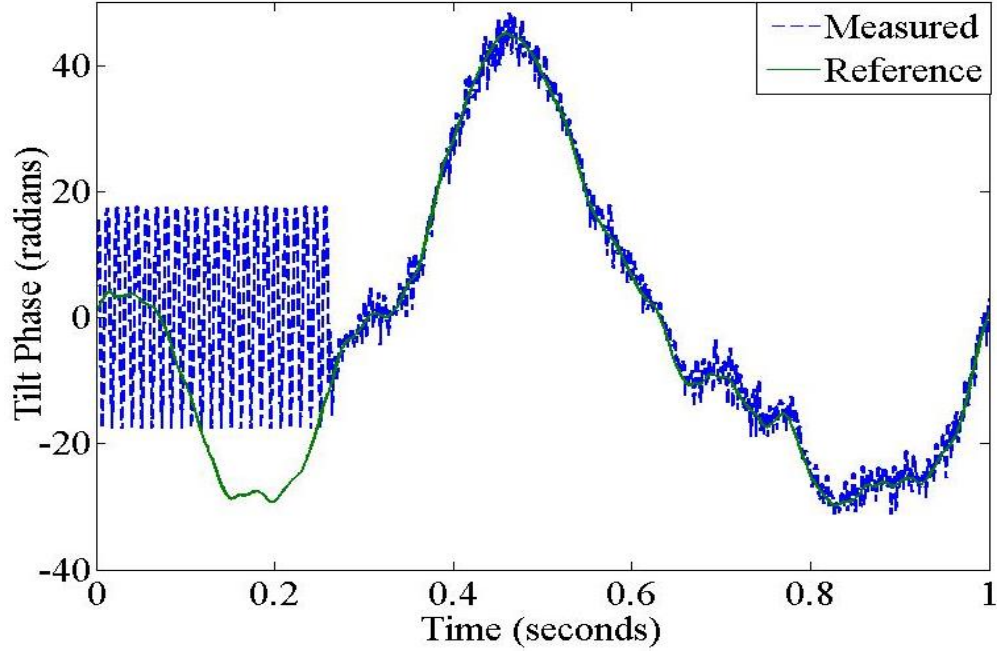


**Figure 65 - Adaptive tilt tracker calibrating for non-optimal  $\alpha$  of 1.53 in the presence of band limited white noise; after calibration, the dashed blue curve tracks aperture tilt phase reference with a reduced noise envelope.**

The previous demonstrations showed the potential effectiveness of the adaptive tilt tracker for non-optimal  $\alpha$  values greater than unity. This scenario continues to evaluate both non-adaptive and adaptive trackers over a range of  $\alpha$  values, now from 0.51 to 1.82. As with Scenarios 1 and 2, 50 random draws for  $\alpha$  result in a total of 100 independent test cases where the absolute average residual tracker error,  $|\bar{\theta}| \pm \sigma_{\theta}$ , is recorded for both trackers. Since the absolute averages,  $|\bar{\theta}|$ , were comparable for both trackers during this scenario, only the standard deviation measurements are shown for conciseness.

Figure 66 shows the standard deviation results for the y-tilt processes while the trackers are operating at  $f_{max}$ . Notably, both trackers perform virtually identically over the range of  $\alpha$  from 0.53 to about 1.57. The standard deviation, in nanoradians, is scaled

according to the base ten logarithm; therefore, the non-adaptive tracker cages the standard deviation well within 100 nrad up to an  $\alpha$  of 1.57.

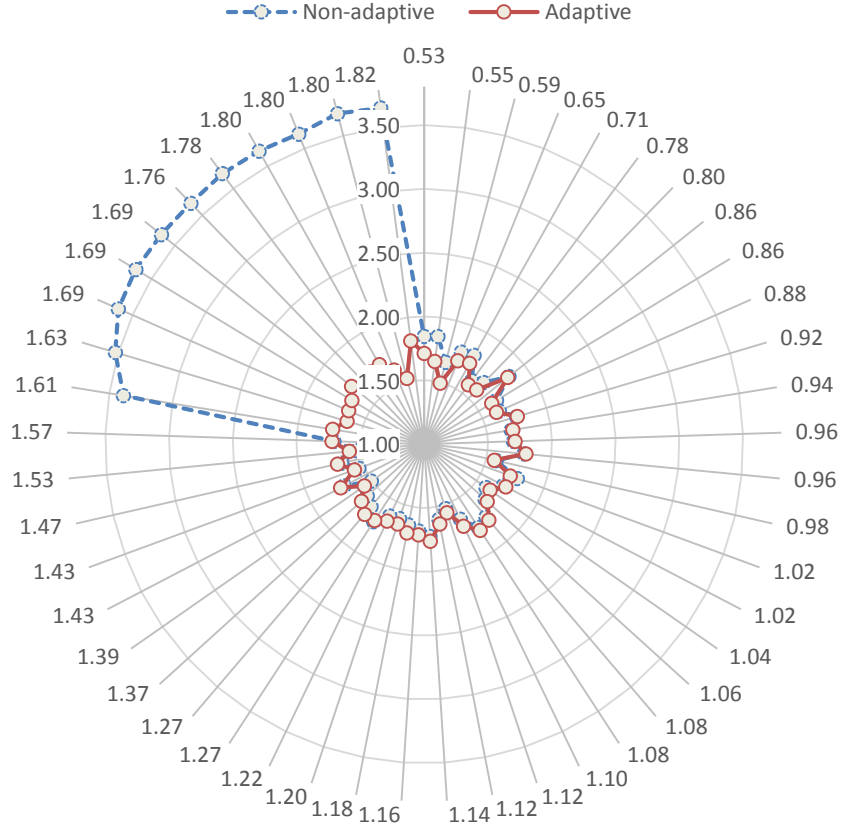


**Figure 66 - Standard deviations,  $\sigma_\theta$  (nrads), for residual tracker error are recorded ( $\log_{10}$  scale) for each randomly drawn,  $\alpha$ . Each dot intersecting a radial for  $\alpha$  indicates a measurement. The solid-red plot represents the adaptive tracker performance; the dashed-blue plot represents the non-adaptive tracker. Both trackers operate at  $f_{max}$ .**

The sharp increase in standard deviation at an  $\alpha$  of 1.61 indicates when the non-adaptive tracker becomes unstable. This work terms the special value for  $\alpha$  when instability occurs as  $\alpha_{critical}$ . Notice the adaptive feature prevents the tracker from reaching  $\alpha_{critical}$  to maintain a standard deviation well within 100 nrad for the entire range of  $\alpha$ . The results for the  $x$ -tilt processes allow for the same conclusions.

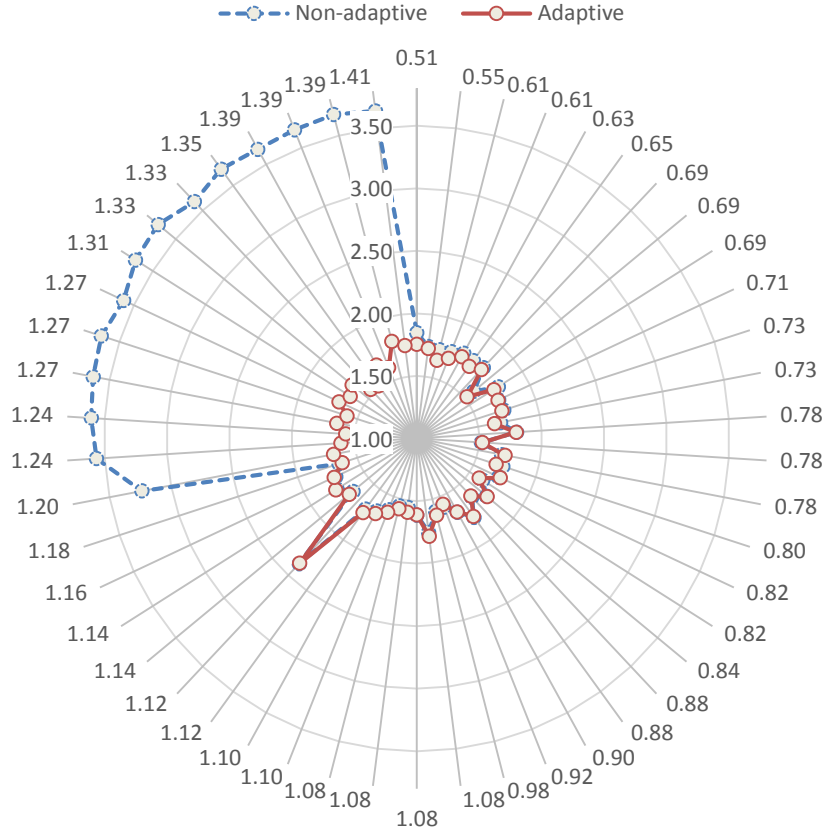


**Figure 67 - Standard deviations,  $\sigma_\theta$  (nrads), for residual tracker error are recorded ( $\log_{10}$  scale) for each randomly drawn,  $\alpha$ . Each dot intersecting a radial for  $\alpha$  indicates a measurement. The solid-red plot represents the adaptive tracker performance; the dashed-blue plot represents the non-adaptive tracker. Both trackers operate at  $f_0$ .**

Consider figure 67 where the trackers now operate at  $f_0$  and the corresponding standard deviation measurements for  $x$ -tilt processes are presented. Again, the trackers perform virtually identically for an  $\alpha$  range where the standard deviation is caged well within the 100 nrad curve, with the exception of a possible outlier measurement for an  $\alpha$  value of 1.12. However, notice the  $\alpha_{critical}$  value is now about 1.20. This confirms previous observations that operating at  $f_0$  as opposed to  $f_{max}$  induces additional loop delay. In figure 67, the increase in loop delay shows as a reduction in the  $\alpha$  margin such that the tracker becomes unstable for smaller increases in  $\alpha$  above unity; the margin reduction is

about 25.5%. Again, the adaptive tracker indicates its effectiveness over the entire range of  $\alpha$  (not including the outlier measurement). The y-tilt processes allow for the same conclusions. Additionally, notice from all scenarios presented up to this point, that the non-adaptive and adaptive trackers perform relatively the same when  $\alpha$  ranges from about 0.51 to  $\alpha_{critical}$ . This suggests the non-adaptive tracker can tolerate moderate deviations from  $K_{g_{opt}}$  and still maintain acceptable performance.

#### **4.3.4 Scenario 4 (Desired Tracker Features)**

##### **4.3.4.1 Recalibration**

Scenario 4 demonstrates two desired adaptive tracker capabilities. The first one involves the adaptive tilt tracker having an ability to recalibrate after an initial calibration. This is necessary because the imaged object characteristics are so dynamic that a change for the detector's intensity spot, after the initial calibration, is highly likely. As discussed, a change for the detector spot results in a change for  $K_{g_x}$  and  $K_{g_y}$ ; the adaptive tracker must sense when the change results in an average tilt angle error that deviates beyond the diffraction angle zone.

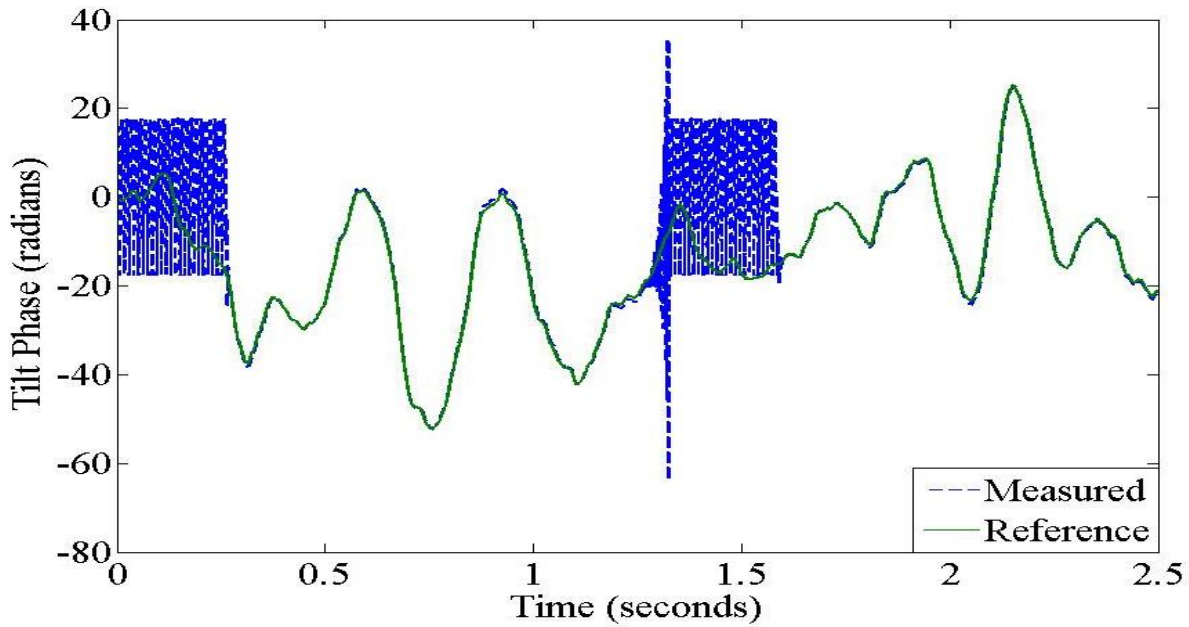


Figure 68 - Adaptive tilt tracker response shown by the dashed blue curve performs an initial calibration; the tracker deviates from the reference, shown by the solid green curve, when a non-optimal  $\alpha$  of 2.45 is introduced at 1.26 seconds; tracker recalibrates at 1.33 seconds to track aperture tilt phase reference accurately.

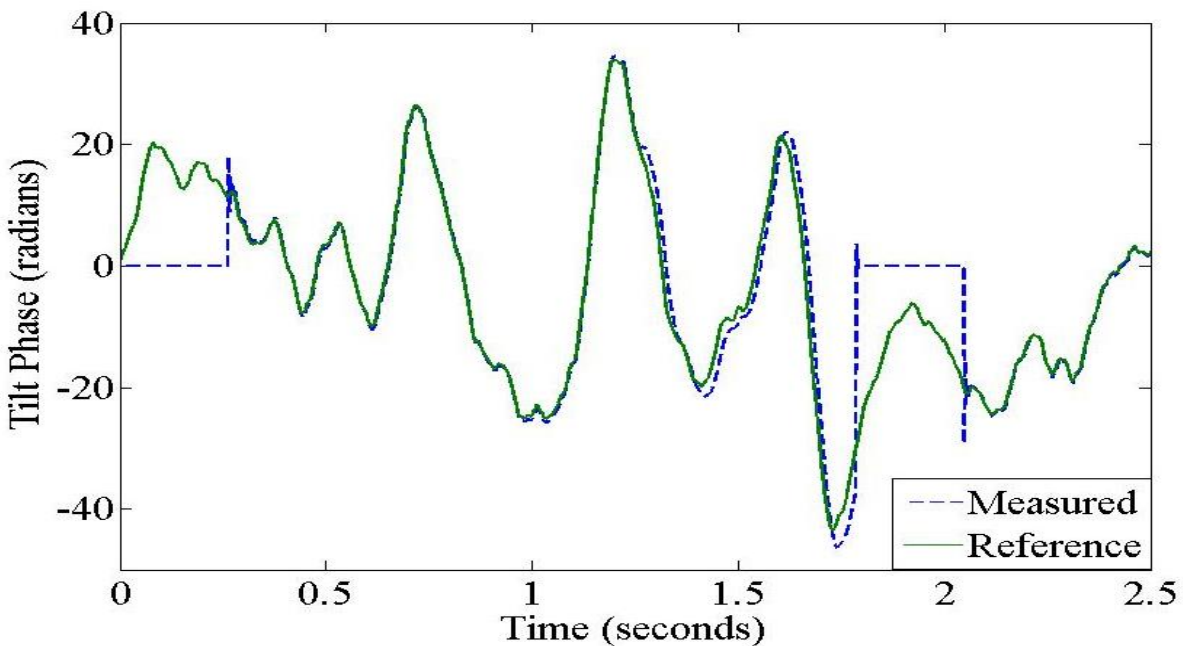


Figure 69 - Adaptive tilt tracker response for y-axis shown by the dashed blue curve; after initial calibration and recalibration using the x-axis only, the tracker accurately tracks the aperture y-tilt phase reference, shown by solid green curve.

Figure 68 shows the adaptive tracker performing an initial calibration, then tracking the reference  $x$ -tilt process accurately. The simulation introduces a non-optimal  $\alpha$  of 2.45 at about 1.2605 seconds to simulate a change in spot characteristics. By measuring an absolute average  $x$ -tilt angle error,  $|\bar{\theta}| \pm \sigma_{\theta}$ , of  $0.865 \pm 159.14$  nrad at 1.33 seconds, the tracker recalibrates to track the aperture  $x$ -tilt phase process accurately. Either tracker response ( $x$  or  $y$ ) can trigger a recalibration; for the simulation shown above, the  $x$ -response first deviated out of tolerance to trigger a recalibration at 1.33 seconds.

Figure 69 shows a recalibration following the initial calibration for a  $y$ -tilt process. Furthermore, the figure shows the behavior of the tracker's  $y$ -response while the tracker's  $x$ -response is dithering to calibrate the tracker. During calibration, the  $y$ -response is held constant at zero tilt angle during the dithering process. The simulation for figure 69 introduces a non-optimal  $\alpha$  of 0.10 at about 1.2605 seconds; this causes the tracker's  $x$  and  $y$  responses to deviate from the reference aperture tilt phase processes. The  $y$ -response first deviates out of tolerance to trigger a recalibration at about 1.78 seconds, where the absolute average  $y$ -tilt angle error,  $|\bar{\theta}| \pm \sigma_{\theta}$ , is  $3.91 \pm 156.09$  nrad. After recalibration, the tracker tracks the aperture tilt processes accurately. As previously stated, the optical system's diffraction angle is the threshold used for simulations to assess when the tracker's responses deviate out of tolerance. The chosen threshold is a design decision and a smaller or larger threshold, in reference to the diffraction angle, correspondingly makes the tracker more or less sensitive in triggering a recalibration.

#### 4.3.4.2 Averaging PTS output signals

The second desired adaptive tracker capability concerns averaging the PTS's output signals. Since the PTS operates over a range of frame rates from about 2.52 to 10.0 kfps while the tracker only compensates for tilt up to 200 Hz, the PTS may sample a particular tilt instance multiple times. Of course, this is taking the effective tilt distortion to be constant over the maximum compensation cycle of 200 Hz, which was shown to be valid from Section 4.2. The multiple samples may be averaged to reduce measurement disturbances from band limited white noise (BLWN).

A measurement for the  $i_{th}$  tilt instance of a tilt process at time,  $t$ , is represented as

$$\widetilde{W}_i(t) = \widehat{W}_i + n(t), \quad (4.4)$$

where the corrupted tilt measurement,  $\widetilde{W}_i(t)$ , is expressed as a summation of independent contributions, the noiseless tilt measurement,  $\widehat{W}_i$ , and the noise disturbance,  $n(t)$ . Given that  $n(t)$  is sampled from a BLWN population that has an expectation near zero and variance,  $\sigma_n^2$ , the distribution for a measured set of  $n(t)$  is derived as follows,

$$E[\widetilde{W}_i(t_k)_{k=1}^n] = E[(\widehat{W}_i)_{k=1}^n] + E[n(t_k)_{k=1}^n] \quad (4.5)$$

$$E[(\widehat{W}_i)_{k=1}^n] = \widehat{W}_i, \quad (4.6)$$

where ' $n$ ' samples of a particular tilt instance are  $\widetilde{W}_i(t_k)_{k=1}^n$  and the expectation of the samples is expressed as a summation of expectations for the noiseless tilt samples,  $(\widehat{W}_i)_{k=1}^n$ , and noise samples,  $n(t_k)_{k=1}^n$ . The expectation for noise samples is a random variable. Therefore, confidence levels and intervals are used to assign a probability that the expectation is confined within a specified range [23],

$$\begin{aligned} E[\widetilde{W}_l(t_k)_{k=1}^n] - z_{\alpha/2} \left( \frac{\sigma_n}{\sqrt{n}} \right) < \widetilde{W}_l < E[\widetilde{W}_l(t_k)_{k=1}^n] + z_{\alpha/2} \left( \frac{\sigma_n}{\sqrt{n}} \right) \xrightarrow{\text{yields}} \\ - z_{\alpha/2} \left( \frac{\sigma_n}{\sqrt{n}} \right) < E[n(t_k)_{k=1}^n] < + z_{\alpha/2} \left( \frac{\sigma_n}{\sqrt{n}} \right) \end{aligned} \quad (4.7)$$

Applying the definition for confidence levels and intervals to  $\widetilde{W}_l(t_k)_{k=1}^n$  results in an expression that bounds the expectation for noise samples, as desired. For a given tracker system,  $\sigma_n^2$  can be determined. Additionally, the z-score ( $z_{\alpha/2}$ ), a parameter that defines desired confidence levels, is a design preference; therefore, the bounds for the expectation of equation (4.7) become only a function of sample size, ' $n$ '. While operating under the assumption that  $\sigma_n^2$  is known, the sample standard deviation is

$$\sigma_n / \sqrt{n}, \quad (4.8)$$

where it also becomes only a function of sample size for known  $\sigma_n$  [23]. Taking a great many samples drives the sample mean and standard deviation towards zero, the desired effect being a reduction of noise disturbance for a given tilt instance. Realistically, the number of samples is determined by sensor frame rate,  $f_s$ , total loop delay,  $\bar{\tau}$ , and tracker bandwidth,  $f_{3dB}$ , as follows,

$$n = \frac{f_s}{f_{3dB}} \left( 1 - \frac{\bar{\tau}}{\tau_{3dB}} \right) \approx \frac{f_s}{f_{3dB}} \quad \text{for} \quad \frac{\bar{\tau}}{\tau_{3dB}} \ll 1, \quad (4.9)$$

where equation (4.9) assumes that  $f_{3dB}$  is at least equal to  $4f_{T_G}$ . The total loop delay,  $\bar{\tau}$ , for equation (4.9) now accounts for delays due to the PTS's sampling, processing, and averaging operations. For simulations conducted in this research,  $\bar{\tau}$  is much less than  $\tau_{3dB}$ , the reciprocal of  $f_{3dB}$ . Therefore, the approximation for equation (4.9) is applicable. To investigate the possible benefits of averaging the PTS's outputs, this work conducted a



scenario similar to Scenario 3 where  $\alpha$  varies upward from 0.51, but now in the presence of BLWN.

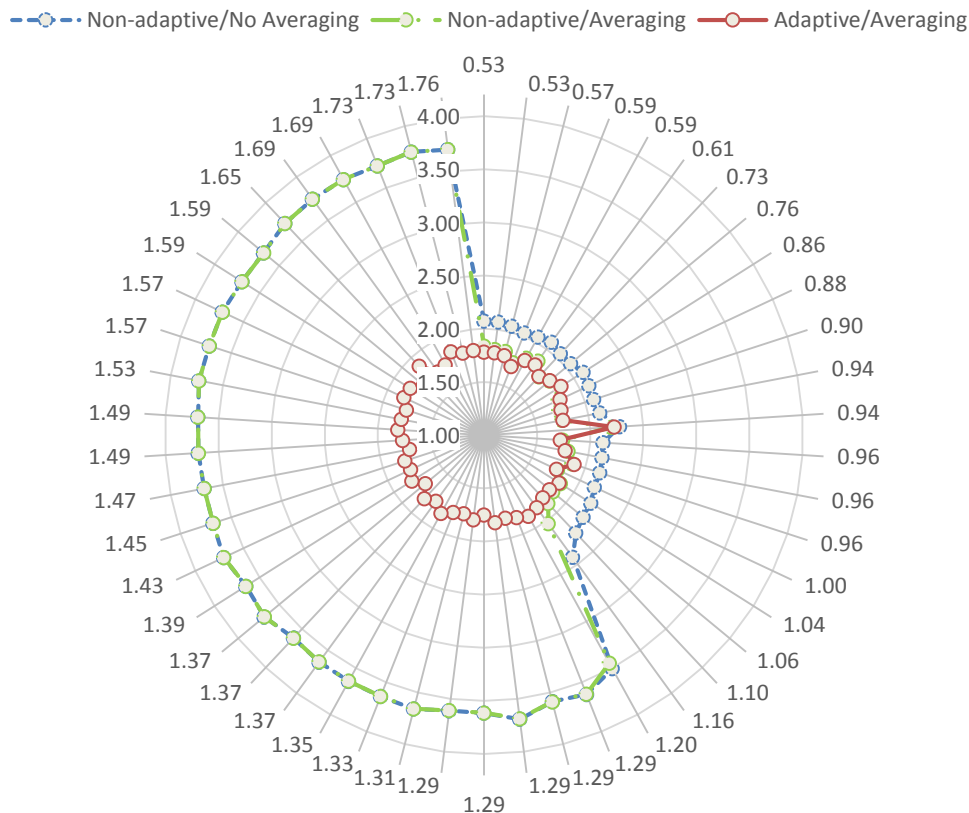


**Figure 70 - Standard deviations,  $\sigma_\theta$  (nrads), for residual tracker error are recorded ( $\log_{10}$  scale) for each randomly drawn,  $\alpha$ . Each dot intersecting a radial for  $\alpha$  indicates a measurement. The solid-red plot represents the adaptive/averaging tracker performance; the dashed-dotted green plot represents the non-adaptive/averaging tracker; the dashed-blue plot represents the non-adaptive/non-averaging tracker. All trackers operate at  $f_0$ .**

Operating the trackers at  $f_0$  theoretically yields about 12 samples per  $f_{3dB}$ ; however, the averaging function for the simulated trackers can only run at multiples of the *G-tilt* filter Nyquist sampling interval of 0.5 milliseconds. Consequently, figure 70 shows the results for three versions of trackers taking ten samples per  $f_{3dB}$ : non-adaptive/non-averaging; non-adaptive/averaging; averaging/adaptive. The trackers are evaluated over

an  $\alpha$  range from 0.51 to 1.76. Over the  $\alpha$  range (0.53 to 1.16), the effect of averaging the PTS's outputs is clearly evident. The non-adaptive/non-averaging tracker (blue-dashed plot) reports standard deviations,  $\sigma_\theta$  (nrads), outside of the 100 nrads curve while the averaging trackers report an average standard deviation of about 63 nrads. The adaptive/averaging tracker is readily identifiable as it effectively cages the standard deviations to about 63 nrads for the entire range of  $\alpha$ . Also notable, is that once the non-adaptive trackers reach the  $\alpha_{critical}$  value of about 1.20, averaging the PTS's outputs makes no difference on tracker performance, as expected.

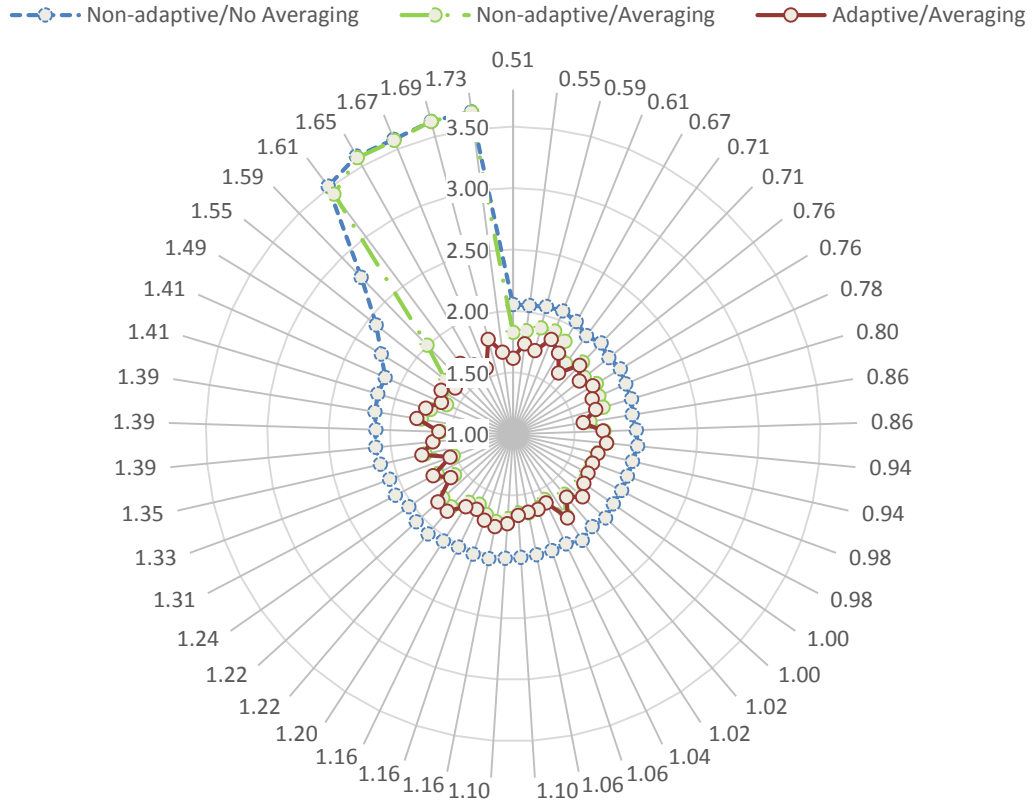


**Figure 71 - Standard deviations,  $\sigma_\theta$  (nrads), for residual tracker error are recorded ( $\log_{10}$  scale) for each randomly drawn,  $\alpha$ . Each dot intersecting a radial for  $\alpha$  indicates a measurement. The solid-red plot represents the adaptive/averaging tracker performance; the dashed-dotted green plot represents the non-adaptive/averaging tracker; the dashed-blue plot represents the non-adaptive/non-averaging tracker. All trackers operate at  $f_{max}$ .**

Operating the trackers at  $f_{max}$  theoretically yields about 50 samples per  $f_{3dB}$ ; the simulations were able to take 50 samples since the averaging function ran at a multiple 0.5 milliseconds for  $f_{max}$ . From figure 71, the same observations for the three versions of trackers can be made as before from figure 70. The difference, however, is that the average standard deviation envelopes for the averaging trackers have diminished down from 63 nrads to about 50 nrads, an approximately 21% decrease. Also notable, is the  $\alpha_{critical}$  value is now about 1.61 to give a greater  $\alpha$  margin where the non-adaptive trackers are stable. The simulations resulted in 200 independent test cases, of which 100 are shown by figures 69 and 70, that suggest the benefits of averaging the PTS's outputs to reduce BLWN effects. However, the results have to be tempered with the realities of physical systems employing low pass filtering that make the BLWN approximation less valid. Also, the delay induced by the averaging operation may be intolerable to the dynamics of some tracker systems.

#### 4.3.5 Summary of Scenario Results

Table 10 summarizes the results for scenario simulations. The first column indicates the particular scenario and operating frame rate for the trackers. The second column corresponds to the average or expectation,  $E[|\bar{\theta}|]$  (nrads), and associated standard deviation, taken over one-hundred absolute averages,  $|\bar{\theta}|$ . Similarly, the third column presents the corresponding average,  $\overline{\sigma_{\theta}}$  (nrads), and associated standard deviation for one-hundred standard deviations,  $\sigma_{\theta}$ . The final column shows the maximum and minimum long exposure Strehl ratios attained over the range of tracker error values.

**Table 10. Summary of Results for Simulated Trackers**

Scenario	$E[ \bar{\theta} ]$ (nrads)	$\bar{\sigma}_{\theta}$ (nrads)	Max/Min $SR_{LE}$
	Non-adaptive	Non-adaptive	Non-adaptive
	Adaptive	Adaptive	Adaptive
<b>1</b> <sub>(<math>f_{max}</math>)</sub>	28.94±26.93	146.15±72.73	0.4769/0.0643
	12.91±10.56	49.58±9.66	0.7436/0.4313
<b>2</b> <sub>(<math>f_0</math>)</sub>	13.26±8.82	108.37±45.28	0.5322/0.1438
	14.27±9.81	49.70±14.46	0.7670/ 0.3999
<b>3</b> <sub>(<math>f_{max}</math>)</sub>	12.41±9.75	134.90±6.46	0.2319/ 0.1625
	13.37±10.84	50.12±1.32	0.6632/0.4755
<b>3</b> <sub>(<math>f_0</math>)</sub>	10.64±7.87	177.83±7.24	0.1472/0.1112
	11.76±8.77	50.12±1.32	0.6592/0.5004
Scenario	Non-adaptive/Non-averaging	Non-adaptive/Non-averaging	Non-adaptive/Non-averaging
	Non-adaptive/Averaging	Non-adaptive/Averaging	Non-adaptive/Averaging
	Adaptive/Averaging	Adaptive/Averaging	Adaptive/Averaging
<b>4</b> <sub>(<math>f_{max}</math>)</sub>	12.62±9.97	165.96±3.02	0.1591/0.1238
	12.32±9.90	81.28±3.80	0.4483/0.3106
	14.20±10.61	50.12±1.20	0.6529/0.4723
<b>4</b> <sub>(<math>f_0</math>)</sub>	16.41±12.83	1071.50±5.75	0.0045/0.0042
	16.05±12.51	794.33±8.13	0.0082/0.0075
	13.93±9.58	64.57±1.29	0.5314/0.3938

Before discussing specific tracker results of table 10, it is important to set a reference for tracker performance assessment. Accordingly, for a  $SNR_v$  value of five, the theoretical best for tracker error standard deviation and corresponding Strehl ratio are about 35.71 nrads and 0.8027, respectively. The non-adaptive and adaptive trackers report comparative

absolute average error values,  $|\bar{\theta}|$ , as shown by the values for column two of table 10. The results for the adaptive tracker seem questionable because the tracker reports lower  $E[|\bar{\theta}|]$  values than the non-adaptive version only for scenarios  $1_{(f_{max})}$  and  $4_{(f_0)}$ .

Although the  $E[|\bar{\theta}|]$  values for both trackers are comparable for scenario  $2_{(f_0)}$ , the author expected the adaptive tracker to report smaller absolute averages,  $|\bar{\theta}|$ , than the non-adaptive tracker. Recall from figure 56 that when  $\alpha$  trends downward from 0.51, as in scenarios  $1_{(f_{max})}$  and  $2_{(f_0)}$ , the non-adaptive response may lag the reference to create larger  $|\bar{\theta}|$  values. This non-adaptive tracker behavior is supported by the  $E[|\bar{\theta}|]$  results for scenario  $1_{(f_{max})}$ . When the trackers switch to a frame rate of  $f_0$ , the resultant  $E[|\bar{\theta}|]$  values are unexpected because they imply that the non-adaptive tracker outperforms the adaptive tracker for scenario  $2_{(f_0)}$ . The author believes the implication is misleading because tilt process characteristics can create a condition where  $|\bar{\theta}|$  values for the non-adaptive tracker become comparable to and even less than the  $|\bar{\theta}|$  values for the adaptive tracker. This is supported by simulation data for scenario  $2_{(f_0)}$  that show both trackers reporting comparable  $|\bar{\theta}|$  values for the  $x$ -tilt processes, but for  $y$ -tilt processes, the adaptive tracker reports larger  $|\bar{\theta}|$  values than the non-adaptive version. For scenarios  $3_{(f_{max})}$  thru  $4_{(f_{max})}$ , the non-adaptive and adaptive trackers report similar values for  $E[|\bar{\theta}|]$ ; the author expects this because  $\alpha$  ranges upward from 0.51 where both trackers report similar  $|\bar{\theta}|$  values. However, the  $E[|\bar{\theta}|]$  values for the adaptive tracker exceed those of the non-adaptive version on average by 1.24 (mean) and 0.92 (standard deviation). This possible

discrepancy may be attributed to a difference in tracker error sample size that existed for the simulated non-adaptive and adaptive trackers.

Therefore, the best discriminator for tracker performance is the variability of the average tracker error or the standard deviation,  $\sigma_\theta$ , and corresponding Strehl ratio. Over all scenarios, the adaptive tracker is shown to outperform the non-adaptive versions. Recall that scenarios one thru three are without BLWN. A cursory look at the data may suggest that the adaptive tracker performed best during scenarios one and two where  $\alpha$  ranged from 0.10 to 0.51, because greater max  $SR_{LE}$  values occurred during the first two scenarios. However, notice for scenario three where  $\alpha$  ranges from 0.51 to 1.82, the adaptive tracker is more consistent as the max and min  $SR_{LE}$  values differ up to 28.3% as opposed to 47.9% for the first two scenarios. Furthermore, the max  $SR_{LE}$  for scenario three is respectable with a value that is about 83% of the theoretical max. Many more test cases than 200 (for each  $\alpha$  range) would need to be run before definitively concluding the adaptive tracker typically performs best over an  $\alpha$  range (0.51 to 1.82), rather than (0.10 to 0.51). Scenario two indicates the largest variability in  $\overline{\sigma_\theta}$  for the adaptive tracker; this is because two outlier standard deviation values of 132.90 and 138.00 nrad induce a larger variance in the average standard deviation. Without the outlier values, the average standard deviation,  $\overline{\sigma_\theta}$ , and associated standard deviation is  $47.94 \pm 7.54$  nrad; the corresponding maximum  $SR_{LE}$  becomes 0.7205. Also notable for scenarios one thru three is that operating the adaptive tracker at  $f_0$  as opposed to  $f_{max}$  does not appreciably affect the tracker's performance for the simulated test cases.

Recall that scenario four involves BLWN where the benefit of averaging the PTS's outputs is made evident by the results of table 10. The adaptive/averaging tracker that

operates at  $f_{max}$  actually reports average standard deviation and  $SR_{LE}$  values comparable to scenario three results. The deleterious effect of BLWN is especially evident for waning signal levels. While operating at  $f_0$ , the adaptive/averaging tracker reports consistent performance; however, its maximum  $SR_{LE}$  is about 66.2% of the theoretical maximum. This work simulated a conservative BLWN power; with larger noise power contributions, the performance for the adaptive/averaging tracker would show an even larger degradation.

The expectation for absolute average tracker error,  $E[E|\bar{\theta}] \pm \overline{\sigma_{\theta}}$ , over all scenarios for the adaptive tracker is about  $(13.41 \pm 10.83) \pm (52.08 \pm 3.72)$  nrad; this means the tracker attenuates the aperture's one-axis, one-sigma *G-tilt* angle deviation up to 97.76%. Corresponding averages for max and min  $SR_{LE}$  are about 0.67 and 0.45, a respective 116% and 246% improvement over the non-adaptive tracker. To put the  $SR_{LE}$  values into perspective, the SOR's Laser Guidestar II AO system that was developed in 2010, reported a typical overall *SR* of 0.33 where the system had a limiting *V-mag* range of (10 to 12) [20].

Finally, the author chose to evaluate the trackers at only the threshold  $SNR_v$  value of five because the signal level for a dim LEO object will typically cause the tracker to operate near  $SNR_{v_0}$ . Therefore, it is more important to characterize the adaptive tracker's performance for its minimum desired operating signal level. For higher signal levels, greater than a  $SNR_v$  value of ten, the tracker's performance will approach 31.43 nrad and 0.8400 for respective error standard deviation and corresponding  $SR_{LE}$ .

## **V. Conclusions and Future Considerations**

### **Chapter Overview**

The development of an adaptive tilt tracker that utilizes a QUAD-cell detector to measure tilt distortion of LEO objects is a complex problem with many complicating factors. Particularly, LEO object characteristics such as size, motion, shape, and intensity distribution, present a daunting set of challenges that may cause the QUAD-cell and tilt tracker performances to deviate substantially from optimal. This research proved successful by first thoroughly defining the problem to identify the realm of constraints; notably, the QUAD-cell is inherently unreliable for resolvable LEO objects that have asymmetrical characteristics. With a solid problem definition, this work developed a methodology that rotates the LEO object image. This greatly simplifies the LEO object characteristics where the image rotation transforms an unpredictable and unfavorable spot intensity distribution to a more suitable one for the QUAD-cell. Using the rotated image, an adaptive gain term is developed that compensates for intensity spots sizes that deviate from optimal. This research employs the dither method that oscillates the fast steering mirror to estimate spot size such that the correct adaptive gain term is applied for the rotated image. The modeled adaptive tracker model was simulated over scenarios that showed the tracker's effectiveness in adapting to a range of non-optimal QUAD-cell responses. Consider the following sections for a review of notable research conclusions and contributions.



## 5.1 Notable Conclusions and Contributions of Research

### 5.1.1 Defining QUAD-cell Behavior

This research makes an important claim that the QUAD-cell is inherently unreliable for resolvable LEO objects that have asymmetrical characteristics, where this claim is supported by the following expressions that were developed in Sections 2.4.3 and 2.4.4,

$$|\widehat{I}_j| = K_{gj}|\Delta a| \quad (5.1)$$

$$K_{gj} \sim \frac{1}{w_j(z)} \quad (5.2)$$

Recall these equations are fundamental in describing how the QUAD-cell measures tilt distortion. Any perceived asymmetry for the LEO object's intensity makes equation (5.1) incapable of mapping  $|\Delta a|$ , one-to-one, to an intensity shift, as required. Equation (5.2) particularly shows the repercussion of using a QUAD-cell to measure tilt distortion. Since the QUAD-cell poorly samples spot sizes, it can only estimate spot displacement via intensity shifts. However, the measured intensity shifts are inversely proportional to spot sizes as expressed by the generalized centroid term,  $K_{gj}$ , of equation (5.2). For an arbitrary LEO object,  $K_{gj}$  is an uncharacterized random variable that may assume non-linear behavior, making a proportional mapping between  $|\Delta a|$  and  $|\widehat{I}_j|$  impossible. Therefore, the QUAD-cell's behavior is "well-behaved" only if equation (5.1) expresses a linear relation such that the measured tilt,

$$\widehat{W}_j = \frac{\widehat{I}_j}{K_{gj}f} \quad (5.3)$$

uniquely maps and is proportional to the QUAD-cell's normalized intensity shift,  $\widehat{I}_j$ .

### 5.1.2 Creating Symmetrical Intensity Distribution/Spot Shape

As discussed, a resolvable LEO object having asymmetrical characteristics causes the QUAD-cell to deviate substantially from optimal behavior. Accordingly, this research makes a critical simplification by rotating the imaged LEO object over the PTS's QUAD-cell. Without the image rotation methodology, the author believes it would be unfeasible for a tracker system to accurately account for all the unpredictable characteristics of an LEO object. The rotation transforms an asymmetrical intensity distribution into a symmetrical one, a necessary requirement for the QUAD-cell. Another critical advantage of image rotation is that it may null any apparent object rotation; thereby, eliminating the pseudo tilt phase contribution. Recall that apparent object rotation due to an object's motion or a telescope's Coudé path induces a QUAD-cell intensity imbalance that registers as a false or pseudo tilt phase. The final advantage of image rotation lies with creating a symmetrical spot shape. Generally, an arbitrary LEO object has an asymmetrical shape that induces distinct centroid gains,  $K_{g_x}$  and  $K_{g_y}$ . Typically, this requires an adaptive tracker to estimate both  $x$  and  $y$  spot dimensions. However, the image rotation makes a symmetrical spot shape where  $K_{g_x}$  and  $K_{g_y}$  are made identical such that the subscripts of equations (5.1) thru (5.3) can be dropped. Now, the adaptive tracker only needs to estimate one dimension for the spot; this reduces measurement, processing, and calibration time by 50%.

### 5.1.3 Considering Methods to Estimate Spot Size

This research considered four methods to estimate image spot size and corresponding centroid gain for an arbitrary LEO object:

- **Utilize a focal plane array or low bandwidth wavefront sensor**
- **Monitor the deformable mirror's average shape via actuator voltages**
- **Measure slope discrepancy for Shack-Hartmann wavefront reconstructor**
- **Dither fast steering mirror to introduce a known tilt disturbance**

Since this research employed the dither method, it is summarized in detail here; refer to Section 2.8 for detailed descriptions of the other methods. All methods considered set a reference spot size (centroid gain) to determine when an arbitrary spot size deviates from optimal.

This research developed an intuitive method that identified the optimal spot size; the method utilized a calibrating laser source to measure open loop (OL) and close loop (CL) tilt phase processes. By varying the source's spot size, then making OL and CL tilt phase measurements for each spot size, this research identified the optimal spot size to be the size that resulted in the least measurement error for both OL and CL tilt phase processes. Refer to figures 29 and 30 of Section 3.6.2.1 where the optimal spot corresponds to the simultaneous minimums for the OL and CL residual phase error curves.

The dithering method uses the reference centroid to detect non-optimal spot sizes by introducing an artificial but known tilt disturbance to the QUAD-cell. By commanding the fast steering mirror to move with a known throw and frequency, the reference centroid ( $K_{g,opt}$ ) generates a reference dither signal,

$$|\hat{I}| \cos(\omega t) \quad (5.4)$$

This reference signal is then used to assess the dither signal that results from an arbitrary LEO object,

$$|\tilde{I}| \cos(\omega t) \quad (5.5)$$

Only the amplitudes are measured and averaged over a dither cycle; therefore, by measuring the resultant  $|\tilde{I}|$ , then comparing to the known optimal  $|\hat{I}|$ , the unknown centroid gain can be estimated. The general idea is that a larger or smaller spot than optimal will reflect in the  $\tilde{I}$  values. This method provides a robust way to rapidly determine the adaptive gain term that was developed in Section 4.1.6,

$$K_c = \frac{1}{K_{g\_opt}} \left| \hat{I} / \tilde{I} \right| \quad (5.6)$$

Since  $K_{g\_opt}$  and  $|\hat{I}|$  are known system constants determined during a one-time system calibration, only  $|\tilde{I}|$  is measured to apply the correct  $K_c$ . The dither signals are filtered to improve the fidelity of the signals when disturbed by atmospheric tilt and noise sources.

#### 5.1.4 Defining the Tracker/QUAD-cell Control Problem

Recall from Section 2.6 that the role of the tilt tracker is to accurately measure the reference tilt disturbance,  $R(j\omega)$ , and provide a much attenuated output to the optical system,

$$E(j\omega) = H(j\omega)R(j\omega), \quad (5.7)$$

where the tracker is modeled by a filtering transfer function,  $H(j\omega)$ , in the  $s$ -domain. This research showed that deviations in spot size away from optimal causes the tracker to perform sub-optimally,

$$\begin{cases} H(j\omega) \approx 1 & \text{for } (W(z) \gg W_{opt}) \\ H(j\omega) \approx 1 - \frac{\Delta_{sat}(W(z), R(j\omega))}{R(j\omega)} & \text{for } (W(z) \ll W_{opt}) \end{cases} \quad (5.8)$$

Equation (5.8) demonstrates two extremes for sub-optimal tracker performance where it can nearly unity pass reference tilt disturbances to the output for “large” spot sizes or provide a significant non-zero saturation error signal for “small” spot sizes.

This work further investigated the effects that the PTS’s operation had on the tracker’s gain and phase stability margins,

$$\begin{aligned} GM &\approx \frac{1}{\alpha} \left( \frac{2}{\omega_n \bar{\tau}} + 0.5 \right) \\ PM &= -\phi(\bar{\tau}, \alpha) - \phi(\alpha) + \frac{\pi}{2}, \end{aligned} \quad (5.9)$$

where these equations are derived in Section 3.5.2. The PTS’s operation, specifically sampling frame rate, detector read-out, and zero-order holds, was shown to induce control loop delay,  $\bar{\tau}$ , that erodes stability margins. Furthermore, any deviation of the PTS’s normalized measurement response,  $\alpha$ , above unity, was shown to exacerbate the reduction of stability margins in the presence of loop delay. The  $GM$  and  $PM$  expressions for equation (5.9) are very useful to determine the maximum allowable loop delay for desired stability margins. Also, the expressions allow a tilt tracker designer to determine the minimum threshold frame rate for the detector. Additionally, this research identified through simulation results that the non-adaptive tracker does become unstable when  $\alpha$  equals or exceeds the  $\alpha_{critical}$  value. The expressions for equation (5.9) are again useful to identify a particular  $\alpha_{critical}$  for a given system. The expressions have wide applicability beyond second order dynamic systems; higher order systems that can be approximated by second order dynamics can apply the  $GM$  and  $PM$  expressions directly. The derivation procedure

can be generalized to apply to other systems where a second order approximation is not valid.

### **5.1.5 Recommending Adaptive Tracker Capabilities**

The author presented two recommendations to enhance the adaptive tracker's robustness while tracking a LEO object. The first recommendation envisions the tracker having a capability to automatically recalibrate once a non-optimal spot size is detected. This is vital because an LEO object's characteristics can change unexpectedly after the initial calibration such that the initial calibration is made irrelevant to present conditions. The proposed recalibration methodology only recalibrates when the tracker error deviates beyond the diffraction angle zone,  $\bar{\theta} \pm \sigma_{\theta} > \lambda/D$ ; periodically calibrating the tracker may unnecessarily disrupt the tracking process. The second recommendation envisions averaging the PTS's output signals to reduce noise effects from band-limited white noise. Operating the PTS with the highest frame rate possible for adequate signal levels, may allow the sensor to take multiple samples of a given tilt instance. This research has demonstrated that averaging the samples had a measureable benefit in reducing the noise variance for the PTS's output.

## **5.2 Future Considerations**

Throughout this research from problem definition to modeling and simulation, the author has taken account of particular areas that warrant further investigation to confirm computer simulations, enhance research findings, or provide a path forward for others. Consider the following highlighted areas:

- Model With Real System Data:** The lack of real system data for the SOR AO system was a limitation in modeling and simulation for this research. An enhancement for the QUAD-cell characterization would employ image files of prototypical LEO objects imaged by the SOR's 3.5 meter telescope instead of artificial images of generic LEO objects that were used in this research. The real data image files would ensure the QUAD-cell characterization is as relevant as possible for the system under consideration. For instance, if the imaging smears the LEO object's asymmetrical characteristics, then the QUAD-cell will be less sensitive to the LEO object's asymmetry. Along with actual QUAD-cell specifications, particularly detector dimensions, the real image data files would have allowed the determination of a typical range of LEO object spot sizes and corresponding centroid gain variance.
- Verification by Physical Model:** A computer simulation that integrates the optical models with the *SIMULINK*<sup>®</sup> tilt tracker model was not feasible for this research. Ideally, the tracker model should respond to an optical model for the PTS where real-time tracker performance could be assessed by residual error in addition to optical (image) feedback as given by a CCD camera. However, the processing speed for a *MATLAB*<sup>®</sup> based integrated computer model would be prohibitive; therefore, a physical model is recommended. A physical model for the PTS optical leg would allow the author to confirm the feasibility of the calibration procedure carried out in this research that determined the reference centroid. Additionally, the author would measure known tilt disturbances with asymmetrical and/or rotating sources to confirm research findings. A physical model for the non-adaptive and adaptive trackers would involve inherent and realistic limitations such as noise disturbances, optical aberrations,

non-ideal fast steering mirror response, and control loop delays due to all system components. Of critical interest to investigate with the physical model, is the determination of the  $\alpha_{critical}$  value and if the adaptive tracker that employs the dither method is effective in maintaining optimal performance over a range of non-optimal sensor responses. Finally, the dither method must be investigated to determine any error in the centroid gain estimate that is induced by mirror dithering/oscillations.

- Image Rotator Development:** To confine the scope of this research, the author abstracted from the modeling of an image rotator; therefore, future work should involve developing an image rotator. Image rotation is an existing technology employed in astronomical imaging systems. Typically, the technology uses a Dove prism that inverts an image by  $180^\circ$  and if the prism is rotated about the optical axis, the image will rotate twice the rate of the prism rotation rate [24]. The author desires to investigate the feasibility of using a Dove prism to create a rotating image for the PTS. The prism would have to rotate at various rates to adjust with the QUAD-cell detector's variable frame rate. Recall the image rotation rate must be significantly faster than the frame rate to create an average intensity distribution that is symmetrical.
- Hybrid-Adaptive Tracker System:** The author's literature review revealed innovative methods to estimate centroid gain, where these methods are detailed in Section 2.8. Each method was developed in reference to the higher order aberrations AO loop and with primary applications toward natural and laser guide stars. The dither method employed in this research is effective in estimating the centroid gain, but the artificial tilt signal is a likely source of estimation error. Additionally, dithering the fast steering mirror complicates the control loop. Therefore, the other passive methods



that do not employ active control should be investigated to determine their applicability towards tracking an arbitrary LEO object. Since the lower and higher order AO loops “see” the same LEO object, the author envisions a hybrid-adaptive tracker where the different loops can “communicate” with one another to provide a centroid gain estimate. The passive estimation methods utilizing a Shack-Hartmann wavefront sensor could be applied during high signal levels, while the dither method utilizing a QUAD-cell detector would only engage for low signal levels. This would ensure that the fidelity of the centroid estimate is as high as possible over the range of signal levels.

## Bibliography

- [1] U.S Air Force Fact Sheet: Starfire Optical Range at Kirtland AFB, New Mexico, Air Force Research Laboratory, Directed Energy Directorate, March 2009
- [2] R.Q. Fugate, "Observations of faint objects with laser beacon adaptive optics," SPIE Adaptive Optics in Astronomy/ Vol. 2201/1994
- [3] J. Brown, R. Johnson, and J. Spinhirne, "Measurement of Tilt and Focus for the Sodium Beacon Adaptive Optics on the Starfire 3.5m Telescope," Air Force Research Laboratory, Directed Energy Directorate, September 2010
- [4] NASA, "What is Orbit?," [http://www.nasa.gov/audience/forstudents/5-8/features/orbit\\_feature\\_5-8.html](http://www.nasa.gov/audience/forstudents/5-8/features/orbit_feature_5-8.html) (Accessed: November 10, 2013)
- [5] G.D. Wirth. "Astronomical Magnitude Systems," Dept. of Physics and Astronomy, University of Toronto, August 2012
- [6] N.D. Paris, "LQR/LQG Tilt and Tip Control for the Starfire Optical 3.5-meter Telescope's Adaptive Optics System", AFIT Thesis, March 2006
- [7] R. K. Tyson, Adaptive Optics Engineering Handbook, Marcel Dekker Inc, New York, NY, 2000.
- [8] "Imaging Through Atmospheric Turbulence: Sensing and Correcting Tilt," class notes For EENG 716, Department of Electrical and Computer Engineering, Air Force Institute of Technology, Spring 2013
- [9] Roggemann, Michael C. and Byron M. Welsh. Imaging Through Turbulence. Boca Raton, FL: CRC Press LLC, 1996.
- [10] S.G. O'Brien, D.H. Tofsted, and G.T. Vaucher, "An Atmospheric Turbulence Profile Model for use in Army Wargaming Application I," Army Research Laboratory, February 2006
- [11] J.D. Schmidt, Numerical Simulation of Optical Wave Propagation *With Examples in MATLAB*, Washington SPIE, 2010
- [12] D.P. Looze, "Realization of system with CCD-based measurement," ScienceDirect Automatica/Vol. 41/September 2005
- [13] CVI Melles Griot, Gaussian Beam Optics, Technical Guide/Vol 2, Issue 1, 2009
- [14] G.A. Tyler, "Bandwidth considerations for tracking through turbulence," J. Opt. Soc. Am. A/Vol. 11, No. 1/January 1994

- [15] R. Clare and M. van Dam, “Wavefront Sensing for Adaptive Optics ” slide show, W.M. Keck Observatory, August 2007
- [16] G.A. Tyler, “Image-position error associated with a quadrant detector,” J. Opt. Soc. Am. A/Vol. 72, No. 6/June 1982
- [17] M. van Dam, “Measuring the centroid gain of a Shack-Hartmann quad-cell wavefront sensor by using slope discrepancy,” J. Opt. Soc. Am. A/Vol. 22, No. 8/August 2005
- [18] G. Herriot and J. Veran, “Centroid gain compensation in Shack-Hartmann adaptive optics systems with natural or laser guide star,” J. Opt. Soc. Am. A/Vol. 17, No. 8/August 2000
- [19] Adaptive Optics Tutorial at CTIO: 3. Wave-Front Sensors,  
<http://www.ctio.noao.edu/~atokovin/tutorial/part3/wfs.html>  
 (Accessed: January 26, 2014)
- [20] R. Johnson and D. Montera, “A New Sodium Guidestar Adaptive Optics System for the Starfire Optical Range 3.5 m Telescope,” Air Force Research Laboratory, Directed Energy Directorate, 2009
- [21] K. Ogata, Discrete-Time Control Systems 2nd ed. Upper Saddle River, NJ: Prentice Hall, 1995
- [22] R. McGuigan, “Effect of Coudé Path Rotation On Sodium Laser Beacon Perspective Elongation,” AFIT Thesis, March 2011
- [23] CH 7: Confidence Intervals and Sample Size,  
<http://highered.mcgraw-hill.com/sites/dl/free/0072549076/79745/ch07.pdf>  
 (Accessed: January 26, 2014)
- [24] D.W. Swift, “Image rotation devices-a comparative survey,” Optics and Laser Technology, August 1972

REPORT DOCUMENTATION PAGE				Form Approved OMB No. 074-0188	
<p>The public reporting burden for this collection of information is estimated to average 1 hour per response, including the time for reviewing instructions, searching existing data sources, gathering and maintaining the data needed, and completing and reviewing the collection of information. Send comments regarding this burden estimate or any other aspect of the collection of information, including suggestions for reducing this burden to Department of Defense, Washington Headquarters Services, Directorate for Information Operations and Reports (0704-0188), 1215 Jefferson Davis Highway, Suite 1204, Arlington, VA 22202-4302. Respondents should be aware that notwithstanding any other provision of law, no person shall be subject to a penalty for failing to comply with a collection of information if it does not display a currently valid OMB control number.</p> <p><b>PLEASE DO NOT RETURN YOUR FORM TO THE ABOVE ADDRESS.</b></p>					
1. REPORT DATE (DD-MM-YYYY) 17-03-2014		2. REPORT TYPE Master's Thesis		3. DATES COVERED (From – To) Sep 2012 – Mar 2014	
TITLE AND SUBTITLE  Development of Adaptive Tilt Tracker that Utilizes QUAD-cell Detector to Track Extended Objects				5a. CONTRACT NUMBER	
				5b. GRANT NUMBER	
				5c. PROGRAM ELEMENT NUMBER	
6. AUTHOR(S)  Thornton, Issac J., First Lieutenant, USAF				5d. PROJECT NUMBER	
				5e. TASK NUMBER	
				5f. WORK UNIT NUMBER	
7. PERFORMING ORGANIZATION NAMES(S) AND ADDRESS(S) Air Force Institute of Technology Graduate School of Engineering and Management (AFIT/EN) 2950 Hobson Way, Building 640 WPAFB OH 45433-8865				8. PERFORMING ORGANIZATION REPORT NUMBER  AFIT-ENG-14-M-78	
9. SPONSORING/MONITORING AGENCY NAME(S) AND ADDRESS(ES)  Intentionally left blank				10. SPONSOR/MONITOR'S ACRONYM(S)	
				11. SPONSOR/MONITOR'S REPORT NUMBER(S)	
12. DISTRIBUTION/AVAILABILITY STATEMENT DISTRIBUTION STATEMENT A. APPROVED FOR PUBLIC RELEASE; DISTRIBUTION UNLIMITED.					
13. SUPPLEMENTARY NOTES This material is declared a work of the U.S. Government and is not subject to copyright protection in the United States.					
14. ABSTRACT  Atmospheric turbulence causes tilt distortion that requires telescopes to track and remove image jitter effects. This research develops an adaptive tilt tracking system to measure and compensate for centroid gain volatility while tracking extended objects. The adaptive tracker counteracts deviations in tilt measurement and correction, due to unintended centroid gain changes. Non-adaptive trackers experience sub-optimal bandwidths and possible instabilities. The adaptive tracker utilizes a quadrant (QUAD) cell tilt detector to measure tilt distortion and its centroid gain relates measured intensity imbalances amongst the four cells to tilt distortion. Additionally, this gain becomes a random variable as it is determined by random image spot characteristics. The tracked LEO object and atmospheric seeing govern spot characteristics. This research develops an innovative methodology that rotates the LEO object's image to create a more favorable intensity distribution for the QUAD-cell. Along with image rotation, an adaptive gain term yields significant improvements in QUAD-cell measurement performance, up to 91% for the simulated tilt processes. Using the image rotation and adaptive gain methodology, this research realizes an adaptive tilt tracker model that dithers the fast steering mirror to detect non-optimal centroid gains. Results show the adaptive tracker effectively counteracts centroid-gain deviations.					
15. SUBJECT TERMS Adaptive tilt tracker; tilt distortion; quadrant-cell detector; centroid gain; pyramid track sensor					
16. SECURITY CLASSIFICATION OF:			17. LIMITATION OF ABSTRACT  UU	18. NUMBER OF PAGES  156	19a. NAME OF RESPONSIBLE PERSON Louthain, James A., Lt Col, Ph.D, USAF
a. REPORT  U	b. ABSTRACT  U	c. THIS PAGE  U			19b. TELEPHONE NUMBER (Include area code) (937) 255-3636, ext 4620 james.louthain@afit.edu

Standard Form 298 (Rev. 8-98)  
Prescribed by ANSI Std. Z39-18